Modeling and Parameter Measurement of Special Electric Machines

Rajendra Thike

A Thesis
in
the Department
of
Electrical and Computer Engineering

Presented in Partial Fulfillment of the Requirements
for the Degree of
Doctor of Philosophy (Electrical and Computer Engineering) at
Concordia University
Montréal, Québec, Canada

September 2020

CONCORDIA UNIVERSITY

SCHOOL OF GRADUATE STUDIES

This is to certify that the thesis prepared

By: Rajendra Thike

Entitled: Modeling and Parameter Measurement of Special Electric Machines

and submitted in partial fulfillment of the requirements for the degree of

Doctor Of Philosophy (Electrical & Computer Engineering)

complies with the regulations of the University and meets the accepted standards with respect to originality and quality.

Signed by the final examining committee:

______________________________ Chair
Dr. Muthu Packirisamy

______________________________ External Examiner
Dr. Kiruba Haran

______________________________ External to Program
Dr. Liangzhu (Leon) Wang

______________________________ Examiner
Dr. Shahin Hashtrudi Zad

______________________________ Examiner
Dr. Luiz A.C. Lopes

______________________________ Thesis Co-Supervisor
Dr. Pragasen Pillay

Approved by ______________________________
Dr. Wei-Ping Zhu, Graduate Program Director

October 28, 2020

____
Dr. Mourad Debbabi, Dean
Gina Cody School of Engineering and Computer Science

Abstract

Modeling and Parameter Measurement of Special Electric Machines

Rajendra Thike, Ph.D.
Concordia University, 2020

Recent engineering applications such as electric and hybrid electric vehicles require higher performance electric machines. Accordingly, there have been a significant increase on research on performance improvement of electric machines for transportation applications. Opposed to the conventional machines, new and innovative traction machines have higher power density, higher efficiency, faster dynamic response, wider speed range and higher reliability. The modern simulation and manufacturing tools made it possible to obtain the desired performance requirements in the new and special designs at reasonable cost. Due to the special designs to improve a certain output variable subjected to several constraints, it is required to have advanced machine models for control and operation of these machines. Moreover, parameter measurement of these special electric machines are gaining a significant interest due to new and advanced motor drive testing systems such as power hardware in the loop emulation which use a look-up table based machine model for fast and accurate solution of machine dynamics.

This PhD work develops a novel automated current control method to measure the parameters of special electric machines. In contrast to the existing parameter measurement method that applies a voltage pulse excitation to the test motor for flux linkage measurement, the current control method developed in this thesis uses a current pulse with closed loop control. While the voltage pulse method requires a higher sampling frequency for machines with lower time constants, the number of samples available during the transient for a fixed sampling rate can be modified by using a current pulse to measure the flux linkages. In addition, the use of a current pulse in closed loop makes it possible to measure the machine flux linkages at operating points unattainable with the voltage pulse method due to inverter dead time and device drops. This PhD work also develops a current controller design methodology for the developed parameter measurement method, which aids in the automation of the measurement process in a real time system.

This PhD research also develops an experimental method to obtain the static torque angle curves and torque-ripple of synchronous reluctance machines (SynRM). The developed technique is used to study the performance of a SynRM using cold rolled grain oriented (CRGO) laminations against a regular SynRM using cold rolled non-grain oriented laminations. The SynRM using CRGO laminations are designed to have a higher saliency, and thus a higher torque per ampere and higher power factor. This thesis presents a comparative study of the torque performance of the CRGO and CRNGO SynRMs.

This PhD work also develops the mathematical model of an interior permanent magnet synchronous machine (IPMSM) with aligned magnet and reluctance torques. It is a new class of IPMSM also called shifted IPMSM, which is designed to have higher torque for lower magnet volume. The torque characteristics of the shifted IPMSM is different from conventional IPMSMs. For the analysis and operation of this new class of machine, a suitable mathematical model is lacking in the literature. The PhD work develops the mathematical model of the novel shifted IPMSM, and validates it using the experimentally obtained inductance, torque angle and torque-speed curves.

This thesis also develops a mathematical model of a novel hybrid variable flux machine (VFM) having rare-earth magnets in series with AlNiCo magnets for power hardware in the loop emulation applications. In order to emulate the VFM, emulation of the change in magnetization state is crucial. This thesis models the magnetization and demagnetization characteristics of the VFM as look-up tables. The current control method to measure the machine parameter proposed in this thesis is used to measure the flux linkage characteristics of the VFM, and a complete VFM model suitable for power hardware in the loop emulation is developed. The developed model is validated experimentally through the comparison of transient and steady state machine behavior.

The works presented in chapters 2 and 3 are primarily useful in generating the flux-linkages, inductances and torque look-up tables for behavioral model special electric machine models. Such a model is used in advanced model based controls that would not be possible with basic two axis machine models. Moreover, the developed techniques are useful in validation of finite element analysis simulation of special electric machines. Within the thesis, Chapters 4 and 5 used the techniques developed in chapters 2 and 3 to develop and validate the machine models of shifted interior permanent magnet synchronous machine and hybrid variable flux machine. The developed models are useful in drive operations of these motors using advanced control algorithms.

Acknowledgments

I am grateful to the mother nature for this life, every breath I take, and everything that I needed to survive. I am thankful to all the health professionals, researchers working on and who worked for the betterment of human health. Thanks to the ‘Time’, which made me realize that this life is mine but indebted to every human being who worked for the improvement in the quality of human life.

I would like to express my sincere gratitude from deepest inside my heart to my supervisor, Prof. Pragasen Pillay, NSERC/Hydro-Québec Senior Industrial Research Chair at Concordia University for his guidance, care and guardianship during the masters and doctorate degree. I am also thankful for his preaching which is useful to live a healthy and stress free life.

I would like to acknowledge the Department of Electrical and Computer Engineering at Concordia University for an excellent academic environment. The facilities and services at the university helped to work safely. I would also like to express my sincere gratitude towards my PhD committee members. Their insightful comments and questions during the course of PhD significantly helped to shape my thesis.

Special thanks goes to Dr. Chirag Desai for the professional and personal help and supports during the PhD work. I would like to thank Dr. Amitkumar Kortagere Sashidhar and Dr. Mathews Boby for the insightful discussions and suggestions to solve the problems faced in the experimental works. I would like to appreciate the help I received from Dr. L Masisi, Dr. J. Wanjiku, Dr. A. M. Aljehaimi, Dr. R. Sudharshan Kaarthik, Dr. A. Takbash, Dr. S. Maroufian, Dr. M. Ghasemi Bijan, and Dr. M. Al-Badri during the PhD work. I would like to remember the teaching from Mr. Pierre Angers during the installation of the dynamometer setup. I would also like to thank my colleagues Gabriel, Arvind, Sumeet, Gayathri, Shiva, Venkata, Dwaipayan, Bigyan, Tamanwe, Yupeng, Nazanin, Mohan and other PEER group members for the memorable and enjoyable laboratory environment.

This research work is done as part of NSERC/Hydro-Québec Senior Industrial Research Chair entitled “*Design and Performance of Special Electrical Machines*” held by Professor Pragasen Pillay at Concordia University. It is also done as part of the InnovÉÉ/NSERC CRD project entitled “*Emulation and Design of Electric and Hybrid Electric Vehicle Motor Drive Systems*”. This research is also partly funded by the NSERC Discovery Grant entitled “*Novel Electric Machine Design*

Topologies For Electrified Transportation". I would like to acknowledge the support of the Natural Sciences & Engineering Research Council (NSERC) of Canada and Concordia University.

Most importantly, I would like to remember the love, encouragement and patience from my family. I would like to dedicate this work to my mother, father, brothers, sister, and my wife, Mira and son, Rayen. I would like to thank Rayen for being understandable and patient while working late nights and during the weekends.

Contents

List of Figures

List of Tables

Abbreviations

AC Alternating Current. 1, 2

CCM Current Control Method. xi, 34, 35, 42, 43

CRGO Cold Rolled Grain Oriented. xi, xii, 6, 13, 16, 45–48, 55–57, 59–63, 113

CRNGO Cold Rolled Non-Grain Oriented. xi, xii, 13, 45, 47, 48, 55–63, 113

CSM Constant Speed Method. xi, 12, 18, 42, 43

DC Direct Current. 1

DTM Dynamic Testing Method. 12, 13, 18

EV Electric Vehicle. 1–3, 6, 46, 97

FEA Finite Element Analysis. xiii, 90, 91, 94, 96, 114

FFT Fast Fourier Transform. xiii, 78–82, 93, 103, 114

HEV Hybrid Electric Vehicle. 1–3, 97

ICE Internal Combustion Engine. 1

IM Induction Machine. 1, 2, 4–6, 64

IPMSM Interior Permanent Magnet Synchronous Machine. xii, xiii, 4, 6–8, 13, 14, 16, 17, 19, 21, 44, 46, 64–66, 68–70, 73–75, 77, 78, 80, 83–85, 87, 90, 91, 94–97, 111, 113, 114, 116

LRT Locked Rotor Test. 51, 53–56, 58, 63, 112

MMF Magneto-Motive Force. 46

MTPA Maximum Torque Per Ampere. xii, 13, 16, 17, 45–47, 50, 51, 55–57, 59–61, 63, 112, 113

NSERC Natural Science and Engineering Research Council. 5

PDF Pseudo-Derivative Feedback. x, xiii, 19, 26, 27, 35, 81

PI Proportional-Integral. x, 19, 26, 27, 52, 85, 108

PM Permanent Magnet. 2–4, 6, 12, 14, 15, 65, 67

PMSM Permanent Magnet Synchronous Machine. xii, 2, 4–8, 17, 18, 45–47, 58, 64–67, 77, 97, 102, 103, 114

PWM Pulse Width Modulation. 52, 54, 81, 85

SynRM Synchronous Reluctance Machine. x–xii, xv, 4–6, 12, 13, 15–17, 19–21, 44–64, 111–114

VFM Variable Flux Machine. xiii–xv, 4, 8, 9, 13, 14, 16, 97–108, 110, 111, 115

VPM Voltage Pulse Method. xi, 34, 35

VSI Voltage Source Inverter. vii, 11, 18, 25, 53, 80, 81, 84, 85, 111

WFSM Wound Field Synchronous Machine. 4

Chapter 1

Introduction

One of the major sources of city air pollution is due to the emissions from vehicles using Internal Combustion Engines (ICEs). For instance, 41% of CO_2 emissions in a typical city is due to transportation [1]. Owing to the significant contribution in global warming by petroleum based transportation infrastructures, a renewed interest in alternative transportation technologies for industrial and commercial off-road vehicles is growing. Studies suggested that the use of alternative vehicles using clean and renewable energy provide environmental as well as economic benefits [2]. Compared to conventional ICE, Electric Vehicles (EVs) and Hybrid Electric Vehicles (HEVs) have lower emissions and higher well to wheel energy efficiency. Thus, electrification of transportation industry help to reduce the total CO_2 emissions.

1.1 Electric Machines for Traction Applications

Though the transportation electrification helps to reduce the vehicle emissions, there are challenges associated with the electrification of transportation. The early transportation vehicles were powered by batteries. In the early 20^{th} century, the newly invented gasoline motor vehicle competed and won against the battery powered electric vehicle. It is mainly due to a smaller range of distance the vehicle can travel on a full charge. The early electric cars used Direct Current (DC) machines. DC machines have a lower efficiency and requires higher maintenance compared to Alternating Current (AC) machines. AC machines were not popular due to control complexity. However, with the advent of modern power electronics, control and computation devices, and material technology, AC machines become dominant DC in traction applications.

The modern era of EVs began with the development and commercial mass production of EV1 by General Motors. It used an AC Induction Machine (IM) in its traction drive system. With the

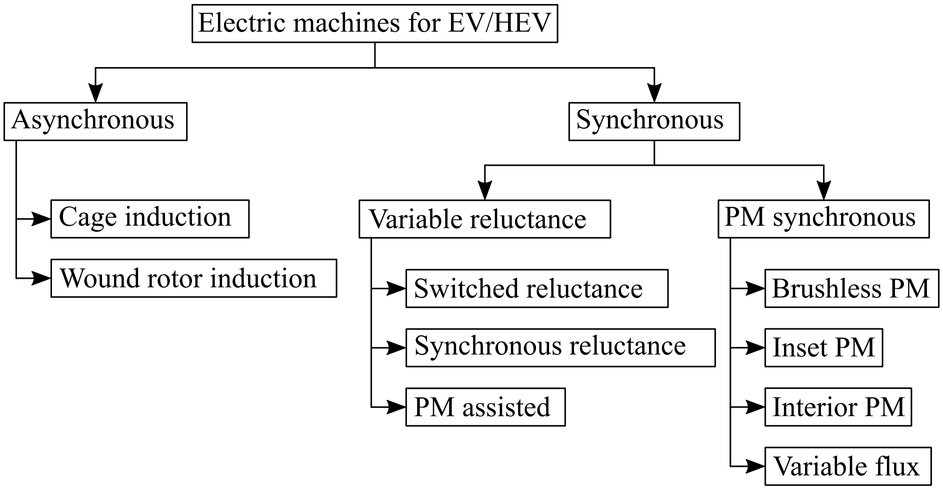

Fig. 1.1: Electric machine types used in electric and hybrid electric vehicles.

introduction of Toyota's highly successful Toyota Prius HEV, EVs and HEVs became popular which led to the development and launching of such vehicles by other auto manufacturers [3]. Recently, all the major auto manufacturers including Nissan, BMW, Hyundai, Ford and others are offering several ranges of EVs and HEVs. It is reported that the total number of EVs in the United States reached close to 1.4 millions by the end of third quarter of the year 2019, an 80% increment in two years [4].

Electric machines are the main component in the drivetrain of EVs. Modern EVs use various power semiconductor controlled AC motors. These motors have higher torque and power density, higher efficiency, higher starting torque, wider speed range, higher constant power speed range, faster dynamic response, higher reliability and better fault tolerance characteristics [5]. These features are the outcomes of the innovative designs and improvements of basic machine topologies, thereby giving rise to the emergence of new classes of machines. Fig. 1.1 shows the various designs of AC machines suitable for EV applications. It presents different types of potential AC machines applicable to traction drives.

Asynchronous machines are widely used in industrial plants and processes, and has a well established technology. Due to the high power density and high efficiency requirements, conventional IMs are not suitable for traction applications. With innovative designs, incorporating modern material and manufacturing technologies, automobile industries are able to obtain the required performance with IM in EVs. In the synchronous machine category, the EV manufactures are currently using Permanent Magnet (PM) based machines. Various design variations of PMSMs are in use on cars by automobile industries. An overview of electric machine trends in modern EVs with focus on current technologies and trends likely to follow in the future is presented in [6]. It predicts that the automobile industries are likely to continue the development of PM machines for

Table 1.1: Electric vehicles in the US and Canadian market with the type of traction motor.

Vehicle Model	Traction motor
Audi E-tron (2018)	IM
2020 Volkswagen E-Golf SE	PM
2019 Ioniq Electric	PM
2020 Mini Cooper SE	PM
Kia Soul	PM
Nissan Leaf S	PM
BMW I3	PM
Kia Niro Electric	PM
Chevrolet Bolt EV	PM
2020 Hyundai Kona Electric	PM
Porsche Taycan	PM
Tesla S60	IM
2012 Tesla Model S	IM
Tesla Model 3 2017	PM
Tesla Model Y	PM
Jaguar I-Pace	PM
Toyota Prius Prime (2020)	PM

EVs, while an intensive research on non rare-earth PM based machines will continue. Table 1.1 presents few of the EVs and HEVs in the US and Canadian market along with the type of electric machine the vehicles use. It also shows that there is an increasing tendency to use PM machines in modern EVs and HEVs.

1.2 Motivation

Due to the growing interest in electrification of the automotive vehicles, there have been significant increase on research on performance improvement of electric machines for transportation applications [7–9]. When compared to conventional designs, new and innovative designs of the traction machines have higher power density, higher efficiency, faster dynamic response, wide speed range and higher reliability. The new designs use modern simulation and manufacturing tools to obtain the desired performance requirements at reasonable cost.

The automobile industries are shifting towards the use of PM machines. It is mainly due to higher torque and power density of rare-earth magnets based PMSM. Due to the presence of magnets for air-gap field production in PMSMs, the rare-earth PMSMs have higher efficiency compared to conventional Wound Field Synchronous Machines (WFSMs) and IMs. Highly efficient machines not only improve the range of the vehicle, it also reduces the cooling system requirements. However, an issue with the rare earth based PMSMs is the higher PM cost and its fluctuation that hinders long term planning [10]. It is reported that the cost of magnets comprise approximately 20–30% of the motor cost [6]. Another issue with the rare-earth PMSMs is the requirement of field weakening current for high speed operation. The necessity of field weakening current at high speed not only reduces the high speed efficiency, but it also places a limit on the maximum possible speed of the machine. Due to these reasons, there has been an increased interest in the alternative electric machine that reduce the dependency on the rare-earth magnets and eliminate or reduce the field weakening current.

Various non rare-earth alternative traction machines are under development. The SynRM and VFM are two alternative electric machines that have gained significant interest recently. The SynRM rotor does not have windings and magnets. Due to its lower cost, simple and rugged structure, and high torque density, SynRM is one of the alternatives for traction drives. The VFM uses low coercive force magnets such that the magnetization states of the magnets can be varied during run-time. Such a feature in VFM is useful to eliminate or lower the flux weakening current at high speed. Apart from the machines that completely eliminates the use of rare-earth magnets, researchers are also working on non-conventional designs of PMSMs where the rare-earth magnets usage is lowered. All these non-conventional machines are termed as special electric machines.

The special electric machines for traction applications have high torque and power density. In order to obtain a performance comparable and higher to that of IMs, SynRMs and IPMSMs present a high rotor anisotropy. Their design is optimized for higher performance subjected to various constraints. In order to control these motors for high performance applications, it is required to have advanced models of these machines that considers the parametric variations caused by anisotropic rotor designs. Moreover, new and advanced motor drive testing systems without requiring a physical motor have become a topic of interest recently [11]. In such systems, the motor model is run numerically in a modern high speed and high capacity digital processor forming a real time emulation system. If a power converter is used to mimic the machine behavior for various operating conditions, the test system is called power hardware in the loop emulation system. Such an emulation system uses the machine model of the motor to solve for the system variables. Emulation of special electric machines requires its mathematical model, and the parameters defining the model. The machine model and its parameters are also essential for the operation of the motor drive. Thus, the modeling and parameter measurement of special electric machines are gaining significant interest. Industries as well as researchers are working on the development of machine models and parameter measurement techniques.

Industries are investing significant resources to improve the performance of electric machines. This research work is a part of Natural Science and Engineering Research Council (NSERC)/Hydro-Québec senior industrial research chair entitled “Design and Performance of Special Electric Machines”. This research work is also a part of InnovÉÉ-NSERC CRD project “Emulation and Design of Electric and Hybrid electric Vehicle Motor Drive Systems”. The research problem under study in this thesis is the modeling of the special electric machines, and development of machine model and parameter measurement techniques suitable for control development. This research work also focuses on techniques to identify the parameters of a machine including saturation effects and rotor position dependency, suitable for behavioral models of electric machines for power hardware in the loop emulation of the machines.

1.3 Review on Special Machines under Study

A brief review of the special electric machines under study in this thesis are presented below.

1.3.1 Synchronous Reluctance Machine (SynRM)

SynRMs are synchronous machines with no field excitation on the rotor. The SynRM rotor is laminated pieces of steel without any cage, magnets, and rotor winding. The concept of SynRM goes back to 1920s. However, due to the lack of suitable power converters, it gained interest among researchers in variable speed drives applications in 1990s [12]. Recently, SynRMs are becoming increasingly attractive in various applications including electric and hybrid electric vehicles (EVs and HEVs) [13]. It is mainly due to their low cost, high efficiency, high torque per ampere capability, simple and rugged structure and high operating temperature capability [14–16].

The performance of a SynRM in terms of torque and power factor depends on the ratio of direct axis inductance, L_d and quadrature axis inductance, L_q called the “saliency ratio” [17]. In order to produce torque in SynRMs, the rotor must have two symmetry axes whose magnetic properties be such that the d-axis (direct) has a very small reluctance and the q-axis (quadrature) has a larger reluctance compared to the d-axis. Since the SynRM rotors present high degree of anisotropy to obtain a performance comparable to that of IMs and PMSMs [18], saturation and cross-magnetization effects are prevalent. Due to saturation and anisotropic rotor design, the qd inductances in a high performance SynRM varies with rotor position, stator current magnitude and angle. For an accurate representation and control, and efficiency optimization of a SynRM, a model considering the saturation, cross-magnetization, and the rotor position effects is necessary [19–22]. As discussed in the previous section, the power hardware in the loop emulation and advanced control of electric machines requires the behavioral model of the machines considering parameter variations of the machines with current and rotor position. Thus, it is critical to obtain an accurate estimate of the SynRM parameters. A detailed literature review on the parameter measurement techniques will be presented in the next section.

Based on the improvements in the material and manufacturing technology, new SynRM topologies are evolving. A segmented pole SynRM using CRGO steel presented in [23] is a new type of SynRM with improved saliency ratio, and hence improved torque. The CRGO electrical steels are high quality anisotropic magnetic material with higher permeability in the rolling direction. The CRGO SynRM design presented in [23] is a four pole machine with each rotor laminations divided into four sections, with the rolling directions parallel to the rotor d-axis. This increases the d-axis inductance while reducing the q-axis inductance of the machine. A comprehensive manufacturing and assembly process of the CRGO SynRM is presented in [24]. An analytical model of the segmented-pole SynRM with CRGO laminations is presented in [25]. However, the research presented in [23,25] lacks the study of torque performance of the SynRM rotor with CRGO laminations in operating regions other than the rated operation. Since the SynRM is operated in wide torque and speed ranges in variable speed drives including EVs, the torque and torque performance of the SynRM in the entire operating range is of crucial importance. Thus, one of the objectives of this thesis is to study the torque performance of CRGO SynRM in the entire operating range.

1.3.2 Interior Permanent Magnet Machine with Aligned Magnet and Reluctance Torques

As discussed and presented in section 1.1, the present trend in modern electric vehicles is moving towards the use of PM machines. It is mainly due to higher efficiency and higher torque density of PMSMs compared to IMs. However, as discussed previously, the PM (rare-earth magnets) cost constitute 20-30% of the motor cost, and it has an increasing demand along with high price fluctuation. Consequently, the current trend in research focuses on the design of alternative electric machines technology that either do not use the rare-earth magnets, or reduce the amount required.

The IPMSM has two components of the useful torque. The reluctance torque which is due to the difference in the reluctance in the magnetic path in the direct axis and the quadrature axis, peaks at a different torque angle than the magnet torque. Due to this, the IPMSM is not able to utilize both the torque components fully at the same time. A new class of IPMSMs generally called the shifted IPMSM are seen as an alternative PM machine topology. Such a machine is of high interest due to it higher torque density, or the reduction in the magnet volume for the same amount of torque compared to the conventional IPMSM. The shifted IPMSM uses an asymmetrical rotor structure [26–38] such that the relative position of the reluctance and magnet axes are shifted from their regular position. The asymmetry is either created by using a hybrid rotor structure [27–31], or by shifting the magnetic axis and the use of flux barriers [32–37].

The asymmetrical rotor structures that use shifting of the magnetic axis and the reluctance axis by the use of flux barriers are simpler and easier to analyze. The objective of such designs is to align the magnet and reluctance torques to maximize the output torque. An asymmetry in the rotor design that allows the reluctance and magnetic torques to reach a maximum value at the same torque-angle is developed in [32, 33] for a V-type interior PMSM. The asymmetry is created in these designs by adoption of assisted barriers employed to allow the reluctance and magnetic torques to reach a maximum value near or at the same current phase angle. A similar approach for a surface-inset PMSM is adopted to improve the torque and efficiency in [34, 35]. In [39], a novel ferrite assisted synchronous reluctance machine is proposed that utilizes both reluctance and PM torque components fully. An interior PMSM design with an additional barrier to align the magnet torque and the reluctance torque is presented in [36]. It showed that the same output torque of a conventional IPMSM can be achieved by shifting one of the torque components with a lower permanent magnet volume. In [37], FEA analysis of an aligned axis IPMSM considering saturation is presented.

While researchers focused on the design improvements to improve the torque performance or reduce the magnet volume by utilizing the shifting technique, a theoretical analysis showing a mathematical model suitable for the analysis of such designs is lacking. In [40], a theoretical analysis of synchronous machines with displaced reluctance axis for different values of the shift angle between the reluctance and magnet axes is presented. The effects of positioning of permanent magnet axis relative to reluctance axis in PMSMs is presented in [41]. The authors developed the mathematical model of the surface inset PMSM by transformation of the machine equations in one reference frame to another reference frame with different orientation, and came up with three torque components viz; magnet torque, saliency (reluctance) torque and asymmetry torque. Finally, the authors concluded with the existence of an additional torque component in an asymmetric PMSM. In [30], a similar approach is used to describe the torque components in a hybrid rotor PMSM. The authors defined two more additional torque components viz; cross magnet torque and cross reluctance torque. However, these torque components vanish depending on the reference frame axis orientation. Thus, a comprehensive interpretation of the developed models are lacking in both [41] and [30].

A mathematical model of a machine allows a better understanding of the machine and it gives insight on the effect of each variable on the machine dynamics. Drive engineers use it for the design and operation of the drive. The torque characteristics of a shifted IPMSM is different to conventional IPMSM designs. The existing mathematical models used for the conventional IPMSMs must be modified to understand the shifted IPMSM behavior for its operation. One of the objectives of this thesis is the development of a mathematical model of the shifted IPMSM. Another objective of this thesis is the development of methods to obtain the parameters of the shifted IPMSM.

1.3.3 Variable Flux Machine (VFM)

VFMs are a new class of permanent magnet machines, for their ability to change the intensity of magnetization and memorize the flux density level in the magnets. The concept of VFM as memory motors is proposed in [42]. In VFMs, the magnetization of the magnets can be varied by a short duration current pulse. According to [42], memory motors have the combined advantages of a wound rotor machine (rotor flux can be varied) with those of wide speed PM machines that form a unique machine having the potential to find numerous applications in electric drives.

Since the magnet flux in PMSMs is fixed, the back-EMF of the machine increases proportionally with the speed. As the operating speed increases, the back-EMF increases, reducing the voltage available to drive the current. For extended speed operation beyond the base speed, due to the limited inverter voltage, the PMSM requires continuous field weakening current, which increases the machine losses. Thus, the PMSM efficiency drops for operating speeds above the base speed. Additionally, the flux weakening stator current limits the torque producing component of the stator current which in turns limit the torque speed range of the machine. Therefore, PMSMs are oversized to achieve a wide torque-speed range for traction applications, increasing the magnet usage [7]. These drawbacks can be diminished in the variable flux memory motors. The use of less expensive and readily available permanent magnets make the variable flux PM machine a good alternative to rare earth based PM machines. The feature to vary the PM flux not only reduces the power loss at higher speeds, but also increases the torque-speed range.

AlNiCo based VFMs

AlNiCo magnets have high remnant flux density comparable to rare earth magnets. However, their coercivity is very low which make them prone to demagnetization by stator excitation during operation. Hence, AlNiCo magnets were not used in PM machines. A new class of permanent magnet machine using AlNiCo magnets to utilize its low coercive property to gain an extra benefit out of PMSMs technology and to opt out some limits in existing rare earth magnets based PMSMs was proposed in [42, 43]. The first proposed variable flux memory motor uses a sandwich of tangentially magnetized AlNiCo magnets [42, 43]. The magnets are magnetized using a short duration current pulse from the same stator as that of a three-phase PMSM. However, the manufacturing of sandwich rotor design is complex and the rotor has lower mechanical strength compared to that of an interior PMSM. Moreover, the magnetization current requirement from the inverter is large, as a wider part of the magnets are near the rotor surface [44]. A variation in AlNiCo magnet based VFMs is proposed in [45–47] to obtain high torque density and reduced inverter rating. However, it is found that the magnetization level of machine is still affected by the armature reaction [48]. This is due to the trade off between the magnetization current reduction and magnetization level stability.

Hybrid excitations VFMs

Hybrid excitation based VFMs utilizes two sources of magnetic fields. A class of these motors utilizes both rare earth magnets as a constant source of flux and low coercivity magnets to vary the air-gap flux density [49–52]. The rare-earth and AlNiCo magnets can be in the form of a sandwich or 'Y' structure. The air gap flux is varied by controlling direct axis current (i_d) to change the magnetization of AlNiCo magnets in both positive and negative directions. However, the disadvantage with these designs is the requirement of a large current to vary the air gap flux due to the design of the rotor. Another class of hybrid excitation VFMs utilizes either stator field coils or rotor field coils to vary the air gap flux. The field controllable axial flux PM motor proposed in [53] uses circumferentially wound DC field windings placed in between the inner and outer stator rings. The concept of using auxiliary stator windings for radial flux controlling purposes has been investigated in [54]. PM machines described in [55, 56] has two rotor parts, one PM and one wound field, mounted on the same shaft separately. The design variation with either different magnetic circuits for PM and the wound field or the same magnetic paths has been explored.

In [57], a hybrid VFM consisting of the rotor with series AlNiCo and a small thickness rare earth magnet is presented. Due to the addition of the rare-earth magnet, the magnetization stability is improved. As discussed in the section 1.2, a highly accurate machine emulation system requires details on the machine's magnetic characteristics considering variation of machine geometric and magnetic data [58]. Thus, it is necessary to develop a behavioral model of the VFM for emulation applications. In order to develop a detailed look-up table based behavioral model of a VFM, a fast and accurate parameter measurement method is required. One of the objectives of this thesis is the development of a behavioral model of the series hybrid VFM and also the development of a suitable fast and accurate parameter measurement method applicable to the series hybrid VFM.

1.4 Review on Parameter Measurement Techniques

The parameters of a special electric machine are number of poles, stator resistance, stator inductance and magnet flux linkage. These parameters are essential to control the machine drive. A basic machine model may use constant parameters, while more sophisticated and high performance control requires a detailed machine model considering saturation and cross-magnetization effects. It was shown in [59] that the accurate dynamic modeling and control of a special electric machine considering machine's magnetic saturation is mandatory to have an accurate prediction for performance measures like output torque, power factor, and stability. In power hardware in the loop emulation of electric machines, in addition to saturation and cross-magnetization effects, it is required to have the rotor position effect on the parameters for accurate representation of the machine. Out of the machine parameters mentioned above, stator inductance is affected most by saturation. In general, a dq model is used for the special electric machines, in which the stator inductance is composed of d and q-axes inductances. Based on the needs in machine and drive designs, parameter measurement methods are evolving with the available new power and computation devices. A brief review of existing parameter measurement methods are given below.

1.4.1 DC and AC Standstill Tests

In standstill tests, an appropriate DC or AC excitation is applied to the machine. The DC locked rotor and AC locked rotor tests are widely established methods to measure the inductances with saturation effects due to currents in the self winding [60]. Fig. 1.2 shows the circuit connection to measure the inductances using DC and AC standstill tests. In the DC standstill test, the machine rotor is locked at either d-axis or q-axis. A DC source is used to supply a pulsed voltage. The transient current is measured and the motor inductance is calculated using the following equation.

$$L_d = \frac{\int_0^T (v_d - i_d R)\, dt}{I_d} \tag{1.1}$$

where, L_d is the d-axis inductance, v_d and i_d are the measured instantaneous d-axis voltage and current, R is the stator resistance, I_d is the steady state d-axis current, and T is the integration period by which the transient settled down.

In the AC standstill test, instead of a DC source, an AC source with sinusoidal voltage is used to excite the stator while the rotor is kept locked at the axis on which the inductance is to be measured. The reactive power at the fundamental frequency is measured using a power meter. The

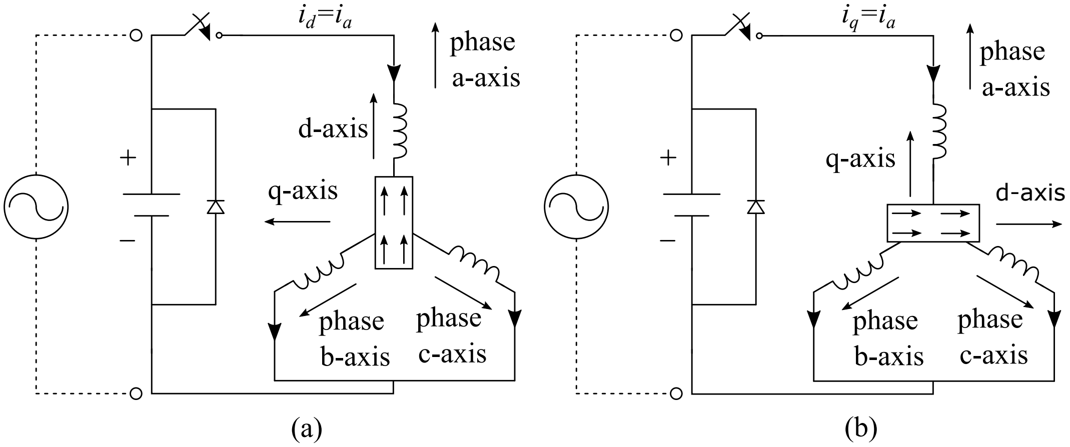

Fig. 1.2: DC and AC test Circuit diagram to measure (a) d-axis inductance. (b) q-axis inductance.

dq inductances are computed using the following equation.

$$L_d(or L_q) = \frac{Q_1}{2\pi f I_{rms1}^2} \tag{1.2}$$

where, Q_1 is the reactive power at the fundamental frequency, f is the frequency of the applied voltage, and I_{rms1} is the rms current at the fundamental frequency. Both DC and AC standstill tests are simple. However, they cannot be used to measure cross-magnetization effects and position dependent inductances. A variation of the DC standstill method to determine the variation of machine inductance with rotor position is discussed in [61]. The authors use a voltage pulse for excitation to measure the inductances considering magnetic saturation and inductance variation distortion. In [62, 63], two voltage sources are used to measure the cross-coupling inductances; one for controlling the current in one axis, and another for supplying the voltage pulse in another axis. While [63] uses the neutral connection to supply a phase current, and [62] uses two extra resistors, both methods are only applicable to measure inductance maps for three rotor positions (each phase axis).

1.4.2 Standstill Test using a VSI

In the standstill test using a VSI, a pulsed voltage in the dq axes can be applied at any rotor position. Authors in [64] and [65] propose usage of a VSI in order to determine the complete flux linkage and inductance map of a permanent magnet synchronous machine. In this method, the machine rotor is locked at a fixed position, and the VSI applies a voltage pulse in one axis while controlling the current in the other axis. The voltages and currents are measured, and (1.2) is applied to obtain the inductance. This method is useful to obtain the complete flux linkage and inductance map including the rotor position variation of a PM synchronous machine or SynRM. However, one drawback of this method is that the response time of the machine varies with current magnitude due to saturation, making this method not suitable for real time implementation.

1.4.3 Constant Speed Method (CSM)

In the CSM, the test motor is run at a constant speed using a dynamometer test bench. The dyno motor is run in a speed control mode and the test motor is run in current control mode. The test motor is supplied with a combination of dq currents both in motoring mode and generating mode. To change the mode of operation from motoring to generating, the motor is run in opposite direction for the same combination of i_d and i_q. The flux linkage characteristics is obtained from the following equations [66].

$$\psi_d(i_d, i_q) = \frac{v_{q+} - v_{q-}}{2\omega_r} \tag{1.3}$$

$$\psi_q(i_d, i_q) = -\frac{v_{d+} - v_{d-}}{2\omega_r} \tag{1.4}$$

where, $\psi_d(i_d, i_q)$ is the d-axis flux linkage, $\psi_q(i_d, i_q)$ is the q-axis flux linkage, v_{q+} is the q-axis voltage for positive speed, v_{q-} is the q-axis voltage for negative speed, v_{d+} is the d-axis voltage for positive speed, v_{d-} is the d-axis voltage for negative speed, and ω_r is the rotor electrical speed. The constant speed method (CSM) produces highly accurate results [66, 67]. However, the test setup requires a full dynamometer setup, and the test result is an average flux linkage around the rotor positions.

1.4.4 Dynamic Testing Method (DTM)

In the Dynamic Testing Method (DTM), the magnetic model of the machine is identified during acceleration [66]. The test motor is supplied by a variable frequency variable voltage source operated in current control mode. Initially, the motor is accelerated to a negative speed of predefined magnitude. Then, a combination of dq current for which the flux linkages are to be calculated is applied to the motor such that the motor accelerates and changed the direction. The currents are maintained constant until the speed reaches the predefined magnitude. The motor speed, currents and voltages are measured during this interval, and the flux linkages are calculated using (1.3) and (1.4) as in the CSM.

However, the DTM requires a power supply capable of sourcing and sinking the power. When the applied torque is large, an extra arrangement may also be needed to increase the moment of inertia so that the data acquisition period can be made larger. Most importantly, the DTM produces an average flux linkage characteristics, and it cannot be used to measure position dependent flux linkages.

1.5 Objectives

As discussed in the previous sections, various new high performance electric machine topologies are evolving for traction applications. Control and operation of these special machines require detailed machine models. In order to test the electric drive systems, power hardware-in-the-loop machine emulation is increasingly being recognized as an effective testing methodology. Such testing systems require detailed machine models considering saturation and cross-magnetization effects and rotor position dependency. Thus, the development of special electric machines models and efficient parameter measurement techniques for such applications is necessary. The objective of this PhD research work are as follows:

(1) Development of efficient parameter measurement techniques applicable to special electric machines with focus on automation in parameter measurements.
In this research work, a new parameter measurement technique will be developed. The developed technique can be implemented in a real-time system for automated parameter measurement requiring no post-processing of the measured data.

(2) Study on the torque performance of a CRGO SynRM.
In this research work, an experimental method will be developed for torque performance measurements of SynRM. Four different experimental methods for obtaining MTPA characteristics will be evaluated, and a comparative study of CRGO and CRNGO SynRMs will be carried out.

(3) Development of mathematical model of the novel shifted IPMSM with aligned magnet and reluctance torques.
In this research work, a mathematical model of the novel shifted IPMSM will be developed. A suitable parameter measurement technique will be developed to validate the developed mathematical model.

(4) Modeling and performance measurement of a novel series hybrid VFM.
In this research work, a VFM model considering the flux variability in the series hybrid VFM will be developed. Since the traditional experimental method to locate the rotor d-axis does

not apply to novel motor designs, this research work also develops an experimental method to locate the rotor d-axis of novel motor designs.

1.6 Contributions

The contributions of this PhD research work are summarized below.

- Development of a novel automated current control based parameter measurement technique for special electric machines.
- Development of a current controller design technique that ensures almost similar current response for wide variation in machine inductance.
- Development of an experimental method to measure torque ripple of a special electric machine condition for wide operating range.
- Development of a dynamomteter test bench with four quadrant operation capability to measure torque characteristics of special electric machines.
- Development of a mathematical model of a novel shifted IPMSM with aligned magnet and reluctance torques.
- Development of an experimental technique to locate the direct axis of special electric machine having PM in the rotor.
- Development of a mathematical model of a series hybrid VFM.

Journal Papers

- R. Thike and P. Pillay, “Mathematical Model of an Interior PMSM with Aligned Magnet and Reluctance Torques,” in IEEE Transactions on Transportation Electrification, doi: 10.1109/TTE.2020.2991369.
- R. Thike and P. Pillay, “Automated Current Control Method for Flux-Linkage Measurement of Synchronous Reluctance Machines,” in IEEE Transactions on Industry Applications, vol. 56, no. 2, pp. 1464-1474, March-April 2020, doi: 10.1109/TIA.2020.2967689.
- K. S. Amitkumar, R. Thike and P. Pillay, “Linear Amplifier-Based Power-Hardware-in-the-Loop Emulation of a Variable Flux Machine,” in IEEE Transactions on Industry Applications, vol. 55, no. 5, pp. 4624-4632, Sept.-Oct. 2019, doi: 10.1109/TIA.2019.2921286.

- R. Thike and P. Pillay, “Torque Performance of a Segmented-Pole Synchronous Reluctance Machine with Grain-Oriented Laminations,” under preparation for submission to IEEE Transactions on Transportation Electrification.

Conference Papers

- R. Thike and P. Pillay, ”Parameter Measurements and Modeling of a Novel Hybrid Variable Flux Machine with Series Rare-Earth and AlNiCo Magnets,” 2020 IEEE Energy Conversion Congress and Exposition (ECCE), Detroit, MI, USA, 2020, pp. 1433-1438, doi: 10.1109/ECCE44975.2020.9235628.
- R. Thike and P. Pillay, “Experimental Study of Torque-Ripple and its Effect on the Flux Weakening Range of Synchronous Reluctance Machines,” 2019 IEEE International Electric Machines & Drives Conference (IEMDC), San Diego, CA, USA, 2019, pp. 1479-1484, doi: 10.1109/IEMDC.2019.8785090.
- R. Thike and P. Pillay, “Experimental Investigation of MTPA Trajectory of Synchronous Reluctance Machine,” 2018 IEEE International Conference on Power Electronics, Drives and Energy Systems (PEDES), Chennai, India, 2018, pp. 1-6, doi: 10.1109/PEDES.2018.8707820.
- R. Thike and P. Pillay, “Automatic Inductance Measurements of Synchronous Reluctance Machines Including Cross-Saturation Using Real-Time Systems,” 2018 IEEE Energy Conversion Congress and Exposition (ECCE), Portland, OR, 2018, pp. 6121-6127, doi: 10.1109/ECCE.2018.8558407.
- K. S. Amitkumar, R. Thike and P. Pillay, “Power-Hardware-in-the-Loop Based Emulation of a Variable Flux Machine,” 2018 IEEE Energy Conversion Congress and Exposition (ECCE), Portland, OR, 2018, pp. 6454-6460, doi: 10.1109/ECCE.2018.8558315.

1.7 Organization of the Thesis

This thesis is organized into six chapters. Chapter 1 introduces the research background along with the motivations behind the work. It also presented the objectives of the thesis.

Chapter 2 presents a novel automated current control technique to measure the parameters of special electric machines. The proposed method is applied to an inset PM machine and SynRM, and validated with standard existing methods. The chapter also presents a current controller design technique that ensures almost similar current response for wide variation in machine inductance.

Chapter 3 presents the study on the torque performance of CRGO SynRM. In this chapter, four different methods to obtain the MTPA characteristics of the SynRM is evaluated experimentally. It also presents an experimental method to obtain the torque-ripple of a SynRM.

Chapter 4 presents the mathematical modeling of a novel shifted IPMSM. The mathematical model is developed using the concepts in magnetic circuit analysis. In order to validate the developed model, an experimental method is developed to obtain the parameters defining the model, and the model is validated by comparing the measured torque performance of a prototyped machine with the performance predicted by the model.

Chapter 5 presents the modeling of a novel hybrid VFM. Experimental techniques to measure the parameters in the model are presented. The developed model is validated by comparing the simulated and experimental results.

Chapter 6 presents the conclusions and future works.

Chapter 2

Automated Current Control Method for Flux-Linkage Measurement

The dynamic performance of modern special electric machines such as SynRM and IPMSM highly depend on its parameters. The SynRM performance in terms of torque and power factor depends on the ratio of direct axis inductance, L_d and quadrature axis inductance, L_q called the "saliency ratio" [17]. In order to control and operate the motor, the inductance and resistance parameters are required. In advanced control algorithms such as MTPA, the flux linkage characteristics are very useful [68]. The control performance of a SynRM drive is improved by using accurate estimates of flux linkages and inductances [69]. Various studies showed that the accurate representation and control, and efficiency optimization of the SynRM, a model considering the saturation, the cross-magnetization, and the rotor position effects is necessary [19–22].

2.1 Introduction

There exists several methods to measure the flux linkages/inductances of SynRMs and IPMSMs [60–64, 66, 67, 70, 71]. With the advent of modern data acquisition and digital signal processing devices, new techniques are evolving to meet the needs of machine and drive design. While the constant dq inductances are enough for the control of conventional surface PMSMs, more advanced controls of advanced special electric machines requires machine parameters considering saturation and cross-magnetization effects. For applications such as the power hardware in the loop emulation of electric machines, a parameter based numerical machine model considering parameter variation with rotor position is used [72]. In order to use the experimental data to represent the machine model for such applications, an accurate and quicker measurement method is required.

Based on the existing literature, flux linkage identification methods are broadly classified into: (a) rotational tests, and (b) standstill tests. Rotational test methods can be further classified into constant speed method and dynamic testing method. While the CSM produces highly accurate results [66, 67], the test setup requires a full dynamometer setup, and the test result is an average flux linkage around the rotor positions. In the DTM presented in [66], the magnetic model of the machine is identified during acceleration. However, the data acquisition period become small at higher acceleration torque, and extra arrangement may be needed to increase the moment of inertia. Both the CSM and DTM cannot be used to measure position dependent flux linkages, thus making it unsuitable for applications requiring position dependent flux linkage variation.

In standstill tests, an appropriate DC or AC excitation is applied to the machine at standstill. The DC locked rotor and AC locked rotor tests are widely established methods to measure the inductances with saturation effects due to currents in the self winding [60]. However, they cannot be used to measure cross-magnetization effects and position dependent inductances. A variation of DC standstill method to determine the variation of machine inductance with rotor position is discussed in [61]. The authors use a voltage pulse for excitation to measure the inductances considering magnetic saturation and inductance variation distortion. In [62, 63], two voltage sources are used to measure the cross-coupling inductances; one for controlling the current in one axis, and another for supplying the voltage pulse in another axis. While [63] uses the neutral connection to supply a phase current, and [62] uses two extra resistors, both methods are only applicable to measure inductance maps for three rotor positions (each phase axis).

Authors in [64] and [65] propose using a VSI to determine the complete flux linkage and inductance map of a PMSM. It is a variant of the locked rotor test where the excitation may be AC or DC. In methods presented in [64] and [65], the machine rotor is locked at a fixed position, and the VSI applies a voltage pulse in one axis while controlling the current in the other axis without need for dynamometer setup or acceleration test. The flux linkage calculation methods employed in [62–65, 70, 71] applies a pulsed voltage to the machine in open loop. These methods require post processing of a huge data set (several Gigabytes). In [73, 74], real-time processing of measured data with some approximating functions are presented for standstill self identification of flux characteristics of SynRMs. The authors used a high test voltage as a trade-off between several contrasting factors and the sampling time of the system was 100μs. However, no analysis were presented on the accuracy of the measurement due to the limited sampling time. Moreover, the presented methods are useful to find the flux linkage characteristics at one rotor position.

Hwang et al. in [75] presented a current control based parameter identification of synchronous reluctance motor at standstill. The authors proposed to apply a current pulse in closed loop to obtain the machine resistance and inductance in two steps. In the first step, the integral gain in the

PI controller is set to zero, and the machine resistance is obtained from the reference current, the measured steady state current and proportional gain. In the next step, the integral gain is computed using the measured resistance, and the proportional gain is tuned until a critically damped response is obtained. The machine inductance is then obtained as the ratio of proportional gain and closed loop bandwidth. Such a method requires tuning the controller parameters for each operating point, and it cannot be programmed in a real-time system to automate the machine parameter measurement.

In real-time emulation and advanced control techniques, it is desirable to have evenly spaced data on the flux linkage and inductance variation with the rotor position [58, 76–78]. Based on the above discussion, the existing parameter measurement methods are not suitable for parameter measurement of special electric machines for such applications. This thesis proposes a novel current control based standstill method to measure the flux linkage and inductance of special electric machines such as SynRM and IPMSM under locked rotor conditions. In comparison to [75], the method presented in this thesis tune the current controllers only once, yet ensure a similar current response for all operating points, irrespective of the variation in the machine inductance. Such a response is obtained by using a pseudo-derivative feedback (PDF) controller with a novel design technique compared to a PI controller in [75]. The flux linkage is obtained by integrating the measured response. The benefit is that the proposed method can be programmed in a real-time system to automate the measurement process. Compared to the existing literature, the followings are the contribution of this thesis to the parameter measurement of special electric machines.

- The proposed method applies a pulsed current reference in closed loop in one axis (d-axis) while controlling the current in another axis (q-axis) to a fixed value, which is not reported in the literature.
- This thesis also demonstrates in detail a method to automatically tune the current controllers required in the measurement process.
- This thesis also presents in details the implementation of the proposed method to compute the flux linkage and inductance in a real-time system without requiring data acquisition and post processing.

2.2 Mathematical Model of a SynRM

In order to demonstrate the current control method for flux linkage measurement of a special electric machine, a SynRM is used as a test machine. The proposed method is equally applicable to IPMSMs. Fig. 2.1a shows the geometry of the machine under test. It is a transversely laminated

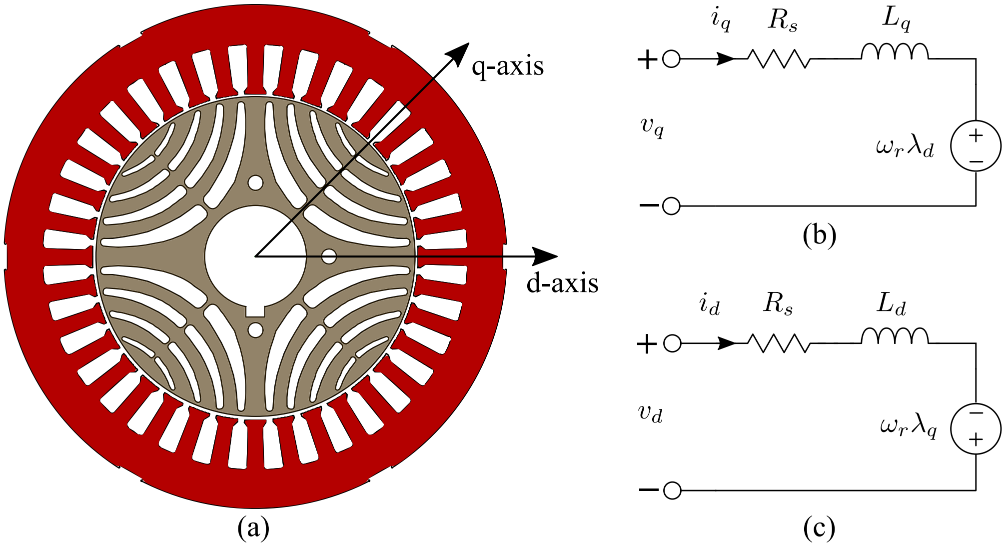

Fig. 2.1: SynRM under test and its equivalent circuits without core loss component. (a) rotor and stator geometry. (b) q-axis equivalent circuit. (c) d-axis equivalent circuit.

anisotropic rotor type SynRM. The nameplate data and some design details of the test machine are given in Table 2.1. Fig. 2.1b and 2.1c show the q- and d- axes equivalent circuits of the SynRM in dq model. Iron loss is not considered in this model. The equations describing the dynamics of the SynRM in the dq reference frame are given by (2.1) and (2.2).

$$v_q = R_s i_q + \frac{d\lambda_q}{dt} + \omega_e \lambda_d \tag{2.1}$$

$$v_d = R_s i_d + \frac{d\lambda_d}{dt} - \omega_e \lambda_q \tag{2.2}$$

where, v_d and v_q are d- and q-axes voltages respectively, λ_d and λ_q are d- and q-axes flux linkages respectively, i_d and i_q are d- and q-axes currents respectively, R_s is the per phase stator resistance, ω_e is the rotor electrical speed. Here, the flux linkages λ_d and λ_q are functions of i_d, i_q and rotor position, θ_e. In applications requiring the most accurate model, variations in the flux linkages with respect to the currents and the rotor position must be considered.

The last terms in (2.1) and (2.2) are speed voltage terms. When the rotor is locked at a fixed position, the speed voltage terms are zero and equations for the d- and q-axes voltages at locked rotor condition are given by (2.3) and (2.4). The flux linkages λ_d and λ_q in the d- and q-axes can be expressed as the functions of several inductances as shown in (2.5) and (2.6). Both λ_d and λ_q are functions of i_d and i_q, and they can be written in terms of self and cross-coupling inductances: L_{dd}, L_{dq}, L_{qd} and L_{qq}.

$$v_d = R_s i_d + \frac{d\lambda_d}{dt} \tag{2.3}$$

Table 2.1: Specification of the SynRM under test.

Machine type	3 phase Δ connected
Rated Power	7.5 hp
Rated Current	20 A
Rated Voltage	230 V
Base Speed	850 rpm
Peak Torque	60 Nm
Number of Poles	4
Number of Stator Slots	36
Winding type	Fully pitched distributed
Air-gap length	0.4 mm
Stack length	200 mm
Stator outer diameter	208 mm
Rotor outer diameter	134.2 mm

$$v_q = R_s i_q + \frac{d\lambda_q}{dt} \tag{2.4}$$

$$\lambda_d = L_{dd}(i_d, i_q, \theta_e) i_d + L_{dq}(i_d, i_q, \theta_e) i_q \tag{2.5}$$

$$\lambda_q = L_{qd}(i_d, i_q, \theta_e) i_d + L_{qq}(i_d, i_q, \theta_e) i_q \tag{2.6}$$

From the Table 2.1, it is seen that the machine under test is designed for delta connected winding. However, all six terminals of the motor are available to the user. In order to avoid mathematical operations that converts line currents to phase currents in delta connected machine, the windings are configured for wye connection during the test. Since the proposed test method is a standstill test with DC excitation, the applied voltage will still be within the rated winding voltage for wye connected motor.

2.3 Review on the Voltage Pulse Method

The voltage pulse based parameter measurement technique is presented in the literature for the parameter measurement of SynRMs and IPMSMs [62–65, 70, 71]. This technique can be used to measure the parameter variation with current magnitude and phase, and rotor position. A brief review on it and its limitations are discussed below.

For locked rotor conditions, the dynamic equations (2.3) and (2.4) can be written in integral form as (2.7) and (2.8).

$$\lambda_d = \int_0^t [v_d(\tau) - i_d(\tau)R_s]d\tau \tag{2.7}$$

$$\lambda_q = \int_0^t [v_q(\tau) - i_q(\tau)R_s]d\tau \tag{2.8}$$

In the voltage pulse based method to measure the flux linkage characteristics, a pulsed voltage is used as the excitation. The excitation voltage and the current response are measured. The measured voltages and currents are used in (2.7) and (2.8) to compute the flux linkages. The stator resistance, R_s is assumed to remain constant during the integration period; and it is found as a ratio of the average steady state voltage to the average steady state current during each pulse. In order to measure the d-axis flux linkage and inductances, a pulsed voltage is applied in the d-axis while controlling the q-axis current to a constant value. Similarly, in order to measure the q-axis flux linkage and inductance, a pulsed voltage is applied in q-axis controlling the d-axis current to a constant value. The duration of the pulsed voltage is governed by the time constant of the machine under test.

2.3.1 Limitations

As discussed earlier, to measure the q-axis flux linkage characteristics using the voltage pulse based method, a pulsed v_q is applied to the machine while controlling i_d to remain constant. During the period when the reference v_q is zero, due to the effects of inverter dead-time and device drops, the actual v_q appearing in the machine terminals is not zero when the inverter is controlled to apply a fixed i_d to the machine. Fig. 2.2 shows arbitrary gate signal waveform to an inverter leg and the output voltage waveform for both the positive and negative output currents. The output voltage V_o is a function of current direction and it can be written as a function shown in (2.9).

$$V_o = DV_d - Sign(I_o)(dV_d + \Delta_V) \tag{2.9}$$

where, D is the reference duty cycle, V_d is the DC link voltage, d is ratio of dead time to the switching period, and Δ_V is the device voltage drop. For an ideal inverter, the output voltage is DV_d, however, due to the device drops and the dead time, the output voltage of the inverter differs from the reference voltage. In order to study the effects of dead time and device drop, an iterative procedure is used to solve the value of v_q introduced when the reference consists of v_d only. Fig. 2.3 shows the variation in v_q with the rotor position, introduced due to dead time and device drops when

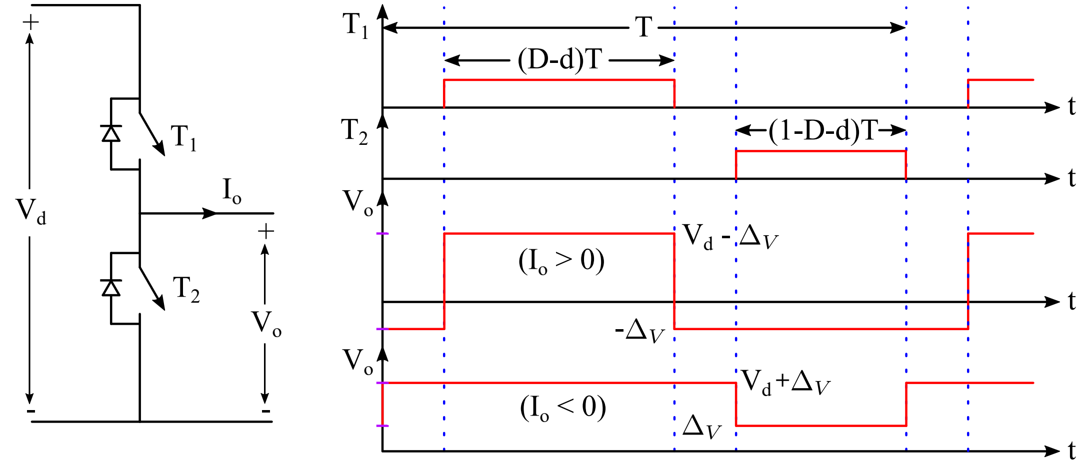

Fig. 2.2: Effect of dead time on the inverter output voltage showing output voltage waveforms for cases $I_o > 0$ and $I_o < 0$.

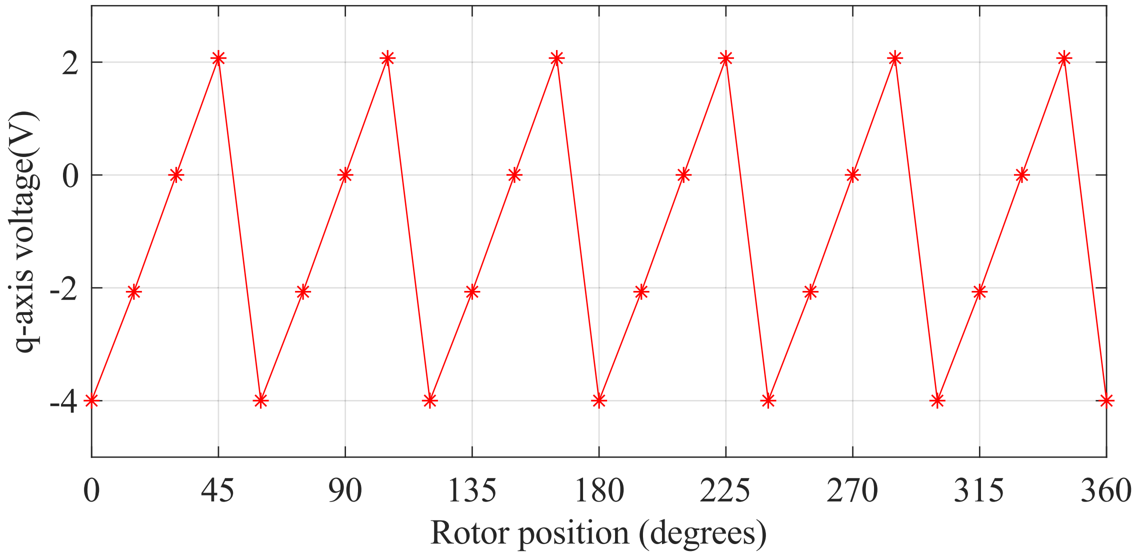

Fig. 2.3: q-axis voltage introduced due to an inverter dead-time of 5 μs and 1 volts of device drops when switching is 10 kHz, dc bus voltage is 100 volts.

the switching frequency is 10 kHz, inverter dead time is 5 μs, the device drop is 1 volts, and the dc link voltage is 100 volts. The presence of v_d causes i_d to flow in the machine. Thus, the voltage pulse based method is limited to measure the flux linkage characteristics for certain operating points in the $i_d i_q$ plane.

Since a pulsed voltage is used to excite the machine, the response of the machine depends on the electrical time constant. In order to study the effect of machine time constant on the computation accuracy in the measurement, three machines with time constants of $1ms$, $25ms$ and $100ms$ are simulated in MATLAB Simulink. Fig. 2.4 shows the step responses. The settling time for the current in the machine with a lower time constant is much smaller than the machine with a larger

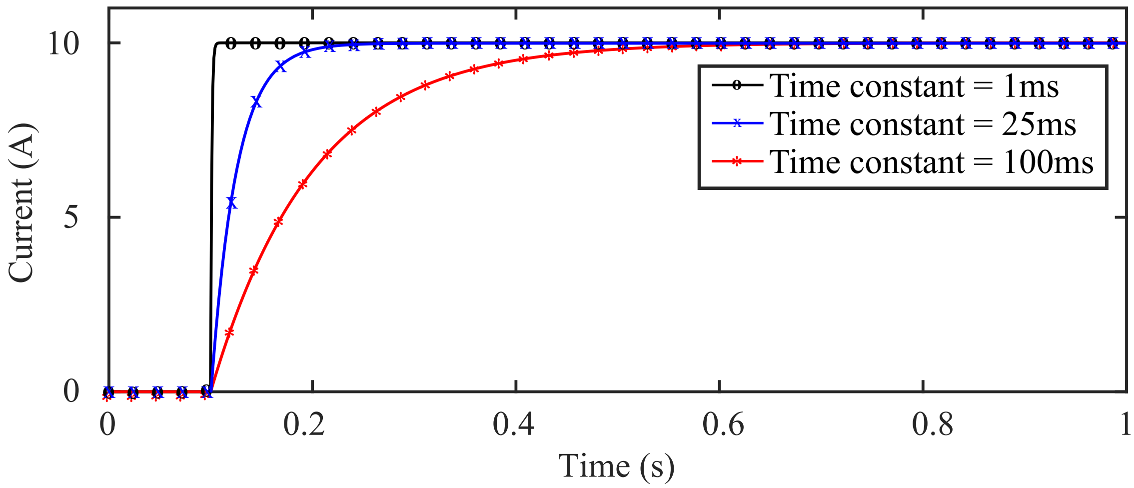

Fig. 2.4: Response of three systems having different time constants obtained in MATLAB Simulink.

time constant. The simulation time step was chosen to be $0.1\mu s$. Table 2.2 summarizes a comparison of errors in the calculated inductance when the responses are sampled at various sampling times. It shows that the percentage error in the calculated inductance increases with an increase in sampling time. For example, for a system with $1ms$ time constant, the percentage errors are 0.04%, 1.2% and 5% when sampled at $1\mu s$, $25\mu s$ and $100\mu s$ respectively. However, the percentage errors for machines with higher time constant are lower at all sampling periods. The higher percentage error in the low time constant machine is due to the lower number of samples available during the transient.

Thus, it is clear that the measurement sampling time should be low for higher accuracy. For the same level of accuracy, the sampling time should be smaller for machines with lower time constant. However, all the real-time processors have a maximum limit on its sampling time. Thus, when a voltage pulse based method is used in the measurement of flux linkage characteristics using a

Table 2.2: Percentage error in calculated inductances with various sampling times.

Sampling time		$1\ \mu s$	$25\ \mu s$	$100\ \mu$ s
L (mH)	Time constant (ms)	$\%$ error	$\%$ error	$\%$ error
1	1	0.04	1.2	5
10	10	0.004	0.12	0.5
100	100	0.0004	0.012	0.05
5	1	0.04	1.2	5
50	10	0.004	0.12	0.5
500	100	0.0004	0.012	0.05

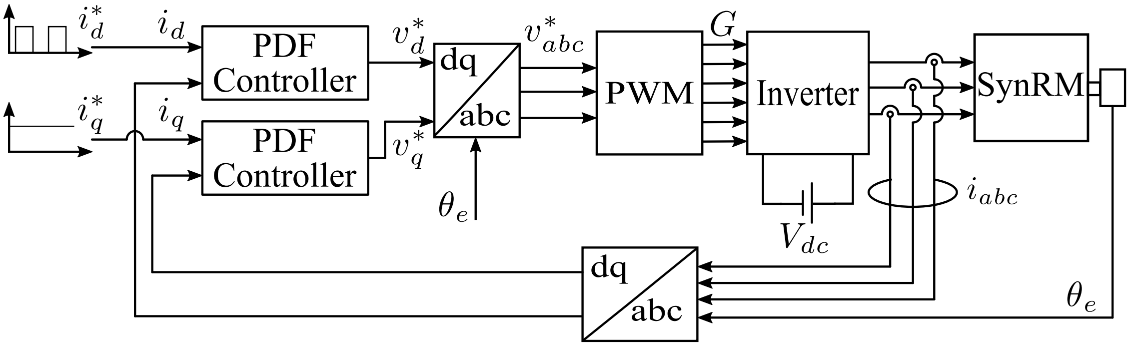

Fig. 2.5: Schematics of the proposed control strategy to measure the d-axis flux linkage and inductance (i_q^* would be pulsed and i_d^* would be constant for q-axis flux linkage and inductance measurement).

real-time system, there would be a significant computational error for lower time constant machines.

In addition, when the voltage pulse method is used to measure the inductance of a saturated machine, the settling time changes with the inductance. The settling time is large when the machine is unsaturated, and it decreases when the machine saturates. Due to the varying settling time, the voltage pulse method become unsuitable for automated parameter measurement where the integration period has to be fixed in advance.

2.4 Current Control Method

In order to overcome the above mentioned shortcomings, this thesis proposes a current control method to measure the flux linkage and inductance characteristics of special electric machines. In the proposed method, the test machine rotor is locked, and a pulsed current reference is applied in one axis while the current in the other orthogonal axis is controlled to a constant. Since both the currents are controlled, unlike the voltage pulse method, it is possible to measure the flux linkage characteristics at any arbitrary operating point in $i_d i_q$ plane. Additionally, due to the closed loop control, the accuracy in the measurement can be improved by modifying the response such that a sufficient number of data are available during the transient. This is important in the implementation using a real-time system with a limited sampling period.

Fig. 2.5 shows the schematic of the proposed technique to measure the d-axis inductances. In the proposed method, the rotor is locked at a fixed position, and a pulsed reference i_d is applied while i_q is controlled to a fixed value. The three phase currents are measured and transformed to the dq frame. The measured currents are subtracted from the references, and the errors are passed through the controller to generate the required voltage signals. A three phase VSI is used to apply the desired voltages in pulse width modulated form. In order to keep the fixed current intact due to

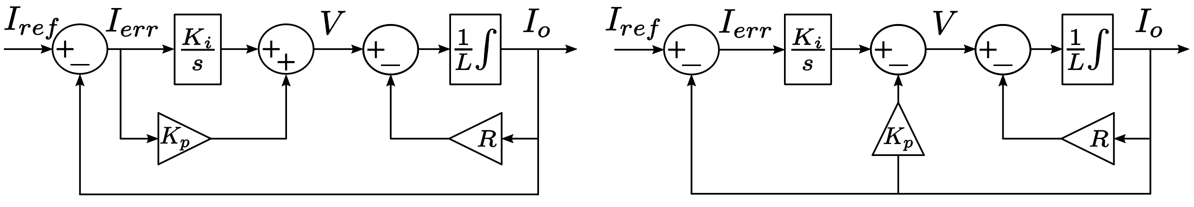

(a) (b)

Fig. 2.6: Two control structures to ensure zero steady state error. (a) PI controller. (b) PDF controller.

the pulsed current, the controller controlling the fixed current is made much faster compared to the controller controlling the pulsed current. Additionally, in order to meet the accuracy requirement, the controller parameters for the pulsed current controller are tuned to ensure an adequate number of samples during the transient period.

2.4.1 Current Controllers

The proposed method requires two current controllers. The major issue with the control problem is that the control design requires the parameters that are being measured. Thus, control design is a challenging task in the proposed method. Another requirement with the controllers is that the controlled parameters should have almost the same settling time irrespective of the variation in the plant parameters (saturation effects). Primarily, this ensures the same accuracy in the measurement at all operating points. In addition, the proposed method will be programmable in a real-time system with fixed current pulse period. Moreover, the controller should be simple with the least possible number of parameters, yet ensuring the applicability of an automatic tuning procedure.

Based on the mathematical model described by (2.3) and (2.4), the controlled systems are first order systems. In order to ensure zero steady state error, the controllers must have an integrator. Fig. 2.6a and Fig. 2.6b shows the two controllers, viz. PI and PDF controllers having only two controller parameters that assure zero steady state error for a first order system. The closed loop transfer function for them are given in (2.10) and (2.11) respectively. Standard form representations of these closed loop transfer functions are shown in (2.12) and (2.13); where, ω_c is the closed loop zero with the PI controller; ω_{nPI} and ζ_{PI} are the natural frequency and the damping ratio of the closed loop system with PI controller; ω_{nPDF} and ζ_{PDF} are the natural frequency and the damping ratio of the closed loop system with PDF controller. The expressions relating these standard form parameters to the controller and system parameters are given by (2.14) to (2.16).

$$\left.\frac{I_o(s)}{I_{ref}(s)}\right|_{PI} = \frac{\frac{K_p}{K_i}s+1}{\frac{L}{K_i}s^2+\frac{R+K_p}{K_i}s+1} \tag{2.10}$$

$$\left.\frac{I_o(s)}{I_{ref}(s)}\right|_{PDF} = \frac{1}{\frac{L}{K_i}s^2+\frac{R+K_p}{K_i}s+1} \tag{2.11}$$

$$\left.\frac{I_o(s)}{I_{ref}(s)}\right|_{PI(standard)} = \frac{\frac{1}{\omega_c}s+1}{\frac{1}{\omega_{nPI}^2}s^2+\frac{2\zeta_{PI}}{\omega_{nPI}}s+1} \tag{2.12}$$

$$\left.\frac{I_o(s)}{I_{ref}(s)}\right|_{PDF(standard)} = \frac{1}{\frac{1}{\omega_{nPDF}^2}s^2+\frac{2\zeta_{PDF}}{\omega_{nPDF}}s+1} \tag{2.13}$$

$$\omega_c = \frac{K_i}{K_p} \tag{2.14}$$

$$\omega_{nPI} = \omega_{nPDF} = \sqrt{\frac{K_i}{L}} \tag{2.15}$$

$$\zeta_{PI} = \zeta_{PDF} = \frac{R+K_p}{2\sqrt{K_i L}} \tag{2.16}$$

The closed loop transfer function (2.10) using a PI controller has a zero at ω_c that depends on the controller parameters. The effect of this zero is the reduction in the rise time and increase in the speed of response. If ω_c is less than ω_{nPI}, it causes overshoot in the system that depends on the degree to which ω_c is smaller, even though the closed loop poles are critically damped. Since the machine parameters vary due to saturation and cross-coupling effects, the presence of a closed loop zero imposes an extra constraint to the controller design, and thus it is undesirable. Additionally, the gain parameter K_p in PI controller cannot be negative, otherwise the initial response would go in opposite direction until the voltage command generated by integral gain becomes higher than the proportional part. In contrast, the PDF controller has a parameter K_p that acts similar to the feedback resistance (Fig. 2.6b). The response with a negative value of K_p would be as if the resistance, R is reduced, which means a sluggish response. Therefore, due to these reasons, the PDF controller is selected.

2.4.2 Controller Design

As discussed earlier, the controller should be able to increase the speed of response for a slower system and reduce the speed of response for a faster system. Based on the analysis presented in section 2.3, the accuracy of measurement for a system with a time constant of $100ms$ at a sampling time of $25\mu s$ is good enough. Thus, in this thesis, one of the controller design criteria is to have a response similar to such system. The desired settling time of the controlled system can be considered to be five times this time constant. The design equations for the controller can be obtained from (2.15) and (2.16); and they are given by (2.17) and (2.18).

$$K_i = L\omega_n^2 \tag{2.17}$$

$$K_p = 2\zeta\sqrt{K_i L} - R = 2\zeta L\omega_n - R \tag{2.18}$$

These equations show that the calculation of controller gains require information on the machine resistance and inductance. The system damping ratio, ζ and the natural frequency of oscillation, ω_n are defined explicitly based on the settling time. As seen from (2.15) and (2.16), these parameters change with the change in system parameters. In addition, when ζ falls below unity, there will be overshoot, which means that the transient has a faster rise as well as oscillations. In order to avoid such oscillations, ζ should be remained greater than unity even for extreme cases.

When ζ is greater than unity, the location of closed loop poles are given by (2.19).

$$p_{1,2} = -\zeta\omega_n \pm \omega_n\sqrt{\zeta^2 - 1} \tag{2.19}$$

In order to define the values of ζ and ω_n in terms of the required settling time (with no overshoot), the roots of the characteristic equation in (2.13) are made far from each other. When the value of ζ is two, the location of the closed loop poles are at $-3.732\omega_n$ and $-0.268\omega_n$. The first pole is much further from the origin than the second pole. Thus, the closed loop system can effectively be treated as a first order system with a time constant of $1/(0.268\omega_n)$. Considering the desired settling time to be five times of this time constant, the natural frequency ω_n can be calculated.

The remaining unknowns in (2.17) and (2.18) are L and R. In order to obtain a rough estimate of these parameters, a pulsed voltage of small magnitude that applies roughly 10%-20% of the rated current is applied to the machine, and (2.7) or (2.8) is used to measure the machine resistance and inductance. These estimates are rough, and can be highly inaccurate as discussed in section 2.3. The efficacy of these rough estimates on the controller performance is evaluated by analyzing the performance of the controller when these parameters are varied. Since the estimation in R is accurate enough and it is not affected by saturation and cross-coupling effects, only the inaccuracy in L is analyzed.

Consider that the actual inductance is 'n' times the estimated value. It may be due to estimation inaccuracy or due to saturation effects. Relations (2.15) and (2.16) are used to see its effect in

Table 2.3: Effect of variation in inductance on ω_n and ζ.

n	Inductance	Natural frequency	Damping ratio
1	L	ω_n	ζ
2	2L	$0.7071\omega_n$	0.7071ζ
0.05	0.05L	$4.472\omega_n$	4.472ζ

the closed loop ζ and ω_n. Table 2.3 presents the variation in ζ and ω_n with respect to the design specification for different values of 'n'. It shows that both the natural frequency and damping ratio varies when the actual inductance differs from the rough estimates. However, the ratio of ζ to ω_n remained constant.

In order to see the effect of variation in machine inductance on the closed loop response, the controller parameters are computed using the desired settling time and nominal value of inductance for an arbitrary test system. Two more test systems are considered with different values of inductances. These additional test systems can be considered as the variation in system time constant due to saturation effects. MATLAB Simulink is used to simulate the response of these three different systems using the same controller. For the test case, the nominal value of machine inductance is $100\ mH$ and the settling time is chosen to be 1 second. Fig. 2.7 compares the step responses with the same controller for machine inductances of $100\ mH$, $5\ mH$ and $200\ mH$. The additional test systems have very large deviation in inductance compared to the nominal value. The plot shows that even though the machine inductance varies by a very high degree from the nominal value, the controller adjusts its output to obtain almost the same response. Thus, this shows that a very rough estimate of inductance is enough for the controller design.

The controller design procedure can be summarized as follows.

(1) Choose the desired settling time (T_s) based on the accuracy requirement.

(2) Compute the value of natural frequency (ω_n) from the following equation using the T_s for ζ=2.

$$\omega_n = \frac{5}{0.268T_s}$$

(3) Obtain a rough estimate of machine inductance and resistance using the voltage pulse based method.

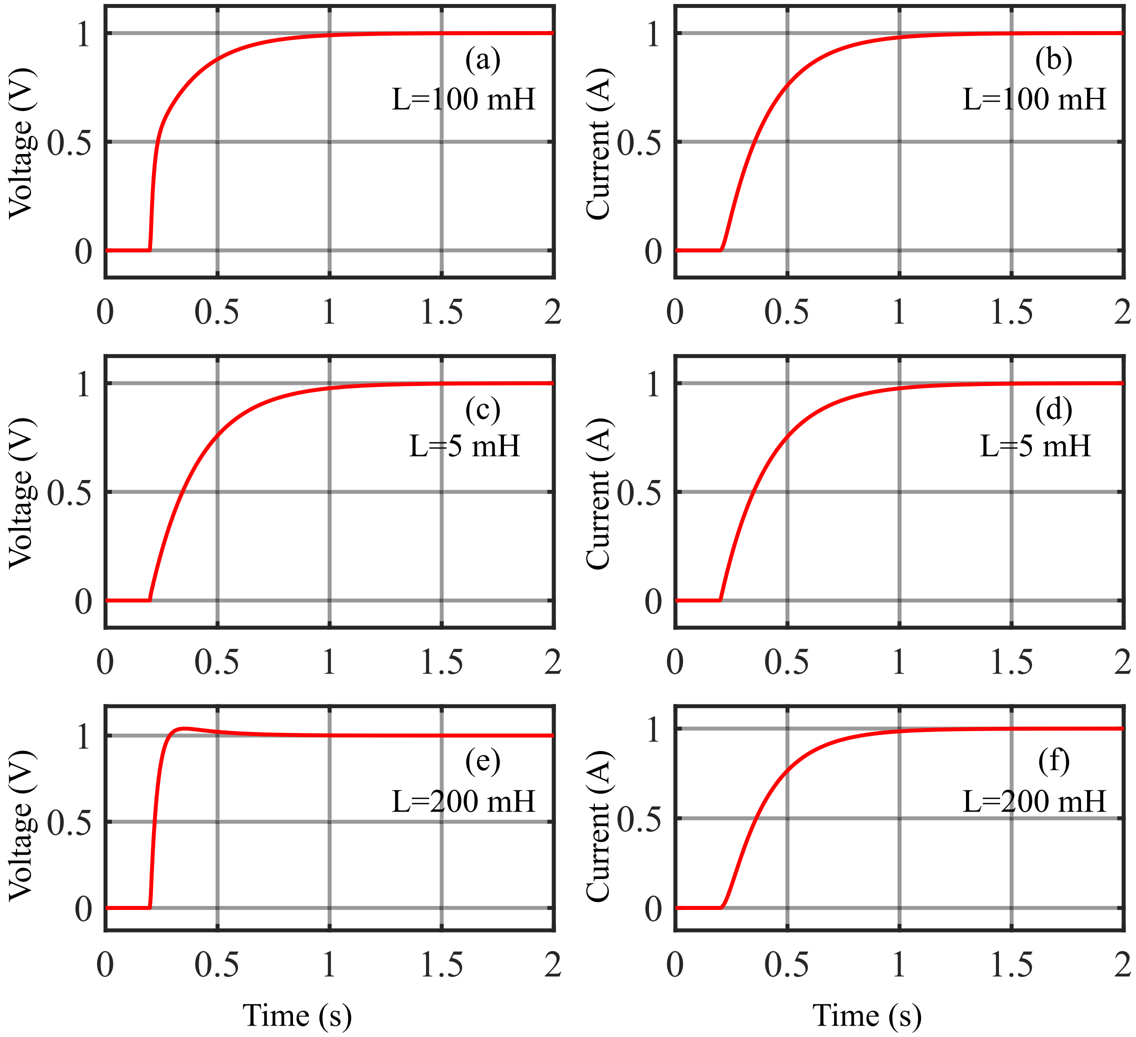

Fig. 2.7: Step response of a system with the same controller when its inductance varies from nominal value of 100 mH to 5 mH and 200 mH. (a), (c), (e) are the controller outputs and (b), (d) ,(f) are output currents.

(4) Compute the controller parameters using (2.17) and (2.18) replicated below.

$$K_i = L\omega_n^2$$

$$K_p = 2\zeta\sqrt{K_i L} - R = 2\zeta L\omega_n - R$$

A similar procedure can be repeated for a fixed current controller. However, the natural frequency ω_n for a fixed current controller should be much higher compared to the pulsed current controller. Based on the literature, in order to have no effect of the pulsed current controller on the fixed current to be controlled, the closed loop bandwidth of the fixed current controller is chosen to be ten times of ω_n.

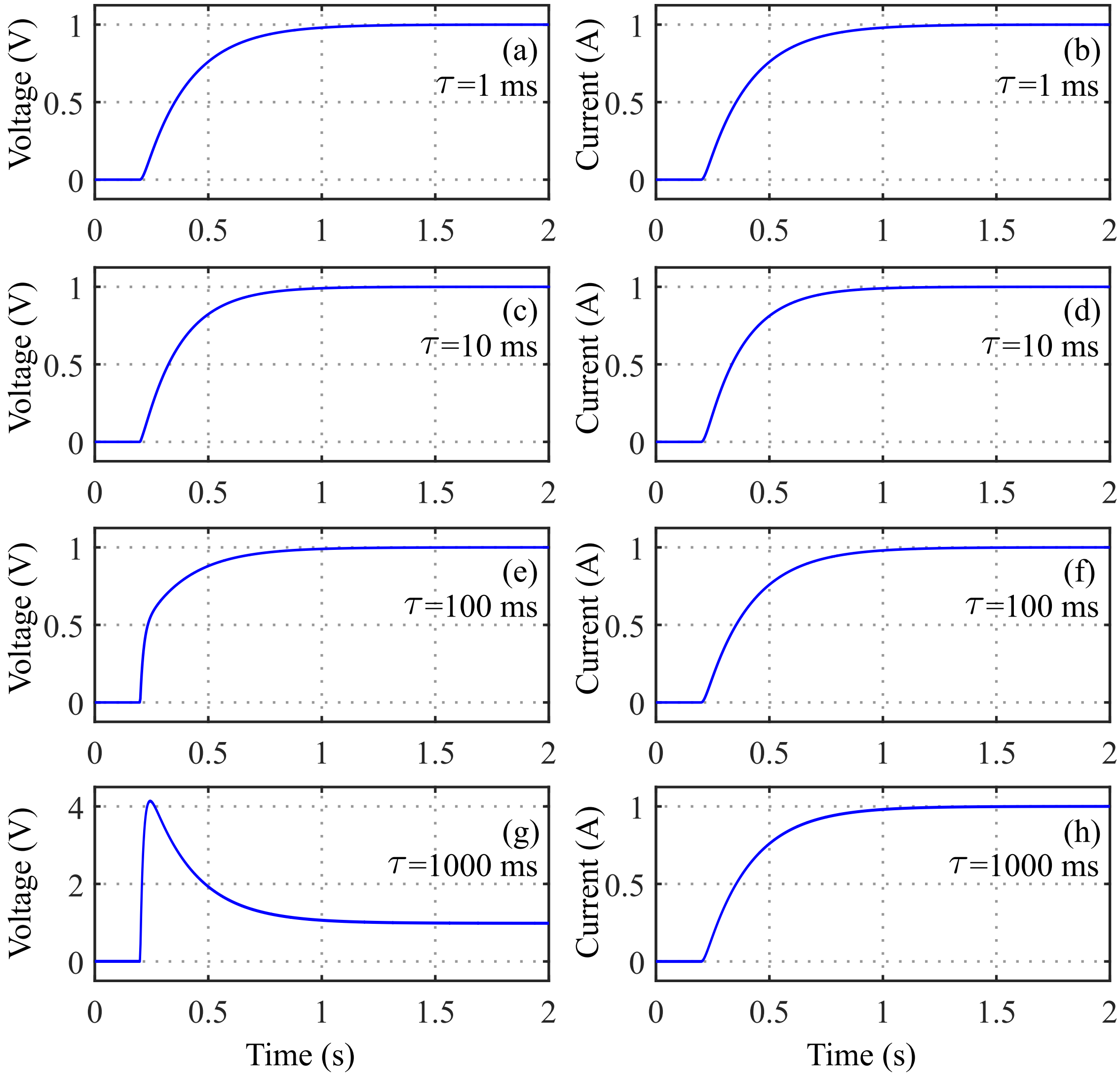

Fig. 2.8: Controller output and the system response for four different machines with the controller parameters designed to have a settling time of 1 second.

In order to validate the proposed controller design technique, the proposed controller design procedure is used to design controllers for four different machines with time constants of 1 ms, 10 ms, 100 ms and 1000 ms to have a settling time of 1 second. MATLAB Simulink is used to simulate the responses of the machines with the designed controller. Fig. 2.8 shows the controller (voltage) and system (current) outputs. It shows that the designed controller is able to slow down the response for the machine with smaller time constant. In the same way, the designed controller is able to speed up the response for the machine with larger time constant. This shows that the proposed controller design procedure can be applied to a wide range of machines.

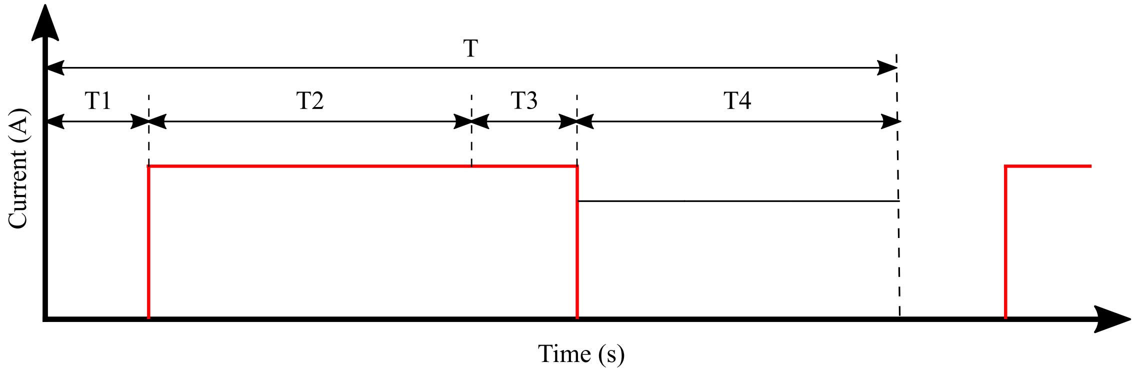

Fig. 2.9: Timing diagram of the pulsed reference current to calculate the inductances online in a real-time processor.

2.5 Real-Time Implementation

Based on the discussion presented in 2.4.2, the system settling time can be made constant irrespective of the variation in machine inductance due to saturation. Such a property is useful for real-time implementation of the proposed technique. The current dependent flux linkages defined by (2.7) and (2.8) can be written as (2.20) and (2.21).

$$\lambda_d = \int_0^t v_d(\tau)d\tau - R_s \int_0^t i_d(\tau)d\tau \tag{2.20}$$

$$\lambda_q = \int_0^t v_q(\tau)d\tau - R_s \int_0^t i_q(\tau)d\tau \tag{2.21}$$

In these forms of the flux linkage equations, the voltages and currents can be integrated separately. Fig. 2.9 shows the timing diagram of the reference current pulse for real-time implementation. The total pulse period 'T' is divided into four periods. During the first period 'T1', the reference current is zero. During this period, the three phase currents and voltages are measured and averaged to find the offsets in the measurement system. In the beginning of the period 'T2', a current of desired magnitude is given as a reference. At the same time, integration of the measured voltages and currents are started and continued until the end of this period. The controllers are designed to reach the steady state at the end of this period. The offsets calculated during the period 'T1' are subtracted from the measured signals during the integration period. In the period 'T3', the signals are averaged to compute the resistance. In the beginning of the period 'T4', the reference current is set back to zero, and the measured voltages and currents are integrated till the end of this period. The offsets are subtracted from the measured signals during the integration period. At the end of each pulse period 'T', the rising and falling edge flux linkages are calculated using (2.20) and (2.21). The rising edge and falling edge flux linkages are averaged to find the flux linkage at that current level.

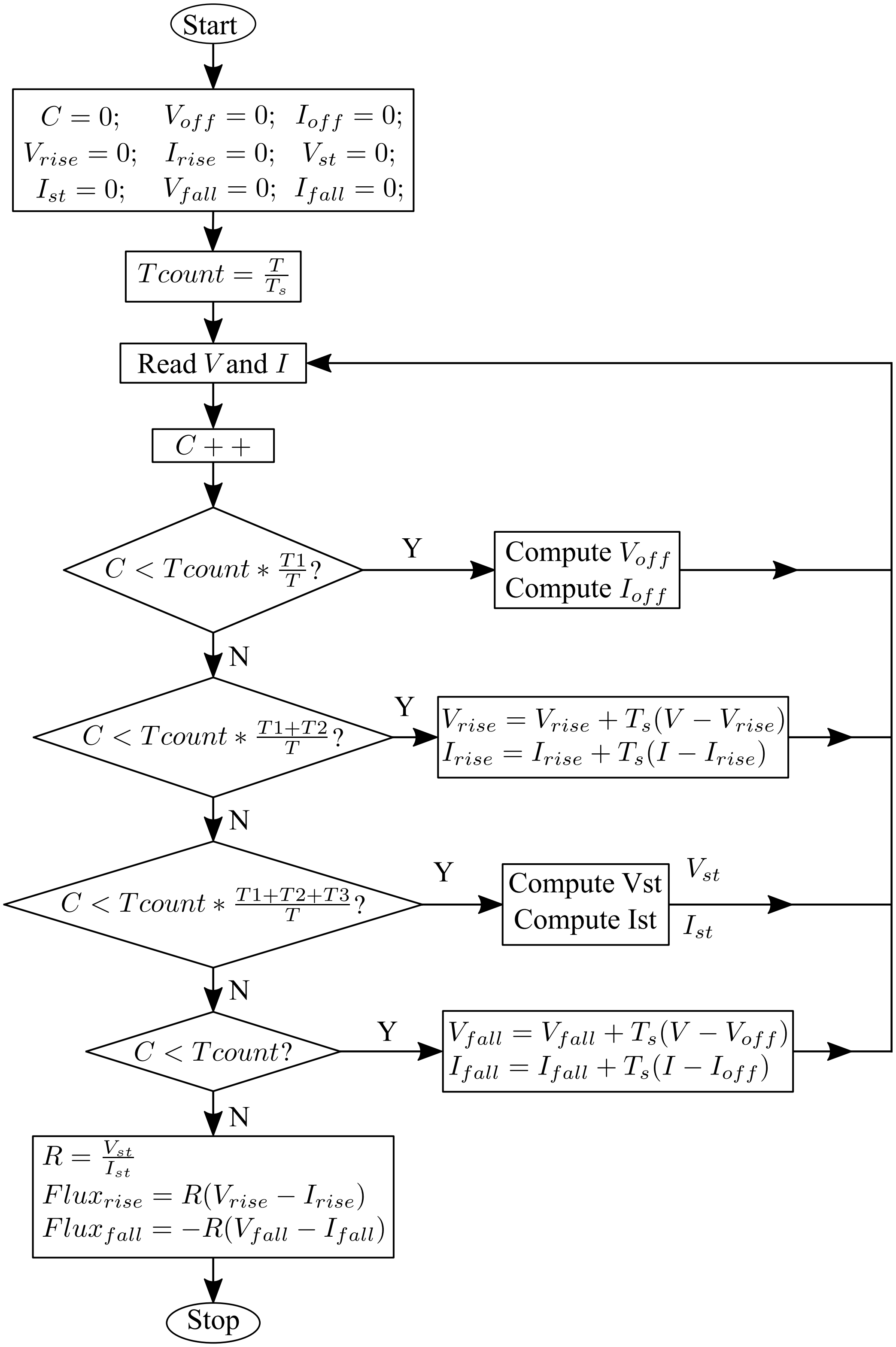

Fig. 2.10: Flowchart showing the implementation of the proposed algorithm in a real-time system.

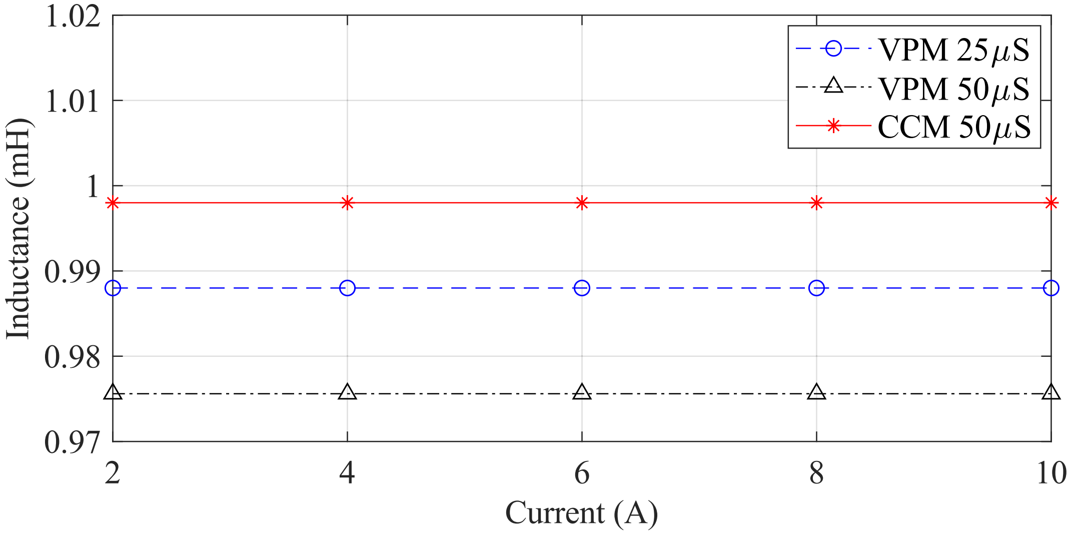

Fig. 2.11: Comparison of inductances obtained using VPM and CCM obtained from simulation in MATLAB simulink for a machine with an inductance of 1 mH.

Fig. 2.10 presents the flowchart of the procedure for the real-time implementation of the proposed method. All the storage variables are cleared before the beginning of the period 'T'. 'C' is the counter used to keep records of the transition between various periods. V_{off} and I_{off} are the offset voltages and currents in the measurement system, V_{rise} and I_{rise} are rising edge voltage and current integrals, V_{fall} and I_{fall} are the falling edge voltage and current integrals, V_{st} and I_{st} are the steady state voltage and current. During each pulse period, no storage of the signals are required for averaging the data. At the end of the period 'T', an average of the flux linkage is calculated and stored along with the current levels. The process is repeated for different current levels to obtain the full flux linkage map. The whole process can be automated to obtain the full flux linkage map. It can be then used to calculate various inductances as defined in [65]. To obtain the flux linkages and inductances at different rotor positions, the process is repeated at each rotor position.

2.6 Computer-Aided Simulation

In order to compare the voltage pulse method and current control method, a permanent magnet synchronous machine from MATLAB SimPowerSystems blockset with 1 mH inductance and 1 Ω resistance is simulated to measure the inductances. The simulation time step is 1 μs, and the magnet flux linkage is set to zero in the simulation model to represent a synchronous reluctance machine. Fig. 2.11 compares the inductances obtained using the VPM and CCM. Details on the VPM is presented in [64]. For the VPM, results are obtained for sampling times of 25 μs and 50 μs. The settling time of the machine for a voltage pulse is 5 ms (time to reach 99.3$\%$ of the final value). For

Fig. 2.12: Experimental setup. (1) Test SynRM. (2) dynamometer. (3) Real-time controller. (4) Inverter. (5) Sensors. (6) Data Acquisition System.

the current control method, the controllers are designed to obtain a settling time of 70 ms. Fig. 2.11 shows that the inductances obtained using CCM with a higher sampling time (50 μs) is closer to the actual inductance compared to the inductances obtained from VPM with a lower sampling time (25 μs). Since the SimPowerSystems machine model has no saturation, the measured inductances are constant.

2.7 Experimental Setup and Results

Fig. 2.12 shows the experimental setup to measure the SynRM flux linkages and inductances. It consists of a test SynRM coupled to a dynamometer with a clamp to lock the rotor, a voltage source inverter (SKM50GB123D), sensors (LV20P and LA100-P), real-time controller (OP5142 Wanda 4U) and a data-acquisition system (SL1000). The data acquisition system is used to record the dq voltages and currents sent by the controller that is used later to verify the flux linkages computed online. As discussed in section 2.4, a pulsed voltage of small magnitude is applied to the machine to obtain a rough estimate of the machine inductance and resistance. These values are used to calculate the controller parameters. As shown in Fig. 2.5, to measure the d-axis flux linkage and inductance, a pulsed reference current is applied in d-axis while controlling the current in q-axis to a fixed value. PDF controllers are used to generate the references v_d^* and v_q^*. The reference dq voltages are converted to the abc frame using a $dq - abc$ transformation. An encoder is used to get the position information for $dq - abc$ transformation. The reference abc voltages are supplied to the

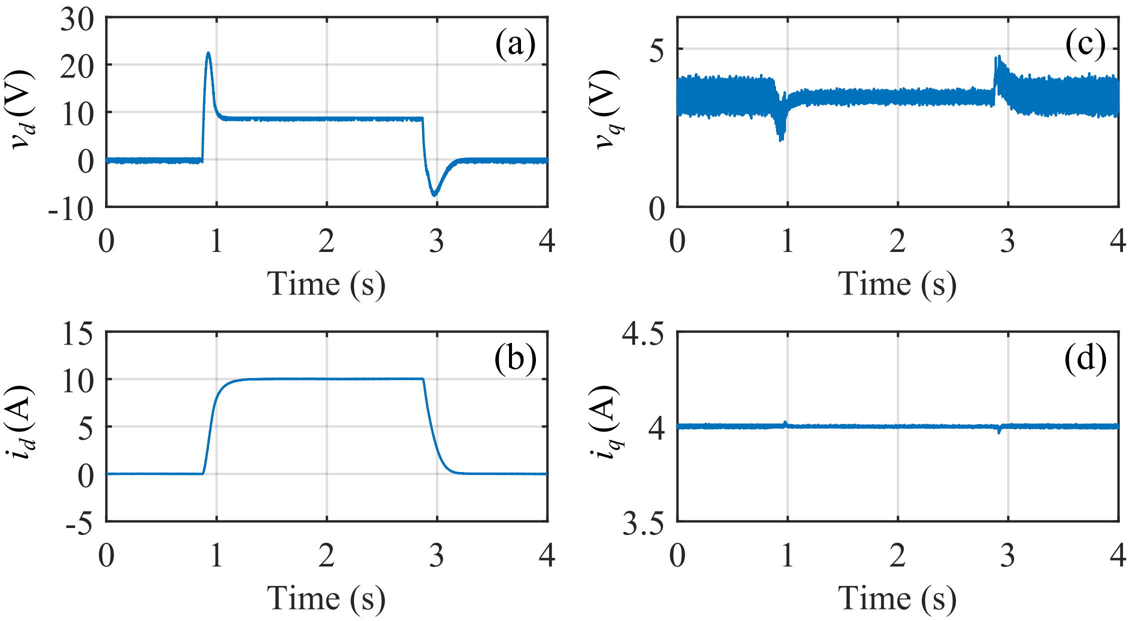

Fig. 2.13: System response for an arbitrary operating point when a pulsed reference i_d is applied at a fixed reference i_q. (a) v_d. (b) i_d. (c) v_q. (d) i_q.

PWM generator to generate gating signals for the inverter. The three phase currents are measured and fed back to the controller for the closed loop operation.

Fig. 2.13 presents the voltage and current waveforms for an arbitrary operating point of $i_d = 10A$ and $i_q = 4A$. It shows that the voltage v_d applied by the controller during the transient is higher compared to the steady state v_d. It is because the machine time constant for this operating point is very large, and an application of steady state voltage from the beginning of the pulse will slow down the response. The plot also shows that the i_q is controlled to $4A$ with a very small ripple. The ripple magnitude depends on the switching frequency and DC bus voltage. In the experiment, the switching frequency was 10 kHz, and the DC bus voltage was reduced to 80 V compared to the nominal voltage of 350 V. The d-axis flux linkage at the operating point of $(i_d, i_q) = (10A, 4A)$ is obtained applying (2.20) to the measured voltages and currents in the real-time processor. To obtain the d-axis flux linkage map for the entire dq plane, the reference operating point is changed and the process is repeated. A similar procedure is repeated to obtain the q-axis flux linkage map.

Fig. 2.14 and Fig. 2.15 presents the experimental results on the variation of q-axis and d-axis flux linkages with i_d and i_q. It shows that the q-axis flux linkage shows more saturation effects than the d-axis flux linkage. Additionally, the cross-coupling effects are more in the q-axis than the d-axis. Comparing Fig. 2.14a and Fig. 2.14c, while both present the q-axis flux linkage curves for negative q-axis currents, the cross-coupling effects of i_d depend on both its magnitude and direction. For the same magnitude of i_d, the change in the q-axis flux linkage depends on its direction. A

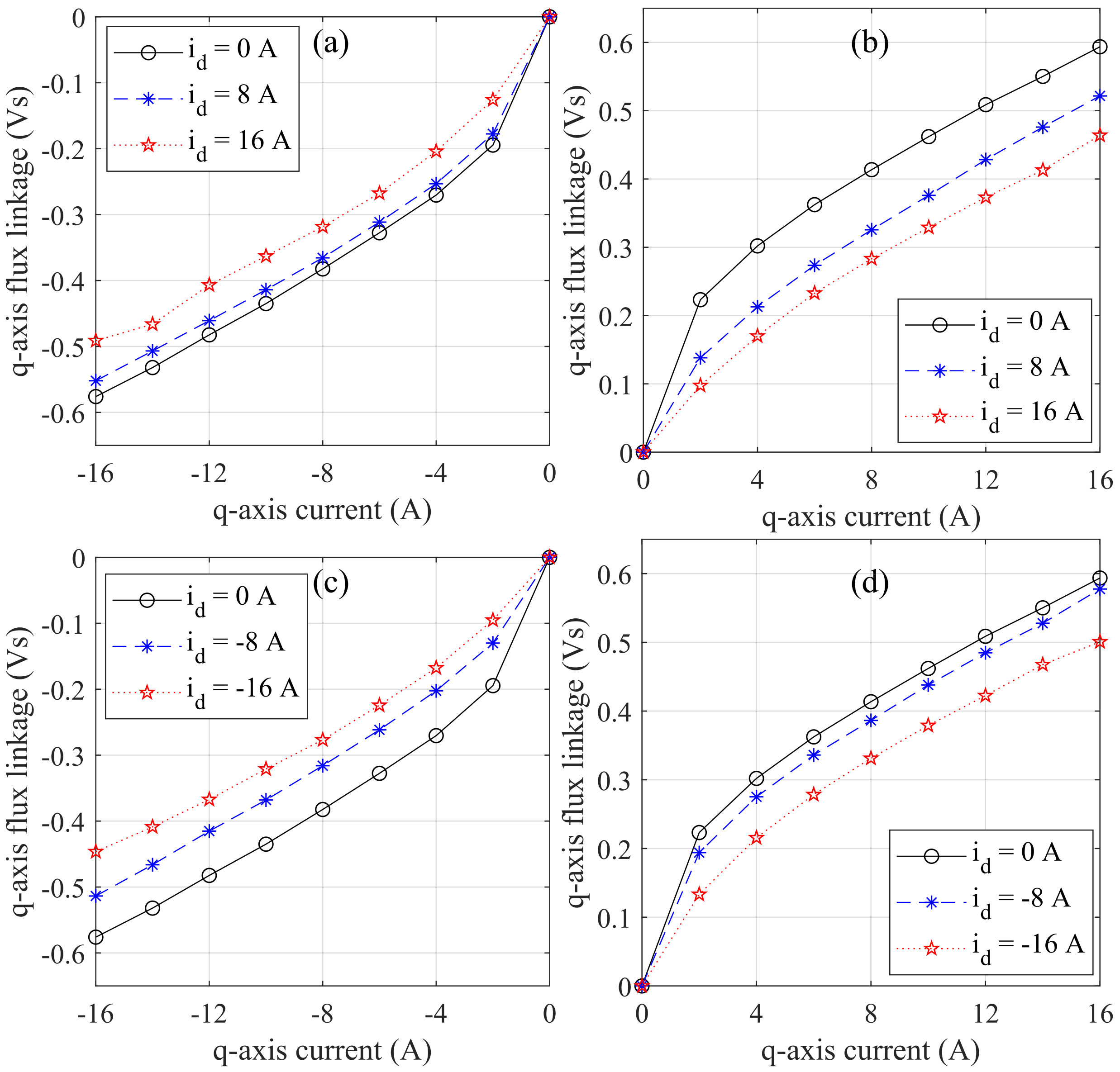

Fig. 2.14: Q-axis flux linkage, λ_q for various ranges of i_d and i_q. (a) Negative i_q and positive i_d. (b) Positive i_q and positive i_d. (c) Negative i_q and negative i_d. (d) Positive i_q and negative i_d.

similar effect can be observed while comparing Fig. 2.14b and Fig. 2.14d, Fig. 2.15a and 2.15c, and 2.15b and 2.15d. In an ideal symmetric machine, the effect of i_d or i_q on the cross-coupling flux linkage does not depend on its direction. This remains true for the synchronous reluctance machine with a symmetrical geometry. The flux linkages obtained by averaging the flux linkages for all the rotor positions must show symmetry. However, for any particular rotor position, it may not be true. The results presented in Figs. 2.14 and 2.15 are for a particular rotor position. For some rotor positions, while magnetic flux in the machine is flowing due to current in one axis, if current in another axis is applied, the resultant magnetic flux may depend on its direction.

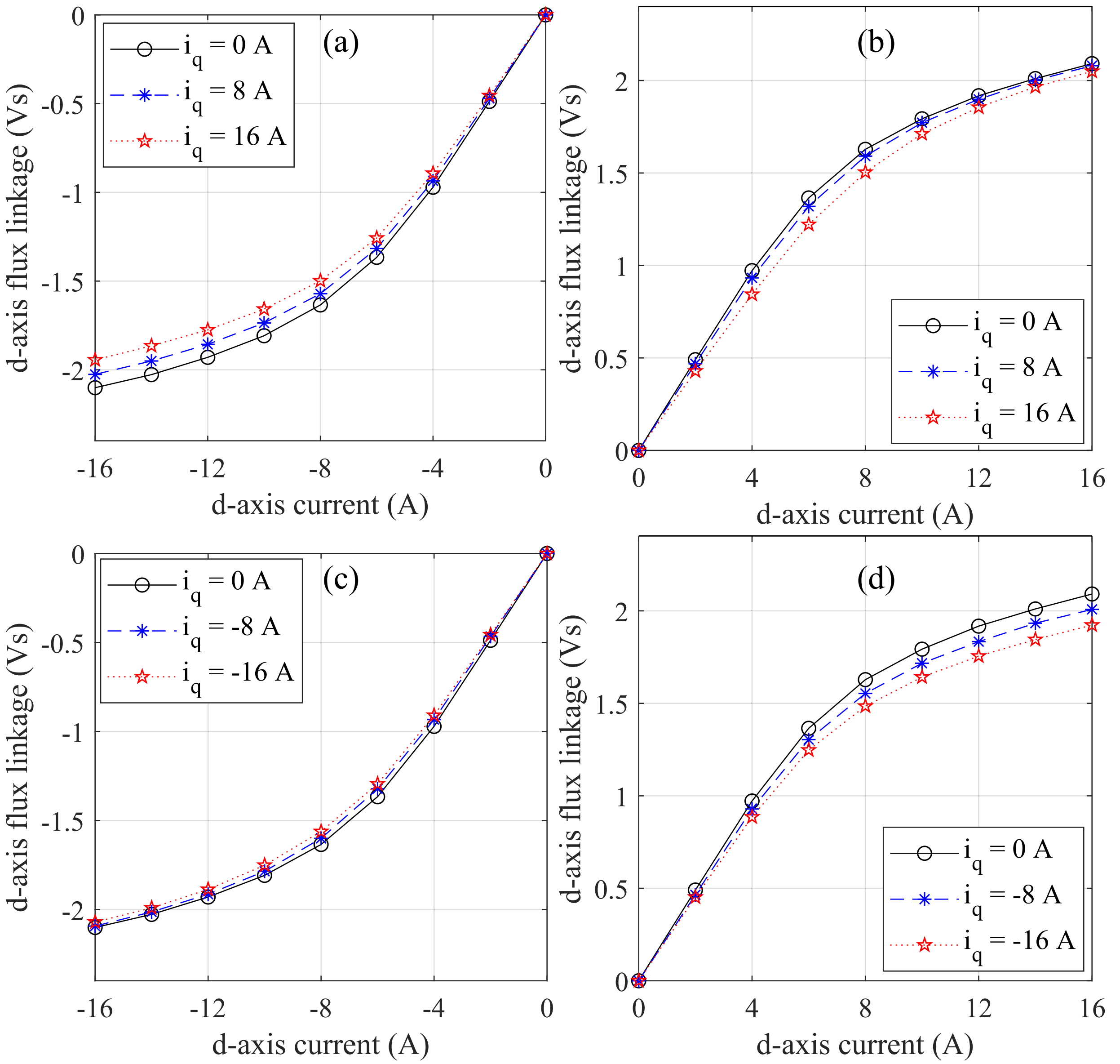

Fig. 2.15: D-axis flux linkage, λ_d for various ranges of i_d and i_q. (a) Negative i_d and positive i_q. (b) Positive i_d and positive i_q. (c) Negative i_d and negative i_q. (d) Positive i_d and negative i_q.

In order to validate the nature of the results presented in Figs. 2.14 and 2.15, FEA simulation results for flux linkages at different rotor positions are obtained from MotorSolve 6.0.1. The simulation results are presented in Fig. 2.16 and Fig. 2.17. The simulation results presented are not to validate the experimental result, instead, to study the nature of the curves. Based on the simulation results, a similar variation of dq flux linkages are obtained at rotor positions where the rotor d-axis is not aligned perfectly with the center of the stator teeth. The curves presenting dq flux linkages vary with the rotor position. In advanced spatial models considering variation of fluxes and inductances with rotor position, all these effects are taken into account.

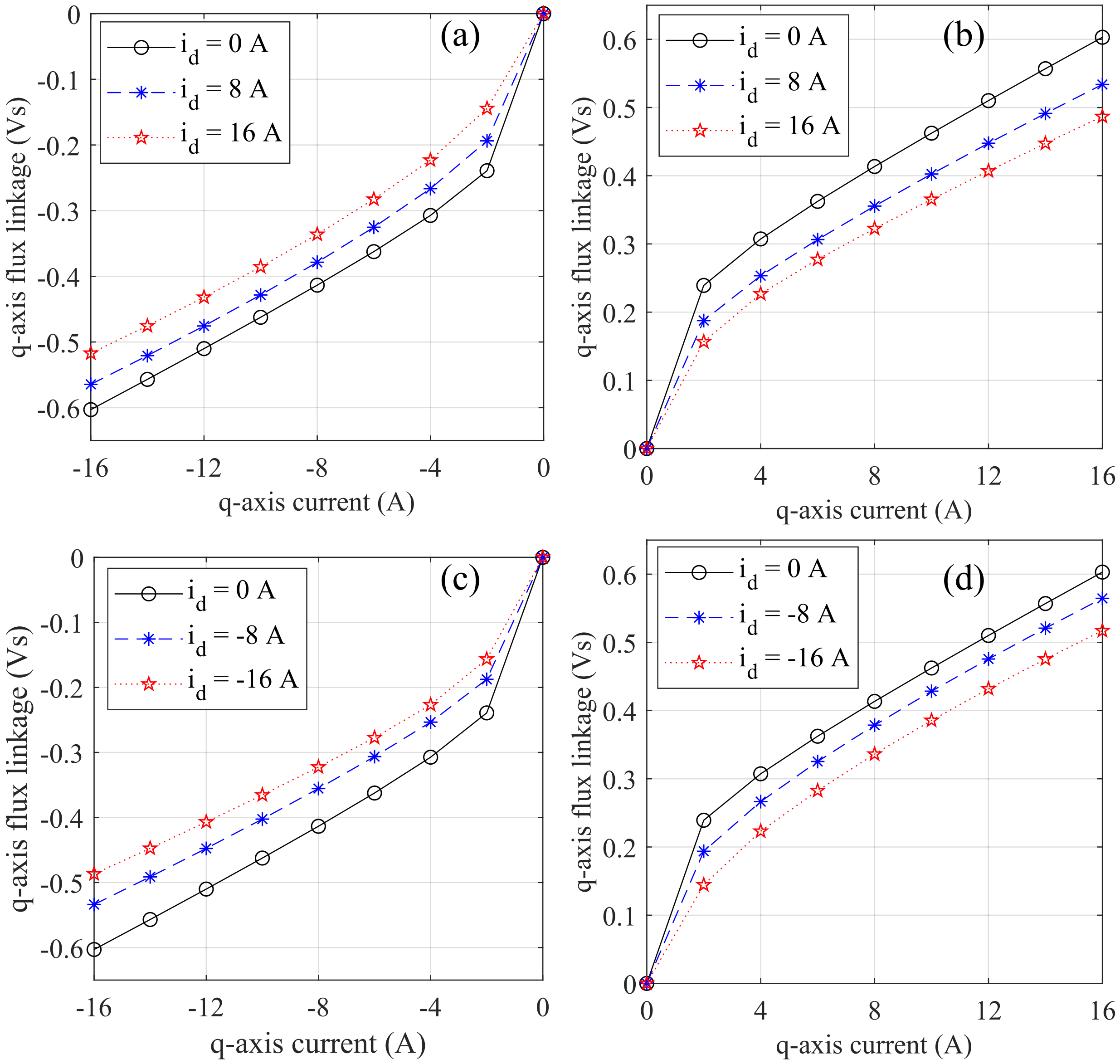

Fig. 2.16: Q-axis flux linkage obtained from FEA simulation in MotorSolve (DQ analysis option).

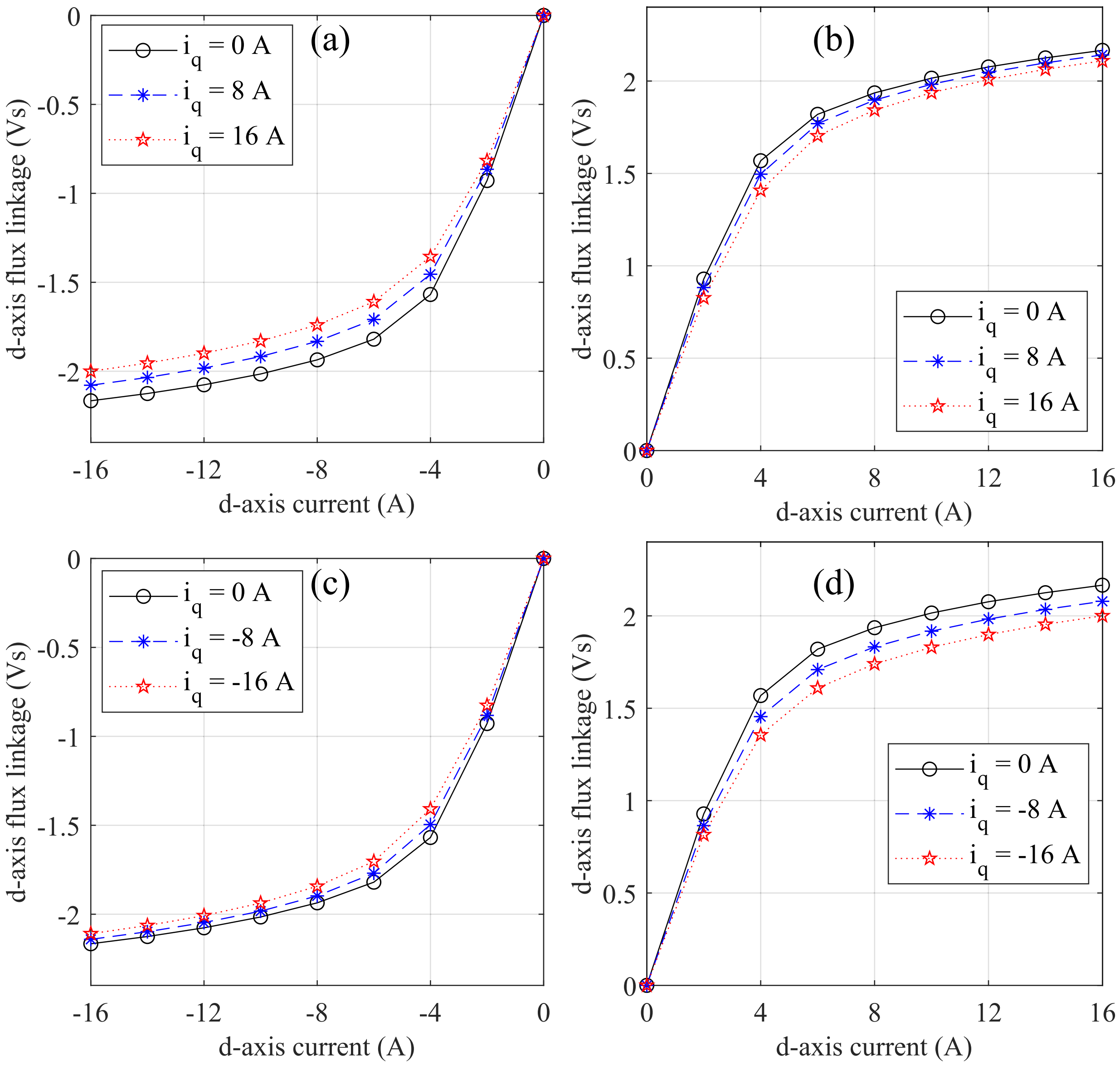

Fig. 2.17: D-axis flux linkage obtained from FEA simulation in MotorSolve (DQ analysis option).

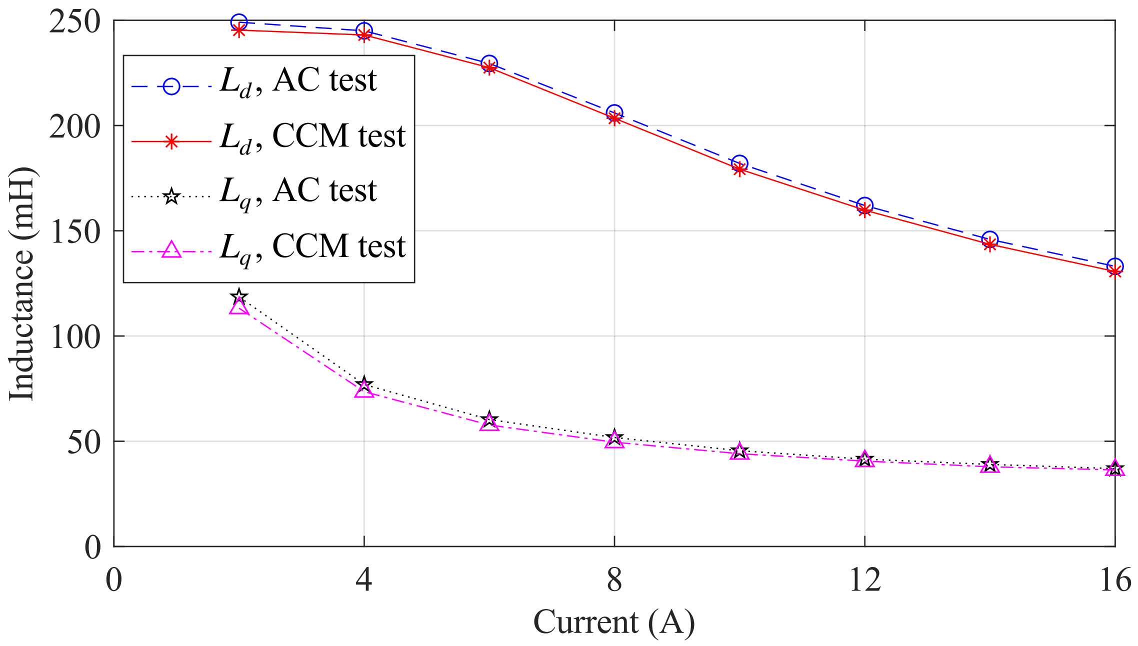

Fig. 2.18: Comparison of L_d and L_q obtained using the proposed CCM with the standard AC test.

2.8 Comparison with Existing Methods

Once the flux linkages are calculated, different inductances as described in [65] can be calculated. In order to have a comparison of the inductances obtained from the proposed method with a standard available method, standard locked rotor AC tests for the inductances are performed on the same machine as per IEEE P1812$^{\text{TM}}$/D2 [79]. The rotor is locked at a position with the rotor d-axis aligned to the stator A-phase. To measure the d-axis inductances, A variable frequency and variable magnitude AC power supply (MX30-3Pi from California Instruments) is used to supply a sinusoidal voltage at the rated frequency (28.33 Hz) to the machine with A-phase connected to the positive, and B- and C-phases connected to the negative of the power supply. The reactive power at the fundamental frequency is measured using a YOKOGAWA WT3000 precision power analyzer. To measure the q-axis inductances, the positive of the power supply is connected to the B-phase, and the negative of the power supply is connected to the C-phase with the same rotor position as during the d-axis inductance measurement condition. The dq inductances are computed using the following equation.

$$L_d (or L_q) = \frac{Q_1}{2\pi f I_{rms1}^2} \tag{2.22}$$

where, Q_1 is the reactive power at the fundamental frequency, f is the frequency of the applied voltage, and I_{rms1} is the rms current at the fundamental frequency.

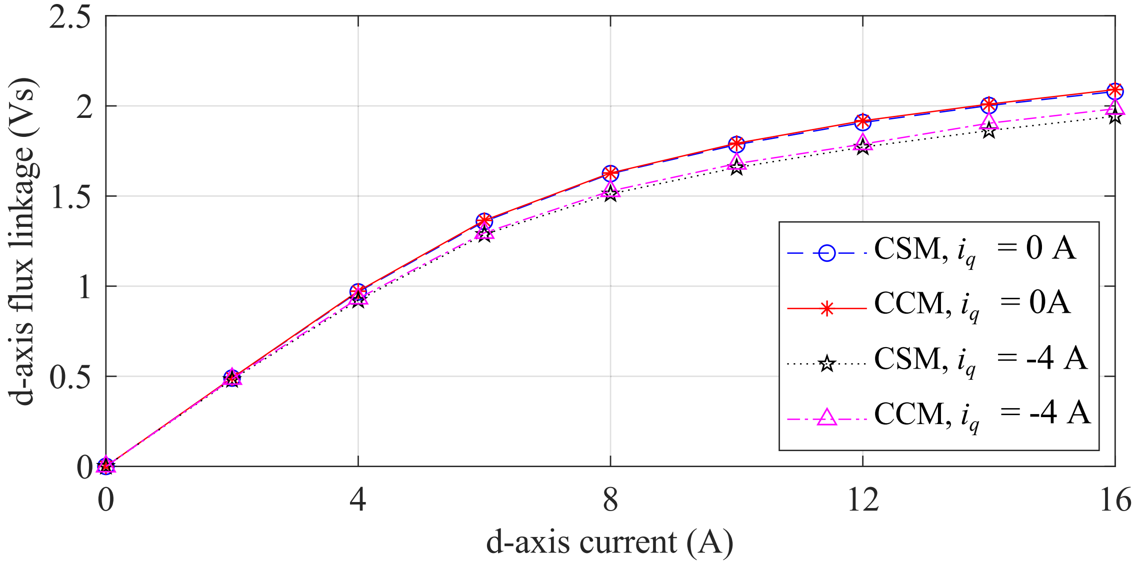

Fig. 2.19: Comparison of d-axis flux linkage at two different magnitudes of i_q obtained using the proposed CCM with the CSM.

A comparison of self inductances L_d and L_q obtained from the proposed test with the AC test are shown in Fig. 2.18. It shows that the test results using the proposed method agrees quite well with the AC test results. The deviation in the inductances with two different tests might arise from several factors. One of the factors might be the accuracy associated with the current and voltage sensors used in the proposed test. Since the custom built sensors are designed to measure currents and voltages for a wide range (30 A and 100 V in the present case), the accuracy of the industrial power analyzer used in the AC test is better. Another reason for the deviation might be due to the difference in the way the machine responds for positive and negative current. The AC test gives an average effect of positive and negative supply to the machine while the current pulse method measures a different inductance for positive and negative currents. The test results also show that both the inductances, L_d and L_q decreases with an increase in i_d and i_q respectively.

The dq axes flux linkages of the test motor including cross-saturation effects are also measured using the CSM. Details on the underlying principle behind the CSM are described in [66], and this thesis followed the CSM presented in the same paper. Figs. 2.19 and 2.20 presents the comparison of dq flux linkages at two different magnitudes of i_q and i_d obtained using the proposed current control method with the constant speed method. In Fig. 2.19, the d-axis flux linkage for the same magnitude of i_d is reduced when i_q is applied to the machine. This reduction is due to saturation of the common magnetic path by i_q, the so called cross-magnetizing effect. A similar effect is seen in Fig. 2.20 in the q-axis flux linkage when i_d is applied. There is a nominal difference in the magnitude of the flux linkage obtained from CSM with the one obtained from the proposed current pulse method. However, the difference is less than 2%. It should be noted that the CSM

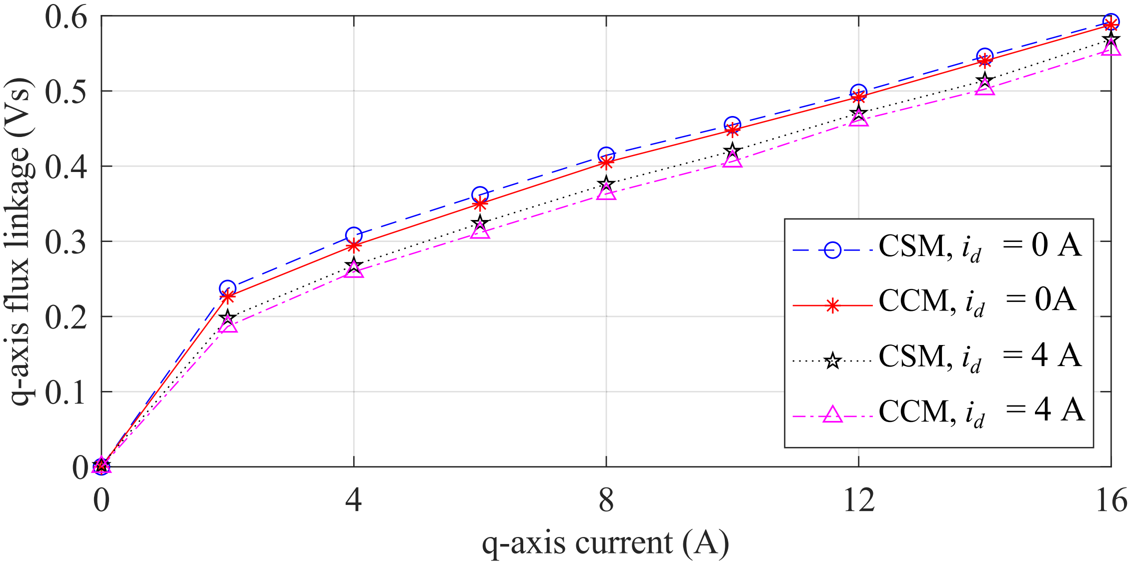

Fig. 2.20: Comparison of q-axis flux linkage at two different magnitudes of i_d obtained using the proposed CCM with the CSM.

result is an average flux linkage around rotor positions, while the proposed method gives position dependent flux linkages. Based on the experiments performed at different rotor positions and current magnitudes, the variation in inductances with rotor position is lower than 2% for L_d and 6% for L_q. For the comparison in Figs. 2.19 and 2.20, the measurements at the rotor position with rotor d-axis aligned with stator phase A axis is used.

Thus, the proposed method is useful to measure the flux linkage and inductance maps using a real-time system. This method does not require post processing of a huge data set. Compared to the pulsed voltage reference method, the proposed method improves the accuracy for machines ranging from very low to high time constants. Although the proposed method is capable of measuring the flux linkage and inductance characteristics at any rotor position, this thesis presented results for the d-axis flux linkage measured at position 90° (d-axis aligned to phase A axis) and q-axis flux linkage measured at position 180° (q-axis aligned with the phase A axis).

2.9 Summary

Flux linkage and inductance measurement methods are evolving to meet the needs in machine and drive designs. To obtain the flux linkage and inductance map of a machine at standstill, conventionally, a pulsed voltage is applied in one axis while the current in another axis is controlled to remain constant. This method requires a higher sampling rate for a machine with a lower time constant and a longer pulse duration for a machine with a higher time constant. This makes it unsuitable for measurements using a real-time system. Moreover, the current flowing in the d-axis induces a voltage in the q-axis due to the inverter dead time and device drops. It puts a limitation to the measurement range in the $i_d i_q$ plane.

This chapter proposed a novel current control based standstill method to measure the flux linkage of special electric machines with a SynRM as a test machine. In the proposed method, instead of a voltage pulse as in the conventional test method, a current pulse in closed loop is applied in one axis while controlling the current in another axis. Due to the use of current control, flux linkage at any operating point in the dq plane can be measured. In addition, the transient response of the machine can be modified such that an adequate number of measurement samples are available during the transient, making it suitable to use in a real-time system for an online measurement of flux linkages. This chapter also presented in detail the analysis and design of the controllers required in the proposed method. Finally, the chapter presented an algorithm to implement the proposed method using a real-time system. The proposed method is verified using an experiment performed on a test machine. In order to assess the efficacy of the proposed method, the results obtained from the proposed method are compared with the results obtained from the standard AC standstill test and constant speed method. The results show that the proposed method is useful to obtain the flux linkage characteristics of special electric machines like SynRM and IPMSM using a real-time system.

Based on the work presented in this chapter, the following research papers are published [16,80].

- R. Thike and P. Pillay, “Automated Current Control Method for Flux-Linkage Measurement of Synchronous Reluctance Machines,” in IEEE Transactions on Industry Applications, vol. 56, no. 2, pp. 1464-1474, March-April 2020, doi: 10.1109/TIA.2020.2967689.
- R. Thike and P. Pillay, “Automatic Inductance Measurements of Synchronous Reluctance Machines Including Cross-Saturation Using Real-Time Systems,” 2018 IEEE Energy Conversion Congress and Exposition (ECCE), Portland, OR, 2018, pp. 6121-6127, doi: 10.1109/ECCE.2018.8558407.

Chapter 3

Torque Performance of a Segmented Pole SynRM with Grain-Oriented Laminations

A high performance SynRM exhibits a high rotor anisotropy in order to have performance comparable to PMSMs. The design objective of a SynRM aims for a higher saliency ratio to improve the torque density. The saliency ratio in a SynRM can be improved by utilizing grain-oriented laminations. This chapter presents the study on torque performance of a segmented-pole SynRM with cold rolled grain-oriented (CRGO) laminations over a similarly sized regular SynRM with cold rolled non-grain-oriented (CRNGO) laminations having the same geometric data. The torque characteristics of both the SynRMs are studied to obtain the MTPA characteristics. This chapter also studies the torque ripple of the SynRMs at various operating points including the extended speed region. A static measurement method is proposed to measure the torque angle and torque ripple in SynRMs.

3.1 Background

Cold-rolled grain-oriented (CRGO) electrical steels are high quality anisotropic magnetic materials with higher permeability in the rolling direction. The use of CRGO steel is uncommon in rotating electrical machines. A segmented-rotor modular switched reluctance motor with high torque and low torque ripple is presented in [81]. In [23], it is shown that the saliency ratio of a SynRM can be improved by using CRGO steel. In the design presented for a four pole SynRM rotor, each rotor lamination is divided into four sections, with the rolling directions parallel to the rotor d-axis. This increases the d-axis inductance while reducing the q-axis inductance of the machine. An analytical model of the segmented-pole SynRM with CRGO laminations is presented in [25]. However, the research presented in [23, 25] lacks the study of torque performance of the SynRM rotor with CRGO laminations in operating regions other than the rated operation. In EV applications, the electric machine operates over a wide range of torque and speed that necessitates the study of its torque performance in the whole operating range. The torque performance of an electric machine is measured in terms of torque characteristics and torque-ripple.

The torque angle curve of a motor shows the variation of its output torque with the current angle (also called torque angle). It is used by machine designers for the validation of their analytic models and comparison among various designs [10, 82, 83]. Drive designers use the torque angle curves in implementation of the MTPA control for selection of the optimum current to minimize the copper loss. Due to square dependency of torque on stator current, MTPA control is more demanding in the SynRM compared to IPMSMs. Various methods to obtain and implementation of the MTPA control are presented in [84–88]. A simpler and accurate MTPA scheme is implemented using the MTPA trajectory obtained from the torque angle curve [88]. Various experimental methods to obtain the torque angle curves of a SynRM are discussed in [65, 89]. This chapter presents the evaluation of the MTPA trajectory of a segmented-pole SynRM using four experimental methods.

Besides the average torque produced due to the difference in reluctance in d-axis and q-axis, SynRMs produce pulsating torque due to non-sinusoidal Magneto-Motive Force (MMF) distribution and non-sinusoidal reluctance variation from the d-axis to q-axis. These parasitic torque components create torque-ripple in the SynRM which result in mechanical resonance, vibration, acoustic noise, and may even cause damage to the drive components [90, 91]. Many industrial applications require low torque-ripple and hence, minimizing this ripple is of a great importance. Approaches to minimize the torque-ripple in synchronous motors can be broadly classified into two classes [92, 93]. The first approach attempts to design the machine such that the machine geometry behaves more closely to its ideal magnetic characteristics, by using methods like shifting, shaping, skewing, addition of dummy slots, winding designs, asymmetric flux barrier design etc [92–96]. The second class of techniques modifies the current excitation by using active control schemes such that the pulsating torque components that would have been produced by sinusoidal currents are actively canceled. With the design approach of torque-ripple minimization, the focus is on the torque-ripple minimization at the rated condition [96–99]. However, in variable speed applications such as traction drives, the information about the torque-ripple at operating conditions other than the rated condition are also equally important. Below the base speed, it is possible to actively cancel the higher order torque harmonics. Nevertheless, there is a constraint of limited dc bus voltage that limits the possibility of active harmonic cancellation near and above the base speed. Thus, torque-ripple in the extended speed region can be more severe.

Various experimental methods to measure the torque-ripple in PMSMs and SynRMs exist in the literature [14, 95, 96, 99–102]. In [100], a static method is proposed to measure the cogging torque in PMSMs. It is measured by using a balanced beam and weight arrangement. There are experimental methods to measure the torque-ripple and cogging torque in the dynamic condition. They either require a higher bandwidth torque transducer [101], or a gear-box arrangement to reduce the speed [14, 96]. In [95, 99], the test motor is operated at a lower speed to measure the torque-ripple. In the existing methods, a gear-box arrangement and operation at a lower speed is required due to the limitations in the torque transducer bandwidth.

This chapter proposes an experimental method to obtain the static torque angle curves and torque-ripple of SynRMs in various operating conditions including the extended speed region. The proposed method is applied to two similarly sized SynRMs with the same geometry, however, one of the rotors is composed of four segments of CRGO laminations while the other is made of a regular CRNGO steel . The MTPA trajectories of the SynRMs under test are evaluated using torque angle curves obtained from four different experimental methods. The static torque waveforms of both the SynRMs are measured for the entire operating range to obtain the torque ripple of the motors for operating conditions including the extended speed region.

3.2 SynRMs under Test

Fig. 3.1 shows the geometry of the two SynRMs under test. Design details of this SynRM is presented in [103]. Table 3.1 presents the key specifications of the motors. The rated speed of the motors are 850 rpm and designed for 7.5 hp. Both the SynRMs consists of the same stator and winding layout. The geometry of both rotors are same with the same rotor and stator pitch angles. Fig. 3.1a presents the geometry of the transversely laminated anisotropic CRNGO rotor and stator. The CRNGO steel lamination possesses uniform magnetic properties. The stator has 36 slots with a stator slot pitch of 10°. The rotor consists of four barriers in each pole with a rotor slot pitch of 8.5°. In this design, neither the rotor nor the stator is skewed. The torque ripple originated due to the rotor and stator slots is minimized in this design by using a properly designed rotor slot pitch (α_r) against the selected stator slot pitch (α_s). The flux barriers are designed such that when the rotor rotates, all the rotor slots never face stator teeth or stator slots simultaneously. Fig. 3.1b shows the geometry of the segmented-pole SynRM using CRGO steel. It consists of a four pole rotor composed of four segments. Each rotor pole lamination is cut from CRGO steel sheet such that the direction of the q-axis is perpendicular to the rolling direction. The laminations are cut in such a way that an asymmetry is introduced in each lamination sheet while the barrier geometries are still symmetrical with respect to the q-axis. While assembling the rotor structure, every second layer is flipped over around the q-axis by 180° such that the q-axis of each layer is along the same

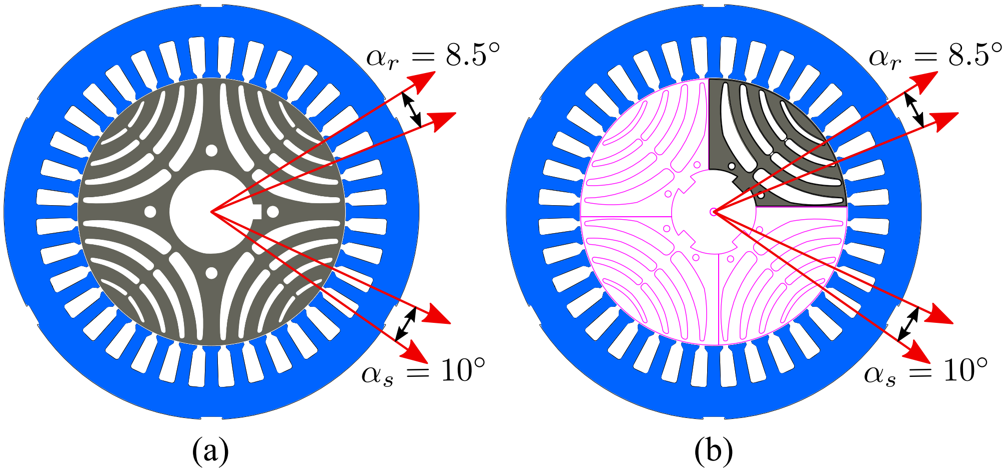

Fig. 3.1: Geometry of two different SynRMs under test. (a) Conventional SynRM rotor made of CRNGO laminations. (b) Segmented pole SynRM with CRGO laminations.

Table 3.1: Specifications of the SynRMs under test.

Machine type	3-phase Δ-connected
Rated power	7.5 hp
Rated current	20 A
Rated voltage	230 V
Base speed	850 rpm
Peak torque	60 Nm
Number of poles	4
Number of stator slots	36
Winding type	Fully pitched distributed
Air-gap length	0.4 mm
Stack length	200 mm
Stator outer diameter	208 mm
Rotor outer diameter	134.2 mm

axis [23]. For mechanical support, the lamination sheets have 3.2 mm guided pin holes, and M6 stud and nuts made of polyether ether ketone (PEEK) are used.

3.3 Torque Production in SynRMs

The torque generation in SynRM is due to the difference in the d- and q-axes permeance. The expressions for the torque and torque-ripple can be developed as follows:

$$
\begin{aligned}
\mathbf{V}_s &= R_s\mathbf{I}_s + \frac{d\boldsymbol{\lambda}_s}{dt} \\
\mathbf{V}_s &= [v_a\ v_b\ v_c]^\intercal \\
\mathbf{I}_s &= [i_a\ i_b\ i_c]^\intercal \\
\boldsymbol{\lambda}_s &= [\lambda_a\ \lambda_b\ \lambda_c]^\intercal \\
\boldsymbol{\lambda}_s &= \mathbf{L}_s \cdot \mathbf{I}_s
\end{aligned}
$$

where, $\mathbf{V}_s$ and $\mathbf{I}_s$ are the stator voltage and current vectors, $\boldsymbol{\lambda}_s$ is the stator flux linkage vector, R_s is the stator resistance and $\mathbf{L}_s$ is the inductance matrix. $\mathbf{L}_s$ can be decomposed into the sum of several matrices.

$$
\mathbf{L}_s = \begin{bmatrix} L_{aa} & L_{ab} & L_{ac} \\ L_{ba} & L_{bb} & L_{bc} \\ L_{ca} & L_{cb} & L_{cc} \end{bmatrix} \tag{3.1}
$$

$$
= \begin{bmatrix} L_{ls}+L_{ms} & -\frac{1}{2}L_{ms} & -\frac{1}{2}L_{ms} \\ -\frac{1}{2}L_{ms} & L_{ls}+L_{ms} & -\frac{1}{2}L_{ms} \\ -\frac{1}{2}L_{ms} & -\frac{1}{2}L_{ms} & L_{ls}+L_{ms} \end{bmatrix} +
$$

$$
L_k \begin{bmatrix} \cos 2k\theta_r & \cos k(2\theta_r - \phi) & \cos k(2\theta_r + \phi) \\ \cos k(2\theta_r - \phi) & \cos k(2\theta_r + \phi) & \cos 2k\theta_r \\ \cos k(2\theta_r + \phi) & \cos 2k\theta_r & \cos k(2\theta_r - \phi) \end{bmatrix} \tag{3.2}
$$

where, L_{ls} and L_{ms} are per phase leakage and magnetizing inductances respectively, k is the inductance harmonic order that accounts for the saliency, winding distribution and slot harmonics, L_k is the peak of the k^{th} inductance harmonic, θ_r is the rotor electrical position from phase A axis, and ϕ is $2\pi/3$. When k is unity, it accounts for saliency, and three times the L_1 gives the difference in d-axis inductance, L_d and q-axis inductance, L_q, which is responsible for an average torque during operation. The rest of the values of k results in pulsating torque which is responsible for the torque ripple in SynRM. The mathematical expression for the electromagnetic torque, T_{em}, the average torque, T_{avg}, and the torque ripple T_{ripple} are as follows.

$$
T_{em} = \frac{1}{2}\frac{\partial \mathbf{I}_s^\intercal \boldsymbol{\lambda}_s}{\partial \theta_m} = \frac{1}{2}\frac{\partial \mathbf{I}_s^\intercal L_s \mathbf{I}_s}{\partial \theta_m}
$$

$$= \frac{1}{2}\mathbf{I}_s^{\intercal}\frac{\partial L_s}{\partial \theta_m}\mathbf{I}_s = \frac{1}{2}\frac{P}{2}\mathbf{I}_s^{\intercal}\frac{\partial L_s}{\partial \theta_r}\mathbf{I}_s \tag{3.3}$$

$$T_{avg} = \frac{1}{2\pi}\int_0^{2\pi}\frac{1}{2}\frac{P}{2}\mathbf{I}_s^{\intercal}\frac{\partial L_s}{\partial \theta_r}\mathbf{I}_s d\theta_r \tag{3.4}$$

$$T_{ripple} = \frac{\Delta T_{em}}{T_{avg}} \tag{3.5}$$

where, θ_m is the rotor mechanical position and P is the number of poles. Computation of the instantaneous torque in the SynRM requires the rate at which the inductance matrix varies with the rotor position. In terms of dq inductances, the instantaneous torque as a function of L_d and L_q can be expressed as shown in (3.6).

$$T_{em} = \frac{3}{2}\frac{P}{2}\{L_d(i_d, i_q, \theta_r) - L_q(i_d, i_q, \theta_r)\}\frac{i_s^2}{2}\sin(2\delta) \tag{3.6}$$

where, i_d and i_q are the d- and q-axes currents, the components of $\mathbf{I}_s$, i_s is the instantaneous magnitude of $\mathbf{I}_s$, and δ is the torque angle (also called the current angle). In an ideal case, the phase inductances varies sinusoidally with the rotor position and the dq inductances remain constant. However, due to the effects of stator slots, rotor flux barriers, and saturation effects, these inductances consist of harmonics. These harmonics create torque-ripple when they interact with the stator MMF. In addition, the flux density distribution of the stator current consists of harmonics due to variation in permeance with respect to the rotor position. These flux density harmonics also contribute to the torque-ripple. Taking into account the rotor and stator geometry, the development of an analytic expression for the actual torque waveform is challenging. However, with some approximations, it is possible to obtain the torque waveform of the SynRM [82]. A more accurate torque waveform used by many researchers is obtained using the finite element analysis (FEA) of the machine [95–99]. The relation (3.4) also depicts that the average torque depends on the current magnitude and angle. Based on (3.6), the average electromagnetic torque is proportional to the square of i_s. The variation of the torque with δ is called the torque angle curve. Machine designers use them for the validation of their analytic models and comparison among various designs. Drive designers use the torque angle curves in implementation of the MTPA control for selection of the optimum current to minimize the copper loss.

3.4 Torque Angle Curve Measurement

Fig. 3.2 shows the vector diagram of a SynRM. The current vector is leading the d-axis of the rotor by an angle of δ. When its value is such that the stator current, i_s lies either in the first quadrant or the third quadrant, the motor produces positive torque, else the generated torque is negative. The

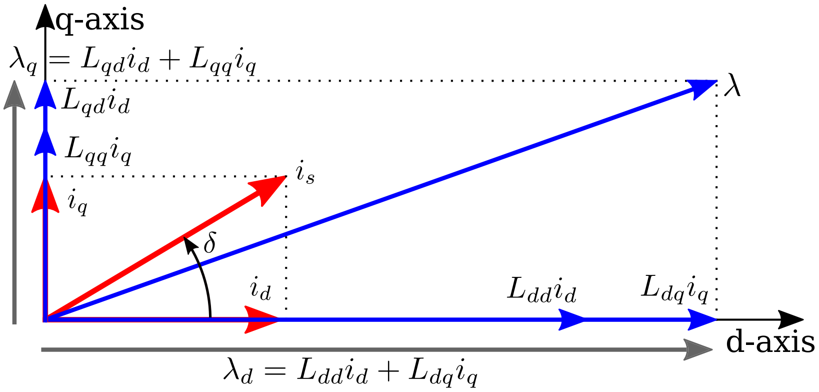

Fig. 3.2: Vector diagram of SynRM showing currents and fluxes.

torque expression in 3.6 depicts that the SynRM torque depends non-linearly with both the stator current and torque angle. Since the copper loss in the stator is proportional to the square of the stator current, MTPA operation of the SynRM is necessary to minimize the copper losses.

A feasible solution for the MTPA trajectory can be obtained using numerical solutions of Finite Element Method (FEM) model. The success of such a model in generating the MTPA trajectory depends on accurate modeling of several physical elements. When the motor design data is not available, experiment on the physical machine is the only option. In the literature, there are three experimental methods to obtain the torque angle curves of the SynRM [65, 88, 89]. One of them is performed with the motor running at the rated speed. The remaining two methods are performed under locked rotor condition, and they can be combined to obtain a fourth method to measure the torque angle curves as listed below.

- Steady state load test at rated speed
- Locked Rotor Test (LRT) with a fixed current vector while varying the rotor position
- LRT with a fixed rotor position while varying the current vector
- LRT varying the rotor position and the current vector

3.4.1 Steady State Load Test

In order to measure the steady state torque angle curves of the SynRMs, the test motors are operated at the rated speed with suitable load. Fig. 3.3 shows the schematic of the complete test system. The test motor is coupled to a dc dynamometer with a torque transducer (MCRT® 2903T) in between. The power flow in the dc dynamometer is controlled using a four quadrant dc drive (ABB DCS800). A standard two level voltage source inverter (VSI) from Semikron (SEMITEACH

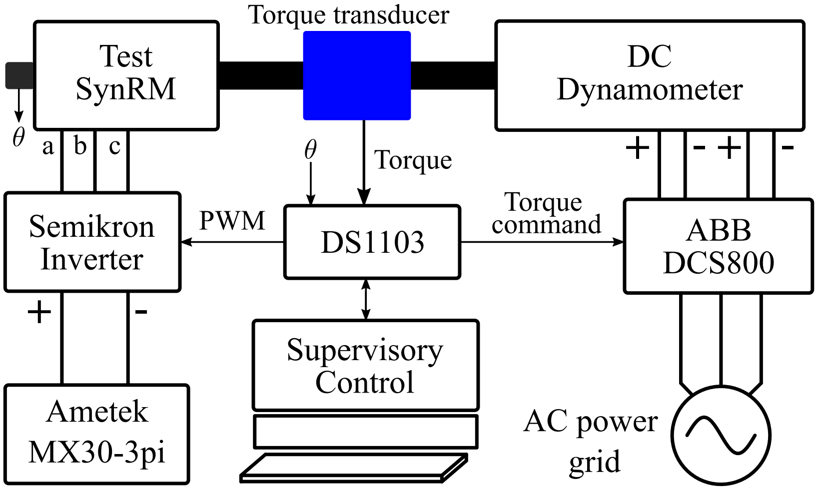

Fig. 3.3: Schematic of the test bench to measure torque angle curves.

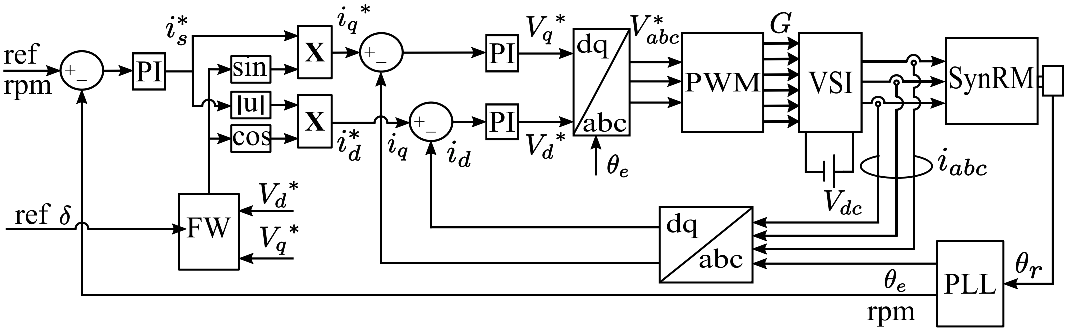

Fig. 3.4: Schematic of the drive control strategy in speed control mode.

B6U+E1CIF+B6CI) is used to control the power flow to the test SynRM. The dc link of the VSI is supplied directly from a programmable power supply (Ametek MX30-3Pi). A dSPACE (ds1103) control and prototyping system is used to command and control both the test and load motors. The load is operated in torque control mode and the test SynRM is operated in speed control mode.

Fig. 3.4 shows the schematic of the drive control strategy. Inputs to the controller are the reference speed and the reference torque angle, δ. The speed error is passed through the controller to generate the reference stator current, i_s^*. The δ is given to the controller explicitly by the operator. From the reference i_s^* and δ, i_d^* and i_q^* are computed. The errors in i_d and i_q are passed through PI controllers to generate V_d^* and V_q^*. V_d^* and V_q^* are transformed to V_{abc}^* which is used by the Pulse Width Modulation (PWM) generator block to generate the PWM signals. The three phase currents are measured and transformed to dq currents. The actual torque angle (or current angle) is calculated from the measured dq currents. In steady state, the reference δ is equal to the measured torque angle.

All the measurements are taken at steady state. Initially, the machine is run at the rated speed without any load torque. The torque angle is set to a low value ($10^\circ - 20^\circ$). The load torque in DCS800 is increased gradually so that the stator current reaches the desired magnitude. In steady state, the shaft speed, torque angle, current magnitude and torque measured by the transducers are recorded. The reference torque angle is increased by few degrees (3° in this test). The load torque on the DC drive is increased such that the measured current magnitude is the same as the previous test point. All the measured variables are recorded at steady state, and the process is repeated until the δ is close to 90°. The process is repeated for different current magnitudes.

3.4.2 Locked Rotor Tests (LRTs)

In locked rotor tests, all the measurements are taken at static conditions with the rotor locked at a fixed position. Depending on how the current angle δ is varied, torque angle curves are obtained using three different methods.

LRT Varying the Rotor Position

In this method, the torque angle curves are obtained by varying the rotor position keeping the current vector fixed in space. The shaft in between the torque transducer and dynamometer is locked using a mechanical clamp, and a DC source is normally used to supply a current vector which is fixed in space. For the experimental tests in this chapter, a three phase VSI is used to control the three phase current such that the current vector is fixed in space (along phase A-axis). First of all, the rotor d-axis is aligned along the stator phase ‘A’ axis. In such a case, the angular position of the shaft from the initial position is the torque angle. The shaft is locked on the dynamometer side using a clamp as shown in Fig. 3.5. In order to mitigate the torsional energy storage in the coupling, a rigid coupling is used between the test motor and the torque transducer. The test bench height is adjusted such that the alignment error is minimal. Thus, the force due to the machine misalignment in the direction perpendicular to the axis of measurement is negligible. Keeping the current vector along the same direction, the output torque of the SynRM is recorded for rotor positions with the torque angles ranging from zero degrees to 90° for various current magnitudes at locked rotor conditions, to obtain the torque angle curves.

LRT Varying the Current Vector

In this method, the torque angle curves are obtained at a fixed rotor position while varying the current vector orientation. Initially, the rotor d-axis is aligned along the stator phase ‘A’ axis. The rotor is locked, and rotor position read by the encoder is fed to the controller. Fig. 3.6 shows the

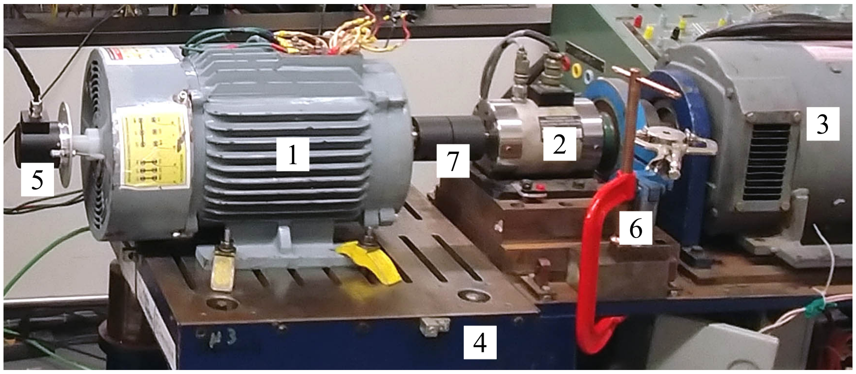

Fig. 3.5: Physical test bench showing 1. SynRM under test. Dynamometer base. 2. Torque transducer. 3. DC dynamometer. 4. Test bench 5. Position encoder. 6. Mechanical clamp. 7. Rigid coupling

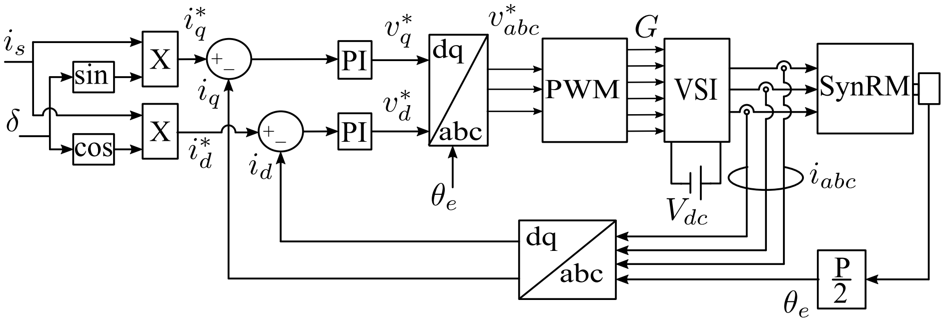

Fig. 3.6: Schematic diagram of the control strategy to measure the torque-angle curves and torque waveforms.

schematic diagram of the control strategy used to obtain the torque angle curve using LRT while varying the current vector. The input to the controller are the current magnitude, i_s and the torque angle, δ. Three phase currents are measured and fed to the controller. The controller generates the PWM signals such that the three phase currents in the machine transforms to a current vector given as the reference. The output torque is measured and recorded for each current magnitude, i_s supplied to the SynRM for values of δ ranging from zero to 90 degrees keeping the rotor position constant.

LRT Averaging over the Rotor Periphery

This method is a combination of the two previously mentioned methods. In this method, an average of the torque readings at different rotor positions for the same torque angle is taken to obtain the torque angle curves. Initially the rotor d-axis is aligned with the stator phase 'A' axis. The torque angle curves for different current magnitudes are obtained at that rotor position by varying the current vector. Next, the rotor position is advanced and locked, and the torque angle curves for the same current levels as before are obtained by varying the current vector. The process is repeated for the rotor positions extending to a full electrical cycle. Finally, an average of the torques at different rotor positions for each current magnitude and torque angle is obtained. Thus, this method considers both the spatial variation due to slotting effects and current vector orientation. If the symmetry in the geometry is known, the range of rotor positions for the measurement can be reduced to lower the measurement duration.

3.5 Maximum Torque Per Ampere Trajectory

Figs. 3.7 and 3.8 present the plots for the experimentally obtained torque angle curves and MTPA trajectories of CRNGO and segmented pole CRGO SynRMs respectively using the experimental methods described in the previous section. Figs. 3.7a and 3.8a demonstrate that the static torque angle curves obtained using LRT while varying the rotor position are not smooth, and they have peaks due to the effects of stator slots. Additionally, the peak or maximum torque at all magnitudes of currents occur at the same torque angle. Thus, the MTPA trajectories are vertical. In other words, the MTPA torque angle is a constant. Figs. 3.7b and 3.8b present the torque angle curves obtained by varying the current vector orientation when the rotor position is such that the direct axis of the rotor is aligned with the stator phase A-axis. The MTPA trajectories obtained using this method are skewed towards higher torque angles for higher currents.

Figs. 3.7c and 3.8c present the averaged torque angle curves over the rotor periphery for the test motors obtained by varying both the rotor position and current vector orientation. The MTPA trajectories obtained using this method are closer to the ones obtained using the steady state load tests. Figs. 3.7d and 3.8d show the torque angle curves and MTPA trajectories for the SynRMs obtained using the steady state load test. These are the actual curves as they are obtained by operating the SynRMs at the real operating conditions. Due to the limitations in the capacity of the dc drive, the stator current in the SynRMs are limited to $8A$ in this test. However, it is still enough to show that the actual MTPA trajectories are close to the MTPA trajectories obtained using the locked rotor test while varying both the current vector orientation and the rotor position. The reason for the deviation in static tests and steady state load tests is that the current supplied to the stator in the latter has to overcome the frictional and windage torque, and it has to supply additional losses (core losses, stray load losses).

The experimental results suggest that the static torque angle curves obtained by LRT while varying the rotor position does not produce a true MTPA trajectory. When torque angle curves are obtained by LRT while varying the current vector, the MTPA trajectories obtained are somewhat similar to the actual trajectories. A fairly accurate estimate of MTPA trajectory can be obtained

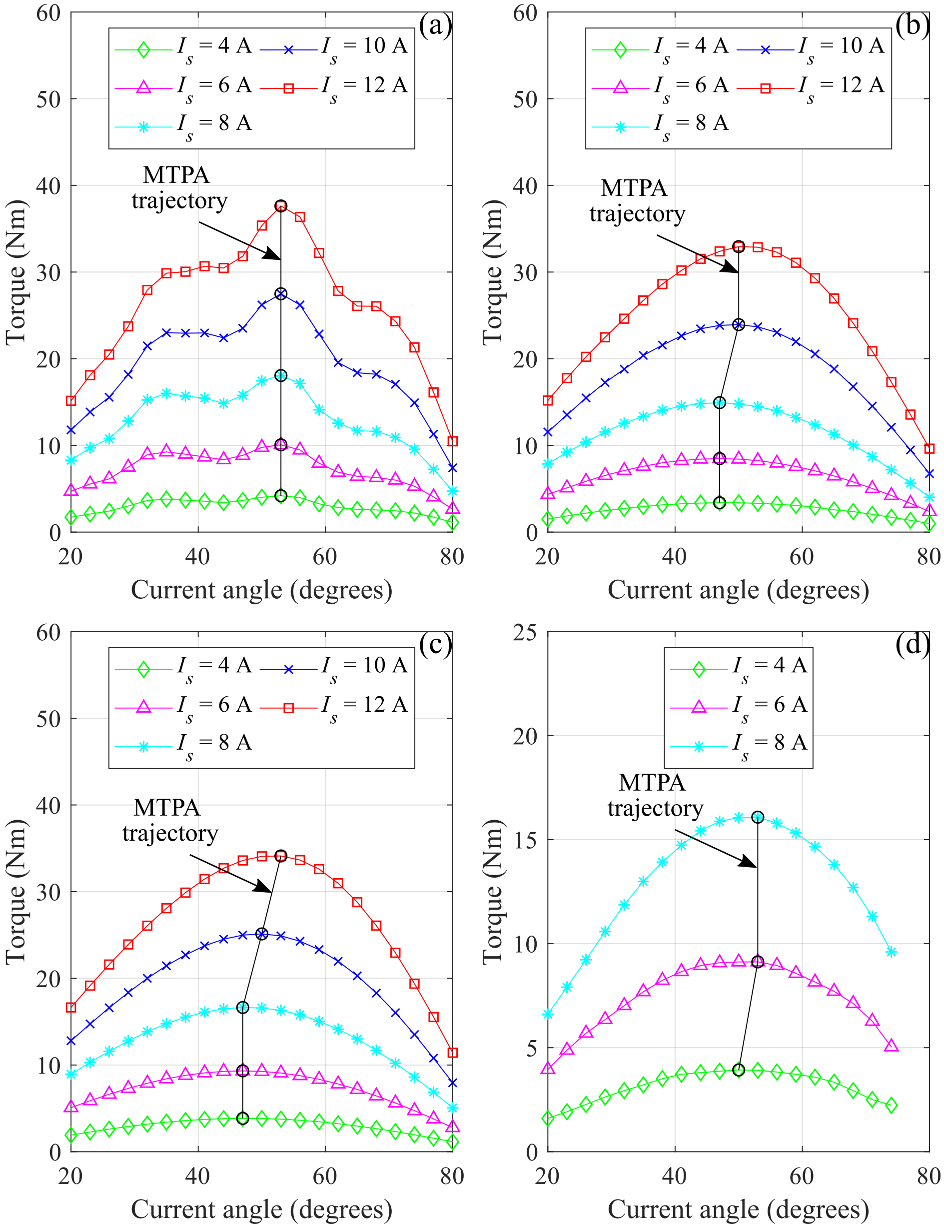

Fig. 3.7: Experimentally obtained torque angle curves and MTPA trajectories for the SynRM with CRNGO rotor. (a) Current vector kept fixed, rotor position varied. (b) Rotor position kept fixed, current vector varied. (c) Averaged torque angle curves for rotor positions extending the full electrical cycle. (d) Averaged torque angle curve when the machine is rotating at the rated speed.

from static torque angle curves measured using LRT while varying both the current vector and rotor position. Since the operation of a drive and loading it with a fine control over load torque is expensive, static tests while varying the current vector and the rotor position could be less expensive and acceptable solution to obtain the MTPA trajectory of SynRMs.

While comparing the torque angle curves in Figs. 3.7c and 3.8c, a segmented pole CRGO

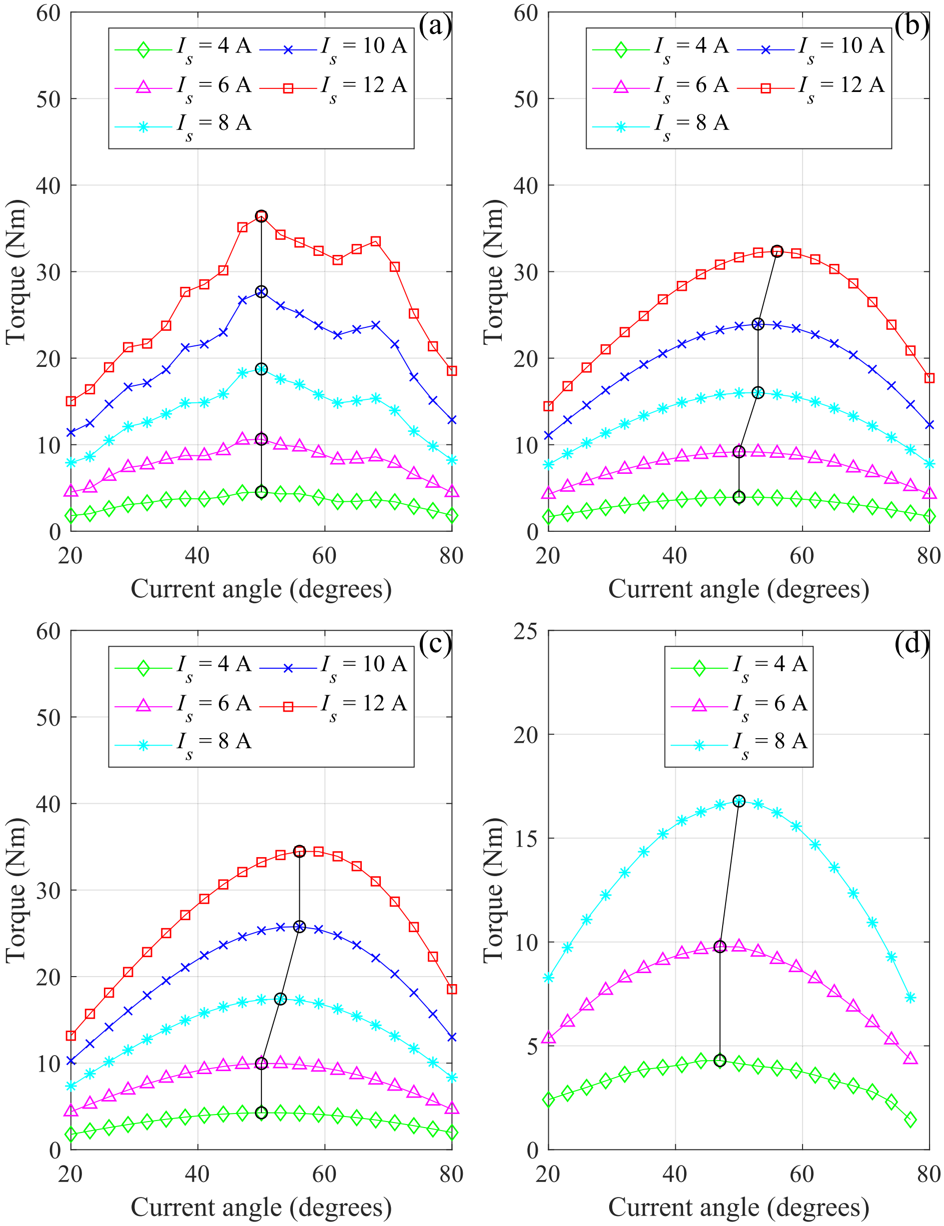

Fig. 3.8: Experimentally obtained torque angle curves and MTPA trajectories for the SynRM with CRGO rotor. (a) Current vector kept fixed, rotor position varied. (b) Rotor position kept fixed, current vector varied. (c) Averaged torque angle curves for rotor positions extending the full electrical cycle. (d) Averaged torque angle curve when the machine is rotating at the rated speed.

SynRM produces a higher average peak torque for lower current magnitudes. However, for higher currents (12 A), the torque increment in the CRGO SynRM is very small. Nevertheless, the torque angles for MTPA operation in CRGO SynRM are larger compared to CRNGO SynRM. It means that the magnetizing current in CRGO SynRM is lower, which eventually increases the power factor.

3.6 Torque-Ripple Evaluation

Torque-ripple measurement in a SynRM is a challenging task. The existing test methods to measure the torque-ripple basically operate the test machine either at lower speeds [95, 99] or at the rated speed with a gear arrangement [14, 96] with either an active or passive load being applied to the shaft. In [101], a detailed analysis of the system requirements to measure the torque-ripple in PMSM is presented. The authors selected a piezoelectric torque transducer to achieve a measurement bandwidth of 213 Hz. With such a high bandwidth, the authors proposed an accurate torque-ripple measurement without using a gear system. Since the torque-ripple is at higher frequency than the fundamental, an accurate measurement of the torque-ripple in the extended speed region would require a higher bandwidth torque transducer than available.

Nevertheless, when the torque angle curves are obtained using LRT while varying the rotor position and the current vector orientation, torque information at every rotor position for different torque angles and current magnitudes are available. This data can be rearranged to generate the torque waveforms at different current magnitudes and angles, including the ones for higher values of δ. SynRMs are operated at higher values of δ to weaken the flux in extended speed operation. Thus, the LRT while varying the rotor position and current vector orientation can be used to generate the torque waveform for any operating point. From the torque waveform, the percentage torque-ripple is obtained using (3.5).

3.6.1 Experimental Results

Fig. 3.9 presents the experimentally obtained torque waveforms and torque ripple of the CRNGO SynRM. The torque-angle curves using the LRT while varying the current vector orientation obtained at rotor positions for every 3° electrical is used to generate the torque waveforms. Fig. 3.9a presents the torque waveforms for three different values of δ for $I_s = 12A$. It shows that the peak to peak torque-ripple and the average torque depend on δ. Similar waveforms are obtained for various current magnitudes and angles. Fig. 3.9b presents the torque ripple magnitude variation with the current angle for three different magnitudes of current. It shows that the torque ripple magnitude varies with both current magnitude and angle. It increases with an increase in the current magnitude. Fig. 3.9c shows the variation of percentage torque-ripple with the current angle at three different current magnitudes. It shows that the percentage torque ripple for CRNGO SynRM is higher for lower current magnitudes. Moreover, the percentage torque ripple is higher for higher values of δ. The torque ripple in the rated operating region is lower. The SynRM is operated at higher torque angles during field weakening operation, where the percentage torque ripple is highest. Although the percentage torque ripple is high for lower values of δ, the SynRM is not operated in this region

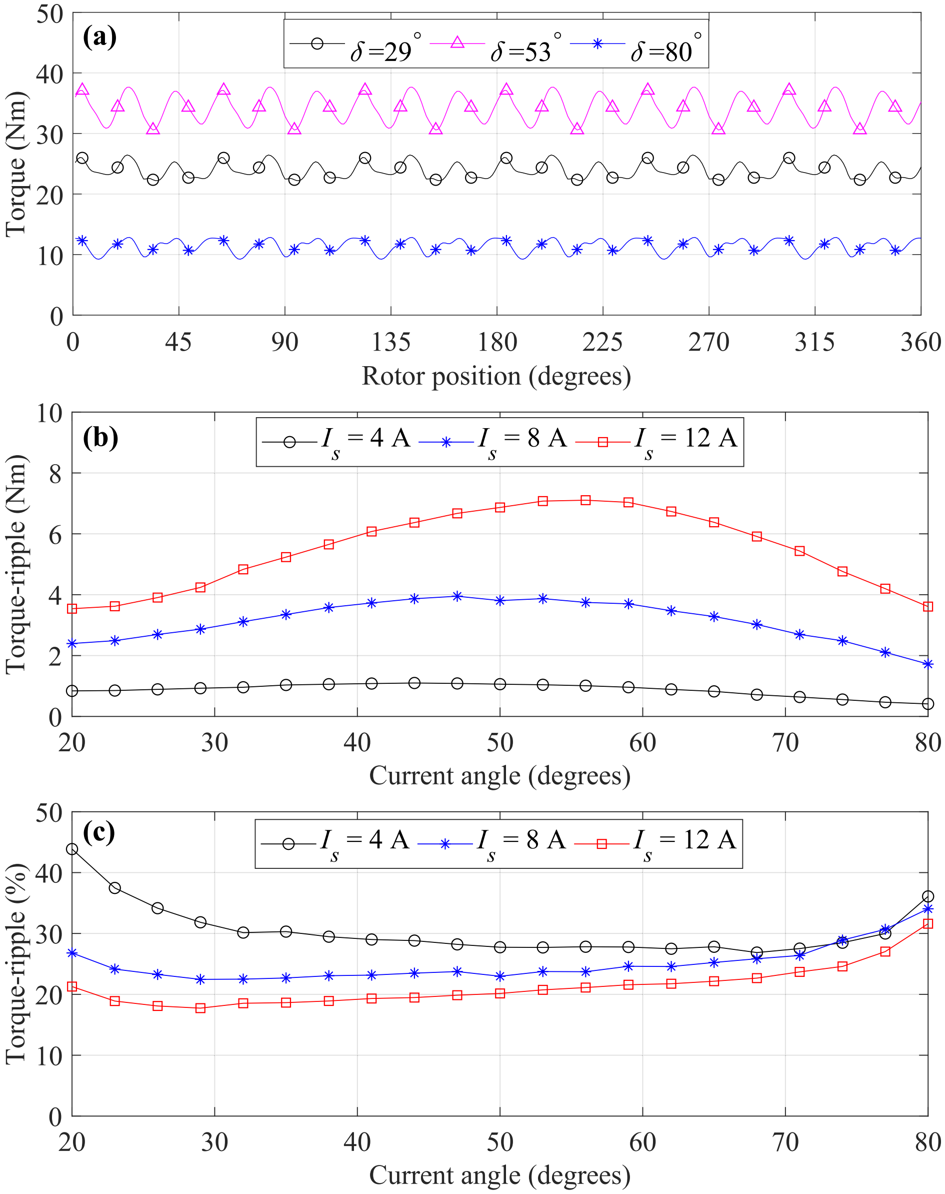

Fig. 3.9: Experimental results for the CRNGO SynRM. (a) Torque waveforms at I_s =12 A for three different current angles. (b) Torque ripple magnitude. (c) Percentage torque-ripple.

due to high magnetizing current.

Fig. 3.10 presents the experimental results for the segmented pole CRGO SynRM. The torque waveforms at $I_s = 12A$ for three different values of δ are shown in Fig. 3.9a. Figs. 3.9b and 3.9c present the torque ripple magnitude and percentage torque-ripple variation with current angles for three magnitudes of currents. Similar to the CRNGO SynRM, the torque ripple magnitude varies with current angle and magnitude. For operation near the MTPA operating points, as opposed to the CRNGO SynRM, the percentage torque ripple in the segmented pole SynRM is almost constant. However, in the field weakening operation for higher values of δ, it is high at lower current

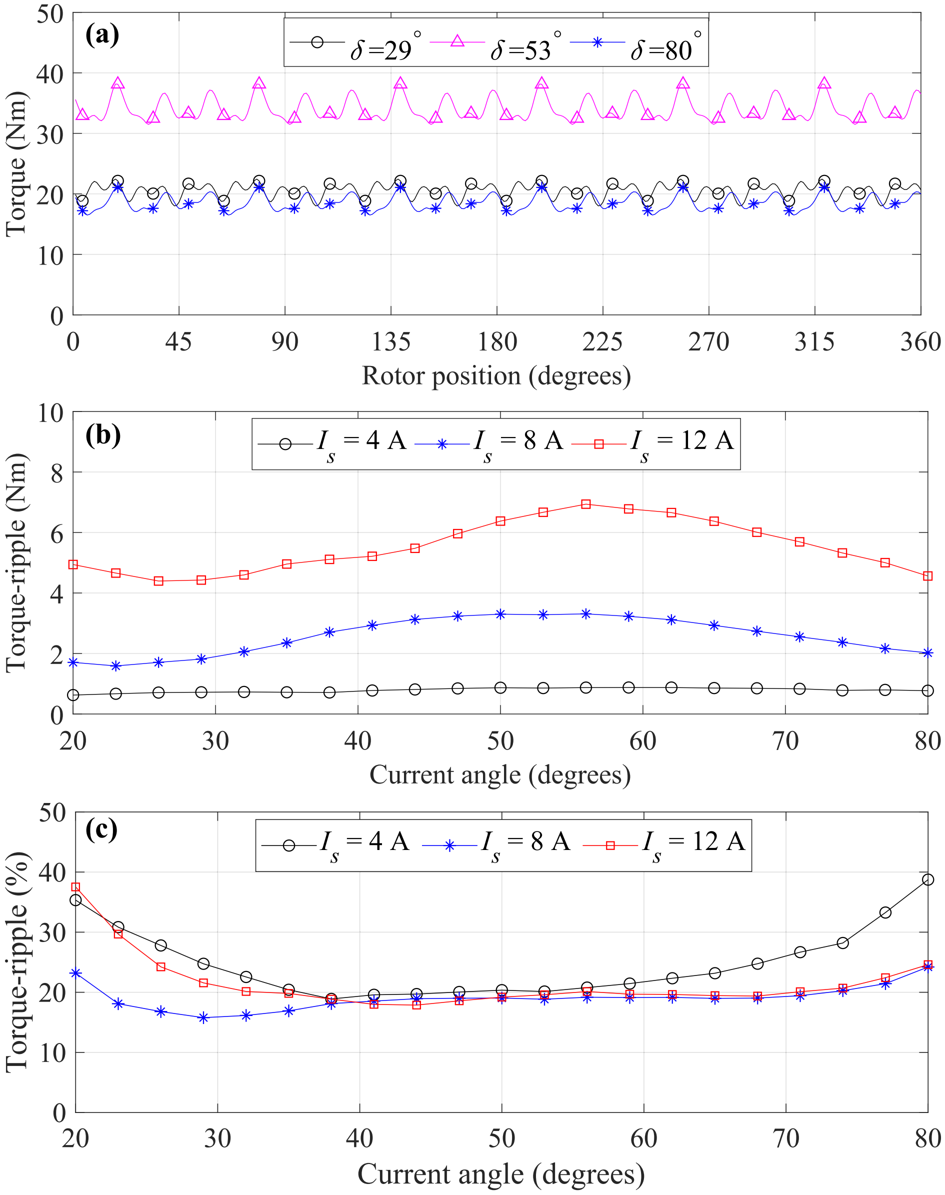

Fig. 3.10: Experimental results for the CRGO SynRM. (a) Torque waveforms at I_s =12 A for three different current angles. (b) Torque ripple magnitude. (c) Percentage torque-ripple.

magnitude. For higher current magnitudes, the percentage torque ripple is almost constant, but higher compared to the operation at lower values of δ.

Comparing the torque waveforms for the CRGO and CRNGO SynRMs, it is seen that the CRGO SynRM has a higher average torque and lower torque ripple in the MTPA operating region. In the field weakening operation region, while the CRNGO SynRM has almost constant percentage torque ripple, the CRGO SynRM percentage torque ripple is higher at lower current magnitudes and lower at higher current magnitudes.

3.7 Torque-Speed Characteristics

For operating speeds lower than the base speed, the inverter dc voltage is not utilized fully. Due to the extra voltage margin, the active harmonic control algorithms can be implemented to actively cancel the torque harmonics. However, in the extended speed region, the dc bus voltage is utilized fully in the torque-speed envelope boundary. Consequently, active cancellation of the torque harmonics becomes challenging. As presented in Figs. 3.9 and 3.10, the CRNGO SynRM has higher percentage torque ripple at higher values of δ, which will affect the SynRM operation in the extended speed region.

Fig. 3.11 depicts the experimentally obtained torque-speed and power-speed curves of both CRNGO and CRGO SynRMs for $I_s = 8A$. The same experimental setup with schematics shown in Fig. 3.3 is used to measure these curves. The SynRMs are operated in speed control mode and the dc dynamometer is operated in torque controlled mode. For the same current magnitude, it is seen that the CRGO SynRM produces slightly higher (3%) torque and power. Moreover, when operated with the same controller as a speed controlled drive, the CRGO SynRM has a higher speed range.

In order to assess the power factor and efficiency of the two SynRMs, the power factor and efficiency of the motors are also measured along with the torque and speed. A Yokogawa WT3000 power analyzer is used to measure the three phase power input to the SynRMs and the mechanical power output in the shaft. Below the base speed, the SynRMs are operated in MTPA mode. Fig. 3.12 compares the experimentally measured power factor and efficiency of the SynRMs. As predicted by the MTPA trajectories in Figs. 3.9c and 3.10c, the CRGO SynRM has higher power factor in all the operating regions compared to the CRNGO SynRM. This is due to higher d-axis permeability in the CRGO SynRM which decreases the magnetizing current. Although a lower power factor increases the losses causing reduction in the efficiency, the efficiency of both the SynRMs are almost the same except at highest speeds of operation.

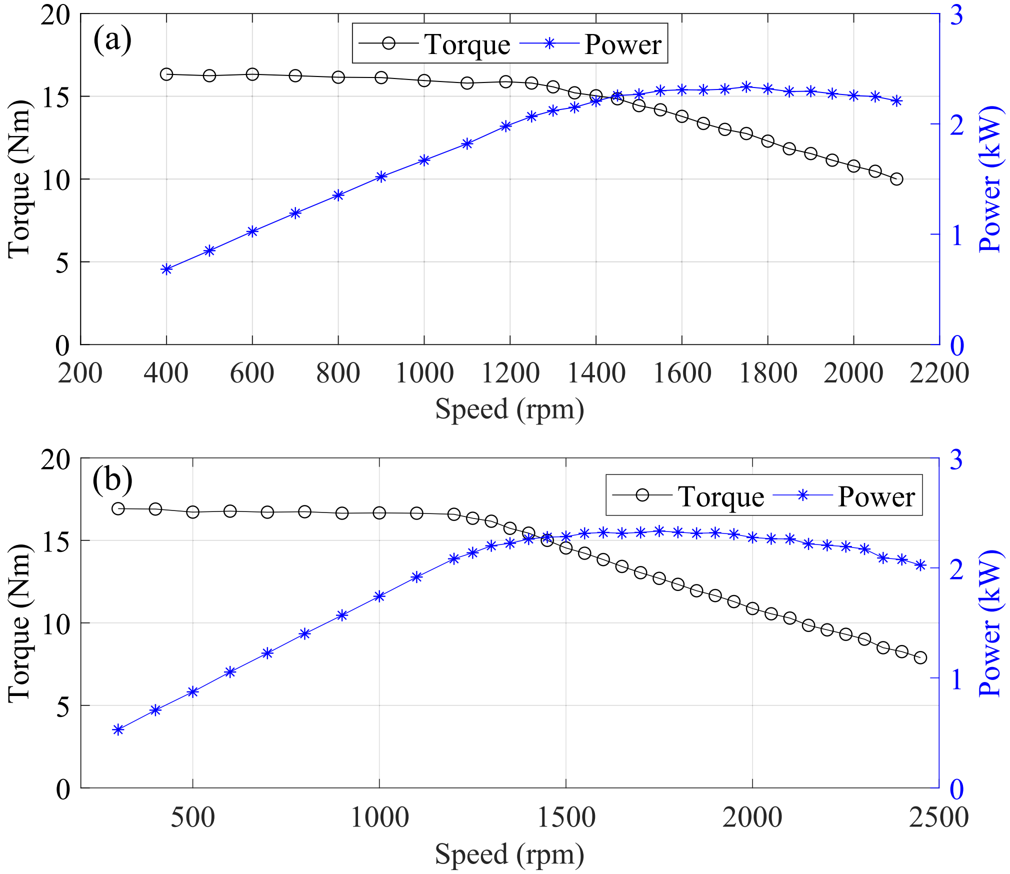

Fig. 3.11: Experimental obtained torque-speed and power-speed curves of at I_s =8A. (a) CRNGO SynRM. (b) Segmented pole CRGO SynRM.

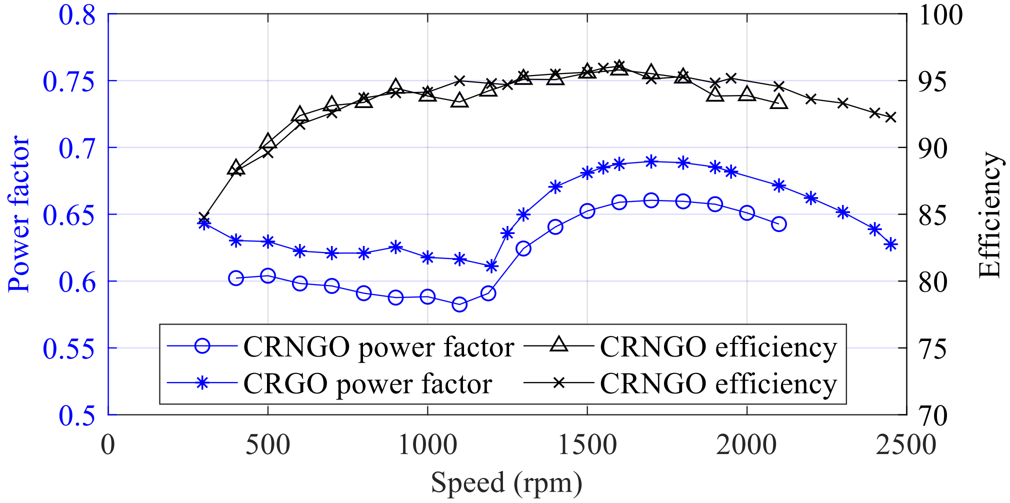

Fig. 3.12: Comparison of the power factor and efficiency of the CRNGO and CRGO SynRMs.

3.8 Summary

SynRMs are one of the alternative machines for transportation electrification. This chapter presented an experimental study of the torque performance of a segmented-pole SynRM with CRGO laminations. The torque angle curves of the CRGO and CRNGO SynRMs are measured using steady state load tests and LRTs. A combination of LRTs while varying the rotor position and varying the current vector orientation is proposed to measure the average torque angle curve and torque ripple in the SynRMs. Although the steady state load test gives the actual torque angle curves and MTPA characteristics of the SynRM, it requires a fully operational dynamometer test bench. However, the LRT with varying both current vector and rotor position can also give highly accurate torque angle curves and MTPA characteristics. In addition, the torque angle curves measured using such a method contains torque ripple information of the tested motor. Thus, the same experimental data can provide MTPA characteristics and torque ripple.

A comparison of the torque angle curves of the CRNGO and CRGO SynRMs shows that the MTPA operation occurs in the CRGO SynRM at higher values of current angle. Consequently, it shows a higher power factor due to reduced magnetizing current. While comparing the percentage torque ripple, the CRGO SynRM shows lower torque ripple in all operating regions. Due to higher permeability in the d-axis in the CRGO SynRM, the saliency ratio is improved, which results in an improvement in torque per ampere and power factor.

Based on the work presented in this chapter, the following research papers are published [68, 104].

- R. Thike and P. Pillay, ”Experimental Study of Torque-Ripple and its Effect on the Flux Weakening Range of Synchronous Reluctance Machines,” 2019 IEEE International Electric Machines & Drives Conference (IEMDC), San Diego, CA, USA, 2019, pp. 1479-1484, doi: 10.1109/IEMDC.2019.8785090

- R. Thike and P. Pillay, ”Experimental Investigation of MTPA Trajectory of Synchronous Reluctance Machine,” 2018 IEEE International Conference on Power Electronics, Drives and Energy Systems (PEDES), Chennai, India, 2018, pp. 1-6, doi: 10.1109/PEDES.2018.8707820.

Chapter 4

Modeling of a Shifted Interior Permanent Magnet Machine

As discussed in section 1.1, electric motors for traction applications require high torque and power density, and wide speed range with high efficiency [5]. The PMSMs have higher efficiency and higher torque density compared to IMs and SynRMs. Thus, they are widely used in traction applications. However, due to the increasing demand on rare-earth magnets and the high fluctuation in its price, the current trend in research focuses on the design of alternative electric machines technology that either do not use the rare-earth magnets, or reduce the amount required.

Ferrite based PMSMs, [105–107] and AlNiCo based PMSMs [47, 65, 108] are some alternative technologies that do not use rare earth magnets. However, Ferrite magnet based PMSMs have low torque density, and control techniques for the AlNiCo based variable flux machines are still ongoing research [109], making these technologies not ready for transportation applications. Apart from the use of different magnets, there is also an intensive research going on to minimize the amount of rare-earth magnets usage in interior permanent magnet synchronous machines (IPMSMs). These works focus on increasing the torque density of the IPMSMs by design optimization based methods [110]. In the literature, extensive research on PMSMs designs exist that provide higher torque density and superior field weakening performance. However, the magnetic torque and the reluctance torque in these machines have their maximum value at different torque-angles. Consequently, the resultant torque is less than the algebraic sum of the torque components.

4.1 Background

A new class of IPMSM having asymmetrical rotor structure called shifted IPMSM aligns the magnetic and reluctance torque to improve the torque density. Recently, in order to improve the torque density of the PM machines, numerous research on alternate designs for PM machines with asymmetrical rotor structures, [26–38, 40, 41] have been conducted. The asymmetry is either created by using a hybrid rotor structure, [27–31] or by shifting the magnetic axis and the use of flux barriers [32–37]. In [26], an asymmetrical rotor is designed for easy assembly and repair of field windings in synchronous machines. The hybrid rotor structure consists of either two different rotors sandwiched together with some optimal assembly angle [28], or a single rotor with a complex arrangement of magnet and flux barriers [29, 30]. It is shown that the hybrid rotor structure has an improved torque characteristic. In [31], a hybrid of a surface-inset and interior PMSM topology is presented. The hybrid rotor PM motor shows an improved torque capability.

The asymmetrical rotor structures that use shifting of the magnetic axis and the reluctance axis by the use of flux barriers are simpler and easier to analyze. The objective of such designs is to align the magnet and reluctance torques to maximize the output torque. An asymmetry in the rotor design that allows the reluctance and magnetic torques to reach a maximum value at the same torque-angle is developed in [32, 33] for a V-type interior PMSM. The asymmetry is created in these designs by adoption of assisted barriers employed to allow the reluctance and magnetic torques to reach a maximum value near or at the same current phase angle. A similar approach for a surface-inset PMSM is adopted to improve the torque and efficiency in [34, 35]. In [39], a novel ferrite assisted synchronous reluctance machine is proposed that utilizes both reluctance and PM torque components fully. An interior PMSM design with an additional barrier to align the magnet torque and the reluctance torque is presented in [36]. It showed that the same output torque of a conventional IPMSM can be achieved by shifting one of the torque components with a lower permanent magnet volume. In [37], FEA analysis of an aligned axis IPMSM considering saturation is presented. However, they presented torque characteristics solely based on FEA, and they lack the actual torque based on experiment to prove the underlying concept.

While researchers focused on design improvements to improve the torque performance or reduce the magnet volume by utilizing shifting technique [26–37], a mathematical model suitable for the analysis of such designs is lacking. A mathematical model of a machine allows a better understanding of the machine and it gives insight on the effect of each variable on the machine dynamics. Drive engineers use it for the design and operation of the drive. The torque characteristics of a shifted IPMSM is different from conventional IPMSM designs. The existing mathematical models used for the conventional IPMSM must be modified to understand the shifted IPMSM behavior. In [40], a theoretical analysis of synchronous machines with displaced reluctance axis for different values of the shift angle between the reluctance and magnet axes is presented. An equivalent magnetic circuit model is presented in [111], and utilized to separate the PM and reluctance torques for a hybrid rotor PM motor. The effects of positioning of permanent magnet axis relative to reluctance axis in PMSMs is presented in [41]. The authors developed the mathematical model of the surface inset PMSM by transformation of the machine equations in one reference frame to another reference frame with different orientation, and came up with three torque components viz; magnet torque, saliency (reluctance) torque and asymmetry torque. Finally, the authors concluded with the existence of an additional torque component in an asymmetric PMSM. In [30], a similar approach is used to describe the torque components in a hybrid rotor PMSM. The authors defined two more additional torque components viz; cross magnet torque and cross reluctance torque. However, these torque components vanish depending on the reference frame axis orientation. In both [41] and [30], a comprehensive interpretation of the developed models are lacking.

This chapter presents the development of a mathematical model of a novel shifted IPMSM with reference to the design presented in [36]. This design has higher torque per magnet volume compared to the conventional designs, and thus the cost associated with the magnet can be reduced in vehicle applications. In order to derive its mathematical model, a simplified rotor structure with sinusoidal air-gap variation is assumed. In the development of the model, the effects of harmonics due to stator slots, non-sinusoidal air-gap distribution and non-sinusoidal winding distribution are not considered. The developed model is useful in the design of such machines and its drives. In order to validate the developed model, a prototype of the motor is built for experimental validation. Compared to the mathematical model presented in [41] and [30], the mathematical model of the shifted IPMSM developed in this thesis uses the principles in magnetic circuit analysis, and presents two different forms of the mathematical model depending on the location of reference frame axis. Due to the comprehensive development of the model, the developed model presents a better understanding of the torque components in the shifted IPMSM. Additionally, this thesis presents a method based on back EMF measurement to locate the rotor d-axis. Based on the experiments, the conventional method to find the rotor d-axis in PMSMs does not find the rotor d-axis position in the shifted IPMSM. This thesis also presents an automated current control method to obtain the machine parameters in the developed model. Unlike [16], this thesis measures the position dependent inductances in the stationary reference frame. The developed model is validated by comparing the experimental torque-angle curves and torque-speed curves with the ones generated from the model.

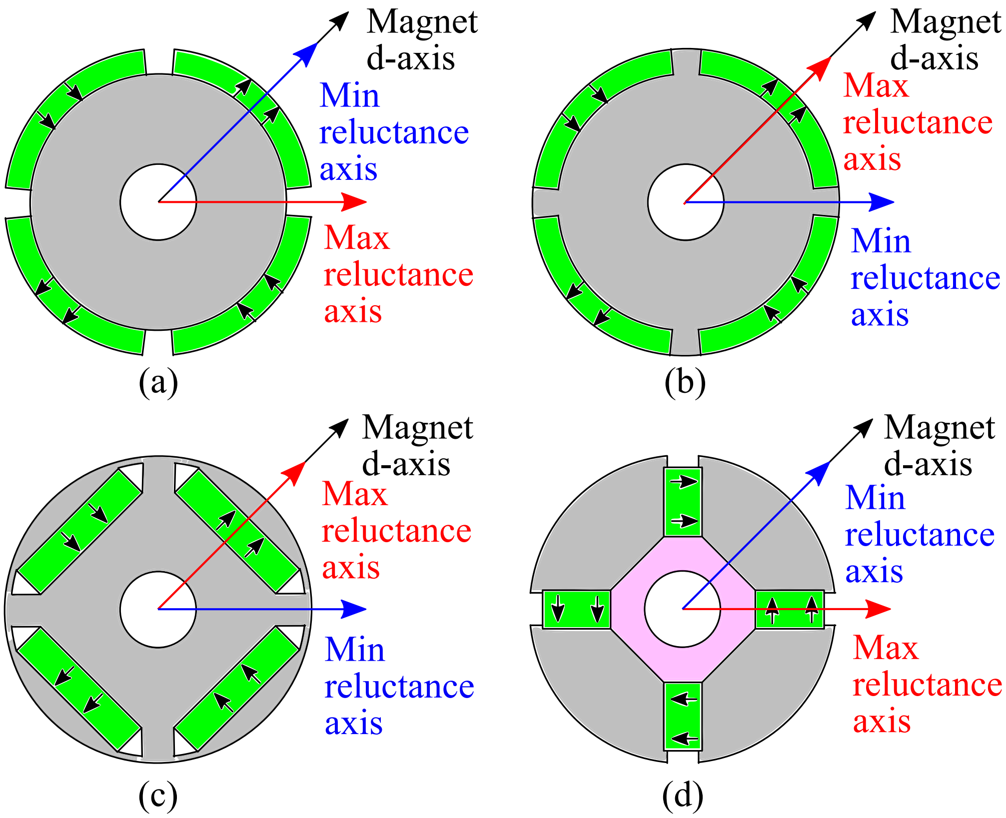

Fig. 4.1: Different PMSM topologies based on the rotor configuration. (a). Surface PMSM. (b). Inset PMSM. (c). Interior PMSM with radial magnetization. (d). Interior PMSM with tangential magnetization.

4.2 Review of the Conventional PMSM Model

Based on the rotor configurations, conventional PM machines are classified into surface, inset and interior permanent magnet machines. Fig. 4.1 shows four different PMSM topologies based on rotor magnet configuration. In all of these PMSM topologies, the magnet d-axis is either aligned along the maximum reluctance axis or the minimum reluctance axis. The magnet d-axis in surface PMSM and interior PMSM with tangential magnetization align along the minimum reluctance axis, while it aligns along the maximum reluctance axis in inset and interior PMSMs. The peak reluctance and peak magnet torques in conventional PMSMs are phase shifted by $45°$.

The characteristics of a regular PMSM is defined by (4.1)–(4.3).

$$\begin{bmatrix}\psi_q\\ \psi_d\end{bmatrix} = \begin{bmatrix}L_q & 0\\ 0 & L_d\end{bmatrix}\begin{bmatrix}i_q\\ i_d\end{bmatrix} + \psi_m\begin{bmatrix}0\\ 1\end{bmatrix} \tag{4.1}$$

$$\begin{bmatrix}v_q\\ v_d\end{bmatrix} = r_s\begin{bmatrix}i_q\\ i_d\end{bmatrix} + \frac{d}{dt}\begin{bmatrix}\psi_q\\ \psi_d\end{bmatrix} + \omega_r\begin{bmatrix}0 & 1\\ -1 & 0\end{bmatrix}\begin{bmatrix}\psi_q\\ \psi_d\end{bmatrix} \tag{4.2}$$

$$T_e = \frac{3}{2}\frac{P}{2}[\psi_m i_q + \frac{1}{2}(L_d - L_q)i_q i_d] \tag{4.3}$$

where, ψ_m is the magnet flux linkage, $\psi_q = L_q i_q$, $\psi_d = \psi_m + L_d i_d$ are the q- and d- axes flux linkages, L_q and L_d are the q- and d- axes inductances, v_q, v_d and i_q, i_d are the qd reference frame voltages and currents respectively, r_s is the stator resistance, ω_r is the electrical angular speed of the rotor. If δ is the angle by which the stator current vector (resultant of i_d and i_q) leads the rotor d-axis, the torque equation can be rewritten as shown in (4.4). Here, δ is known as the torque angle. Since it is also the angular location of the stator current vector with respect to i_d, it is also called current angle.

$$T_e = \frac{3}{2}\frac{P}{2}[\psi_m i_s \sin\delta + \frac{1}{2}(L_d - L_q)i_s^2 \sin 2\delta] \tag{4.4}$$

4.3 Mathematical Model of the Shifted IPMSM

In the regular IPMSM, the current angle at which the magnet torque peaks is different from the current angle at which the reluctance torque peaks. Ideally, the magnet torque peaks at the torque-angle of $90°$ and the reluctance torque peaks at the torque angle of $135°$ in the regular IPMSMs. Due to the phase shift in the peak magnet and peak reluctance torques, the total electromagnetic torque is less than the sum of individual peak torques. Fig. 4.2 shows the per unit magnet torque, reluctance torque and total torque of an arbitrary IPMSM. The peak torque of the regular IPMSM occurs at the torque angle between $90°$ and $135°$. Of course this angle changes with current magnitude, making the maximum torque per ampere (MTPA) trajectory a non-linear function of the torque-angle. In vehicle applications, operation of the IPMSM along the maximum torque per ampere trajectory is important.

In the new class of IPMSM presented in [36], a phase shift is introduced between the magnet d-axis and reluctance axis to obtain the peak magnet torque and peak reluctance torque at the same torque angle. It is called the shifted IPMSM. The fundamental difference between the regular IPMSM and the shifted IPMSM is that the magnet d-axis is either aligned with the maximum or minimum reluctance axis in the former while it is in between the maximum and the minimum reluctance axes in the later. This chapter develops the machine model for the shifted IPMSM so that the behavior of such machine can be studied. The developed mathematical model is also useful in the design of the control algorithms for such a machine.

In the derivation of the mathematical model of the shifted IPMSM, the following assumptions are made.

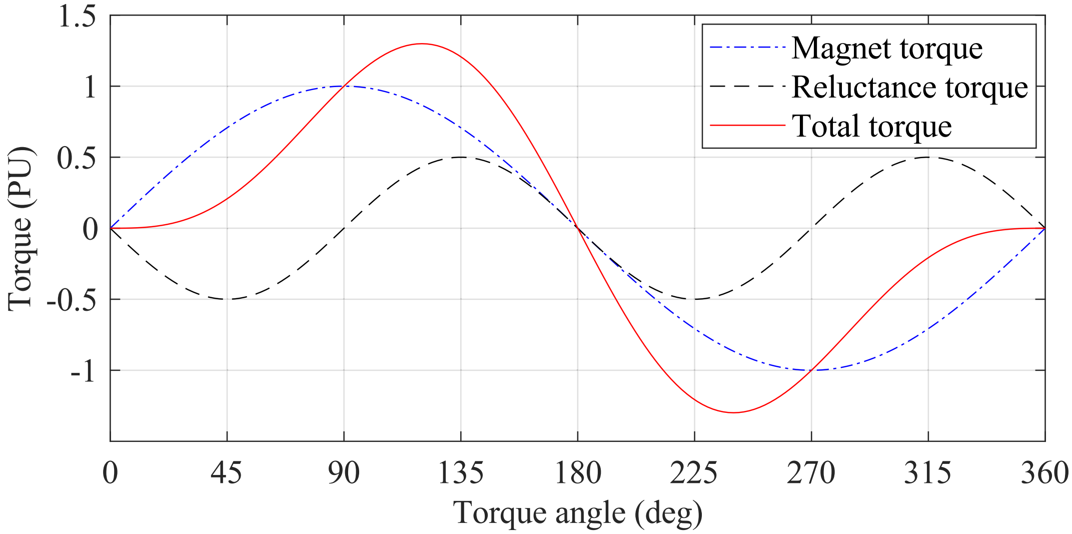

Fig. 4.2: Torque-angle curves of an arbitrary regular IPMSM showing magnet torque, reluctance torque and the total torque.

- The windings are sinusoidally distributed.
- The air-gap distribution is sinusoidal at double the frequency of the winding distribution.
- The effect of harmonics due to stator slots are neglected.
- A two pole machine structure is considered.
- The rotor position, θ_r is the position of q-axis with respect to the stator phase a-axis.

The assumptions made above simplifies the development of the dynamic equations representing the shifted IPMSM. In the first step, the machine inductances and dynamic equations in the abc frame are derived using the geometrical and winding data in basic magnetic equations relating current, MMF and flux density. The next step is the transformation of the equations from the abc frame to the qd reference frame.

4.3.1 Development of Machine Inductances

Fig. 4.3 presents a simplified two pole three phase motor structure used to develop the mathematical model of the shifted IPMSM. The reference frame d-axis is chosen to be along the magnet d-axis, and the rotor position is measured from phase a-axis to the reference frame q-axis, which is 90° ahead of the magnet d-axis. The spatial location of the stator from the phase a-axis is β_s, and the spatial location of the stator from the rotor q-axis is β_r. Due to the shift in the reluctance axis, the minimum air-gap axis is in between the d- and q-axes. The air-gap varies sinusiodally along the

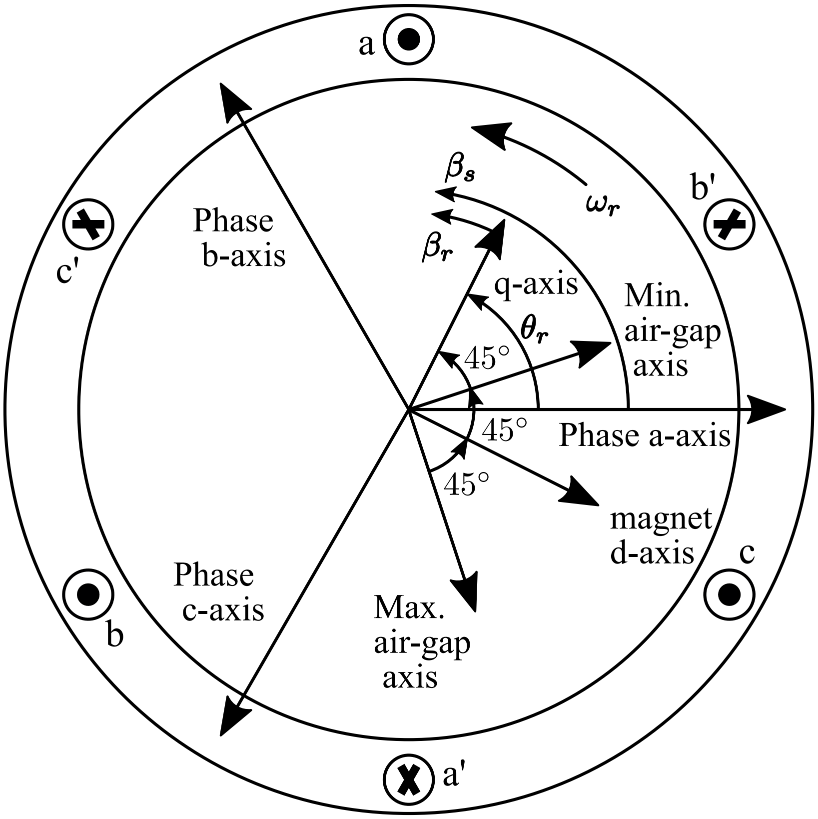

Fig. 4.3: Simplified two pole three phase structure used for modeling the shifted IPMSM.

spatial location at double the frequency. The air-gap distribution is represented by a function similar to the one in [112].

$$\begin{aligned} g(\beta_r) = g(\beta_r + \pi) &= \frac{1}{\alpha_1 - \alpha_2 \sin 2\beta_r} \\ &= \frac{1}{\alpha_1 - \alpha_2 \sin 2(\beta_s - \theta_r)} \end{aligned} \tag{4.5}$$

where, α_1 is the inverse of harmonic mean of the maximum and minimum air-gap lengths, and α_2 is the parameter relating the air-gap range with the geometric mean of the maximum and minimum air-gap lengths. The choice of air-gap distribution function in (4.5) facilitates the development of the machine model. The MMF distributions due to individual phase excitation are given by (4.6)–(4.8).

$$MMF_{as} = \frac{N_s}{2} i_a \cos \beta_s \tag{4.6}$$

$$MMF_{bs} = \frac{N_s}{2} i_b \cos(\beta_s - 2\pi/3) \tag{4.7}$$

$$MMF_{cs} = \frac{N_s}{2} i_c \cos(\beta_s - 4\pi/3) \tag{4.8}$$

where, $N_s/2$ is the total number of stator turns in each phase, i_a, i_b and i_c are the phase currents. The MMF distribution is used to obtain the air-gap flux density distribution due to individual phase excitation. Neglecting the steel reluctance, the air-gap flux distribution due to individual phase excitation are given by (4.9)–(4.11). Here μ_o is the air permeability.

$$B_{as} = \mu_o \frac{N_s}{2} i_a \cos\beta_s [\alpha_1 - \alpha_2 \sin 2(\beta_s - \theta_r)] \tag{4.9}$$

$$B_{bs} = \mu_o \frac{N_s}{2} i_b \cos(\beta_s - 2\pi/3) [\alpha_1 - \alpha_2 \sin 2(\beta_s - \theta_r)] \tag{4.10}$$

$$B_{cs} = \mu_o \frac{N_s}{2} i_c \cos(\beta_s - 4\pi/3) [\alpha_1 - \alpha_2 \sin 2(\beta_s - \theta_r)] \tag{4.11}$$

The flux density distributions are used to obtain the flux linkage of the sinusoidally distributed windings. The integrals (4.12)–(4.14) give the phase A flux linkage due to excitation in phases A, B and C respectively.

$$\psi_{aa} = L_{ls} i_{as} + \int_{\pi}^{2\pi} \big(-\frac{N_s}{2} \sin\beta_s \big) \big[\int_{\zeta}^{\zeta+\pi} B_{as}(\zeta, \theta_r) r l \partial\zeta \big] \partial\beta_s \tag{4.12}$$

$$\psi_{ab} = \int_{\pi}^{2\pi} \big(-\frac{N_s}{2} \sin\beta_s \big) \big[\int_{\zeta}^{\zeta+\pi} B_{bs}(\zeta, \theta_r) r l \partial\zeta \big] \partial\beta_s \tag{4.13}$$

$$\psi_{ac} = \int_{\pi}^{2\pi} \big(-\frac{N_s}{2} \sin\beta_s \big) \big[\int_{\zeta}^{\zeta+\pi} B_{cs}(\zeta, \theta_r) r l \partial\zeta \big] \partial\beta_s \tag{4.14}$$

$$\psi_{ba} = \int_{\pi+2\pi/3}^{2\pi+2\pi/3} \big(-\frac{N_s}{2} \sin(\beta_s - 2\pi/3) \big) \big[\int_{\zeta}^{\zeta+\pi} B_{as}(\zeta, \theta_r) r l \partial\zeta \big] \partial\beta_s \tag{4.15}$$

$$\psi_{bb} = L_{ls} i_{bs} + \int_{\pi+2\pi/3}^{2\pi+2\pi/3} \big(-\frac{N_s}{2} \sin(\beta_s - 2\pi/3) \big) \big[\int_{\zeta}^{\zeta+\pi} B_{bs}(\zeta, \theta_r) r l \partial\zeta \big] \partial\beta_s \tag{4.16}$$

$$\psi_{bc} = \int_{\pi+2\pi/3}^{2\pi+2\pi/3} \big(-\frac{N_s}{2} \sin(\beta_s - 2\pi/3) \big) \big[\int_{\zeta}^{\zeta+\pi} B_{cs}(\zeta, \theta_r) r l \partial\zeta \big] \partial\beta_s \tag{4.17}$$

$$\psi_{ca} = \int_{\pi+4\pi/3}^{2\pi+4\pi/3} \big(-\frac{N_s}{2} \sin(\beta_s - 4\pi/3) \big) \big[\int_{\zeta}^{\zeta+\pi} B_{as}(\zeta, \theta_r) r l \partial\zeta \big] \partial\beta_s \tag{4.18}$$

$$\psi_{cb} = \int_{\pi+4\pi/3}^{2\pi+4\pi/3} \big(-\frac{N_s}{2} \sin(\beta_s - 4\pi/3) \big) \big[\int_{\zeta}^{\zeta+\pi} B_{bs}(\zeta, \theta_r) r l \partial\zeta \big] \partial\beta_s \tag{4.19}$$

$$\psi_{cc} = L_{ls} i_{cs} + \int_{\pi+4\pi/3}^{2\pi+4\pi/3} \big(-\frac{N_s}{2} \sin(\beta_s - 4\pi/3) \big) \big[\int_{\zeta}^{\zeta+\pi} B_{cs}(\zeta, \theta_r) r l \partial\zeta \big] \partial\beta_s \tag{4.20}$$

where, ψ_{aa}, ψ_{ab}, ψ_{ac} are the phase A flux linkages due to excitation in phases A, B and C respectively, ψ_{ba}, ψ_{bb}, ψ_{bc} are the phase B flux linkages due to excitation in phases A, B and C respectively, ψ_{ca}, ψ_{cb}, ψ_{cc} are the phase C flux linkages due to excitation in phases A, B and C respectively, L_{ls} is the per phase leakage inductance, l is the machine stack length and r is the rotor outer radius. The inductance matrix in abc reference frame is obtained from these flux linkages. The integrals are solved using symbolic toolbox in MATLAB and the source code is attached in the appendix A. The following is the expression for the inductance matrix obtained.

$$
\begin{aligned}
L_{abc} = &\begin{bmatrix} L_{ls}+L_{ms} & -\frac{1}{2}L_{ms} & -\frac{1}{2}L_{ms} \\ -\frac{1}{2}L_{ms} & L_{ls}+L_{ms} & -\frac{1}{2}L_{ms} \\ -\frac{1}{2}L_{ms} & -\frac{1}{2}L_{ms} & L_{ls}+L_{ms} \end{bmatrix} + \\
&L_{\delta} \begin{bmatrix} \sin 2\theta_r & \sin(2\theta_r-\phi) & \sin(2\theta_r+\phi) \\ \sin(2\theta_r-\phi) & \sin(2\theta_r+\phi) & \sin 2\theta_r \\ \sin(2\theta_r+\phi) & \sin 2\theta_r & \sin(2\theta_r-\phi) \end{bmatrix}
\end{aligned} \tag{4.21}
$$

where, L_{abc} is the per phase inductance matrix, L_{ms} is the mean self-magnetizing inductance, L_{δ} is the peak of the self-magnetizing inductance ripple over the rotor positions, and $\phi = 2\pi/3$. Their relation with the physical variables are given in (4.22) and (4.23).

$$L_{ms} = \mu_o\left(\frac{N_s}{2}\right)^2 \pi r l \alpha_1 \tag{4.22}$$

$$L_{\delta} = \frac{1}{2}\mu_o\left(\frac{N_s}{2}\right)^2 \pi r l \alpha_2 \tag{4.23}$$

Considering the flux linkage due to rotor magnets, the flux linkage vector and the stator voltage equation in the abc frame are given by (4.24) and (4.25), where ψ_{abc} is the flux linkage vector in abc frame, ψ_m is the magnet flux linkage, and r_s is the stator per phase resistance.

$$\psi_{abc} = [L_{abc}]\begin{bmatrix} i_a \\ i_b \\ i_c \end{bmatrix} + \psi_m \begin{bmatrix} \sin\theta_r \\ \sin(\theta_r - 2\pi/3) \\ \sin(\theta_r - 4\pi/3) \end{bmatrix} \tag{4.24}$$

$$v_{abc} = r_s i_{abc} + \frac{d}{dt}\psi_{abc} \tag{4.25}$$

4.3.2 Machine Dynamics in Rotor Reference Frame

In order to obtain the dynamic equations in the qd reference frame, the procedure presented in [113] is followed. The transformation matrix from abc frame to rotating $qd0$ reference frame and its inverse are given by (4.26) and (4.27).

$$K_s = \frac{2}{3}\begin{bmatrix} \cos\theta_r & \cos(\theta_r - 2\pi/3) & \cos(\theta_r - 4\pi/3) \\ \sin\theta_r & \sin(\theta_r - 2\pi/3) & \sin(\theta_r - 4\pi/3) \\ \frac{1}{2} & \frac{1}{2} & \frac{1}{2} \end{bmatrix} \tag{4.26}$$

$$K_s^{-1} = \begin{bmatrix} \cos\theta_r & \sin\theta_r & 1 \\ \cos(\theta_r - 2\pi/3) & \sin(\theta_r - 2\pi/3) & 1 \\ \cos(\theta_r - 4\pi/3) & \sin(\theta_r - 4\pi/3) & 1 \end{bmatrix} \tag{4.27}$$

Applying these transformations to (4.24) and (4.25) yields the following in the $qd0$ reference frame.

$$\begin{bmatrix} \psi_q \\ \psi_d \end{bmatrix} = \begin{bmatrix} L_s & L_\Delta \\ L_\Delta & L_s \end{bmatrix} \begin{bmatrix} i_q \\ i_d \end{bmatrix} + \psi_m \begin{bmatrix} 0 \\ 1 \end{bmatrix} \tag{4.28}$$

$$\begin{bmatrix} v_q \\ v_d \end{bmatrix} = r_s \begin{bmatrix} i_q \\ i_d \end{bmatrix} + \frac{d}{dt}\begin{bmatrix} \psi_q \\ \psi_d \end{bmatrix} + \omega_r \begin{bmatrix} 0 & 1 \\ -1 & 0 \end{bmatrix} \begin{bmatrix} \psi_q \\ \psi_d \end{bmatrix} \tag{4.29}$$

$$T_e = \frac{3}{2}\frac{P}{2}[\psi_m i_q + L_\Delta(i_q^2 - i_d^2)] \tag{4.30}$$

$$L_s = L_{ls} + \frac{3}{2}L_{ms} \tag{4.31}$$

$$L_\Delta = \frac{3}{2}L_\delta \tag{4.32}$$

where, L_s is the mean magnetizing inductance, and L_Δ is the peak of the magnetizing inductance ripple over the rotor positions. The expression for the torque in (4.30) is obtained from the cross product of flux linkage vector and current vector. The equations (4.28)–(4.30) form the mathematical model of the shifted IPMSM.

4.3.3 Alternative Form of the Model

The mathematical model represented by (4.28)–(4.30) are derived with the reference d-axis along the magnet d-axis. In this form of the model, the d-axis flux linkage is also affected by q-axis current and vice versa. When the reference frame d-axis is aligned along the maximum reluctance axis (axis along which the air-gap length is maximum), an alternative sets of equations representing the shifted IPMSM are obtained. The air-gap distribution function is represented by (4.33).

$$\begin{aligned} g(\beta_r) = g(\beta_r + \pi) &= \frac{1}{\alpha_1 + \alpha_2 \cos 2\beta_r} \\ &= \frac{1}{\alpha_1 + \alpha_2 \cos 2(\beta_s - \theta_r)} \end{aligned} \tag{4.33}$$

The MMF distribution function would be represented by the same equations in (4.6)-(4.8). Following a similar procedure presented above, the following relation is obtained for the inductance matrix in abc frame.

$$\begin{aligned} L_{abc} = &\begin{bmatrix} L_{ls} + L_{ms} & -\frac{1}{2}L_{ms} & -\frac{1}{2}L_{ms} \\ -\frac{1}{2}L_{ms} & L_{ls} + L_{ms} & -\frac{1}{2}L_{ms} \\ -\frac{1}{2}L_{ms} & -\frac{1}{2}L_{ms} & L_{ls} + L_{ms} \end{bmatrix} + \\ &L_\delta \begin{bmatrix} \cos 2\theta_r & \cos(2\theta_r - \phi) & \cos(2\theta_r + \phi) \\ \cos(2\theta_r - \phi) & \cos(2\theta_r + \phi) & \cos 2\theta_r \\ \cos(2\theta_r + \phi) & \cos 2\theta_r & \cos(2\theta_r - \phi) \end{bmatrix} \end{aligned} \tag{4.34}$$

The machine dynamics in the abc frame are given by (4.35) and (4.36).

$$\psi_{abc} = [L_{abc}] \begin{bmatrix} i_a \\ i_b \\ i_c \end{bmatrix} + \psi_m \begin{bmatrix} \sin(\theta_r - \pi/4) \\ \sin(\theta_r - \pi/4 - 2\pi/3) \\ \sin(\theta_r - \pi/4 - 4\pi/3) \end{bmatrix} \tag{4.35}$$

$$v_{abc} = r_s i_{abc} + \frac{d}{dt}\psi_{abc} \tag{4.36}$$

Transforming these dynamic equations in the abc frame to the qd reference frame as defined by the transformations in (4.26) and (4.27), the following dynamic equations in qd reference frame are obtained.

$$\begin{bmatrix} \psi_q \\ \psi_d \end{bmatrix} = \begin{bmatrix} L_q & 0 \\ 0 & L_d \end{bmatrix} \begin{bmatrix} i_q \\ i_d \end{bmatrix} + \psi_m \begin{bmatrix} \frac{1}{\sqrt{2}} \\ \frac{1}{\sqrt{2}} \end{bmatrix} \tag{4.37}$$

$$\begin{bmatrix} v_q \\ v_d \end{bmatrix} = r_s \begin{bmatrix} i_q \\ i_d \end{bmatrix} + \frac{d}{dt} \begin{bmatrix} \psi_q \\ \psi_d \end{bmatrix} + \omega_r \begin{bmatrix} 0 & 1 \\ -1 & 0 \end{bmatrix} \begin{bmatrix} \psi_q \\ \psi_d \end{bmatrix} \tag{4.38}$$

$$T_e = \frac{3}{2}\frac{P}{2}\left[\frac{\psi_m}{\sqrt{2}}(i_q - i_d) + (L_d - L_q) i_q i_d\right] \tag{4.39}$$

where, $L_q = L_{ls} + \frac{3}{2}L_{ms} + \frac{3}{2}L_\delta = L_s + L_\Delta$ is the q-axis inductance, and $L_d = L_{ls} + \frac{3}{2}L_{ms} - \frac{3}{2}L_\delta = L_s - L_\Delta$ is the d-axis inductance. The expressions (4.37)-(4.39) represents an alternative form of the mathematical model of the shifted IPMSM.

4.3.4 Interpretation of the Developed Model

The expressions (4.28)–(4.30) and (4.37)–(4.39) represent two different forms of the mathematical model of the shifted IPMSM. In (4.28)–(4.30), the reference d-axis is aligned along the magnet flux axis, and it is aligned along the maximum reluctance axis in (4.37)–(4.39). Comparing (4.28) and (4.37), it is seen that the qd flux linkages in the former form depends on both i_q and i_d. The inductance term L_Δ is similar to cross-magnetizing inductance. However, the latter form shows that the cross-dependency of qd flux linkages on $i_q i_d$ disappear for the reference frame d-axis align along the maximum reluctance axis. Comparing the torque equations in (4.30) and (4.39), the reluctance torque in the former is similar to the asymmetric torque in [41]. In the latter form however, it is similar to the reluctance torque in [41]. Based on these two expressions, it can be concluded that the asymmetric torque discussed in [41] is a part of reluctance torque that appears in a different form.

Comparing the dynamics of the machine represented by (4.29) and (4.38), the dynamics in i_q and i_d show cross dependency in the former. Due to this reason, design of the current controllers in the former form becomes more complicated. However, the torque equation in (4.30) shows that the maximum torque is obtained for $i_d = 0$ and thus the speed controller design becomes simpler compared to the model represented by (4.37)-(4.39). This is because both i_d and i_q need to be changed with the load torque when operated at MTPA with the latter model. Thus, both forms of the model have their own significance.

Compared to (4.1)–(4.3), it is seen that both the flux linkages ψ_q and ψ_d are functions of i_q and i_d in the shifted IPMSM model represented by (4.28)–(4.30). In the regular IPMSM, when the d-axis current is zero, the reluctance torque is zero and the electromagnetic torque has a linear relationship with i_q. However, in the shifted IPMSM, the torque is a non-linear function of i_q except for the conditions when i_q equals i_d. In the regular IPMSM, the MTPA trajectory is a non-linear function of torque angle. In contrast, the electromagnetic torque is maximum when i_d is zero for the shifted IPMSM. Due to this reason, the MTPA trajectory is a constant torque-angle. Thus, the MTPA operation of the shifted IPMSM is simpler below the base speed. Based on (4.28), application of positive i_q also enhances the d-axis flux linkage, positive torque production always tend to increase the air-gap flux. Such a nature of flux linkage coupling complicates the understanding of air-gap flux linkage. Although the flux linkages are decoupled with i_d and i_q in the alternative model, the electromagnetic torque depends on both currents and the torque control requires adjustment of both currents. Thus, the developed model predicts that the operation of the shifted IPMSM is simpler below the base speed and it is more complicated in the field weakening region.

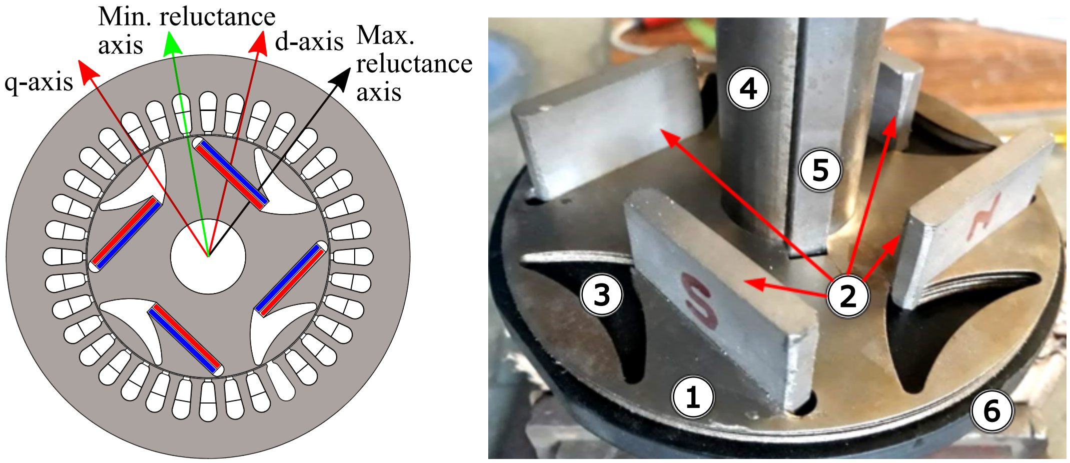

(a) (b)

Fig. 4.4: Motor prototyping. (a). Motor geometry. (b). Prototyped rotor. 1. Rotor lamination stack. 2. SmCo18 magnets. 3. Air barrier. 4. Shaft. 5. Key-way. 6. Bakelite end-plate.

4.4 Design Specifications and Prototyping

In order to validate the concepts of aligning the magnet torque with the reluctance torque, the motor designed in [36] is prototyped. Fig. 4.4 shows the motor geometry and a picture during the rotor assembly. Fig. 4.4a shows the motor geometry along with the direction of the direct axis, quadrature axis, maximum reluctance axis and minimum reluctance axis. From the rotor geometry, it is clearly seen that there is no axis of symmetry. Fig. 4.4b shows a picture during insertion of the magnets in the rotor assembly. Parts of the rotor assembly are also labeled. Table 4.1 presents the design specifications of the prototyped motor. IT is a four pole motor using SmCo magnets. The stator consists of a double layer lap winding with a short pitch of one slot, and it is skewed by one slot. The rotor structure contains air barriers to shift the reluctance axis.

Table 4.1: Specifications of the prototyped machine.

Rated power (hp)	6
Rated speed (rpm)	1775
Rated current (A)	14.142
Rated voltage (V)	220
Number of poles	4
Number of slots	36
Winding configuration	8/9 double layer
Stator outer diameter (mm)	180
Rotor outer diameter (mm)	108
Stack length (mm)	125
Air-gap length (mm)	0.5
Magnet length (mm)	40.33
Magnet width (mm)	6
Magnet type	SmCo grade 18

4.5 Experimental Validation

Based on the developed mathematical model, the shifted IPMSM parameters are ψ_m, r_s, L_s and L_Δ. In order to validate the developed machine model, these parameters are obtained experimentally. The experimentally obtained parameters are used in the developed mathematical model to obtain the torque characteristic of the motor. To measure the machine parameters and validate the developed model, an experimental setup is built to measure the back-emf, inductances and torque-angle curves of the machine. Fig. 4.5 shows the test setup used to perform the tests on the prototyped machine. It consists of a prototyped motor, torque-meter (MCRT®2903T), voltage and current sensors, OPAL-RT OP4510 control and prototyping real time system, adjustable test bench, dc dynamometer, and an absolute position encoder. The experimental test consists of locating rotor d-axis, magnet flux linkage measurement, inductance and resistance measurement, and torque measurement.

4.5.1 Locating the Rotor d-axis

In traditional PMSMs, the magnet d-axis is aligned either along the minimum reluctance axis or along the maximum reluctance axis. In order to find the magnet d-axis, a dc current of magnitude I is applied to the machine such that $i_a = I$ and $i_b = i_c = -I/2$. With this, the magnet d-axis will

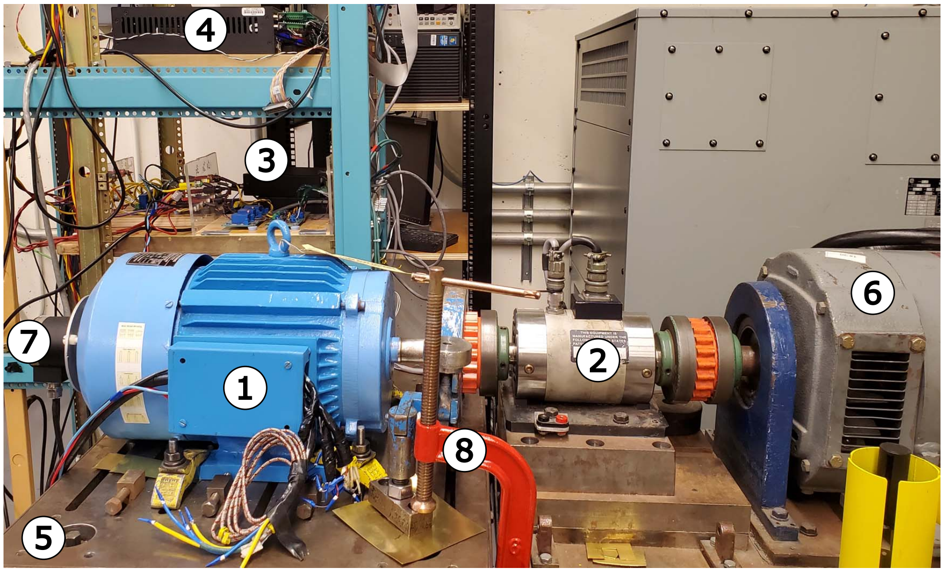

Fig. 4.5: Experimental test setup. 1. Prototyped motor. 2. Torque-meter. 3. Voltage and current sensors. 4. OPAL-RT OP4510 system. 5. Test bench with adjustable test bed. 6. DC dynamometer. 7. Position encoder. 8. Mechanical clamp.

align along the phase a-axis. The same statement holds true for a traditional synchronous reluctance machine. However, the shifted IPMSM design has an asymmetrical rotor structure. The magnet d-axis is not aligned along either of the maximum and minimum reluctance axes. Due to this, when a current is applied to the motor such that $I_a = I$ and $I_b = I_c = -I/2$, the rotor d-axis does not align along the phase a-axis.

In order to find the rotor d-axis position, the machine is run as a generator at a fixed speed. The machine back EMF and the absolute rotor position are measured and recorded. Fig. 4.6 shows a plot of phase A back EMF and the rotor position measured by an absolute position encoder when the machine is run as a generator at a speed of 600 rpm. The fundamental component of the phase A back EMF is obtained using FFT analysis. Based on the abc to $qd0$ transformation in (4.26), the rotor position is zero when the q-axis is aligned with the stator phase a-axis. With this convention, when the phase of the fundamental phase A back EMF is $180°$, the rotor d-axis is along the phase a-axis. The rotor position at this instant is noted and, a phase shift is applied to it such that θ_r is $90°$ at this instant as per the transformation defined by (4.26). Thus, whenever θ_r is $90°$, the rotor d-axis is aligned along the phase a-axis. This is the procedure to obtain the relative position of the rotor d-axis with phase a-axis.

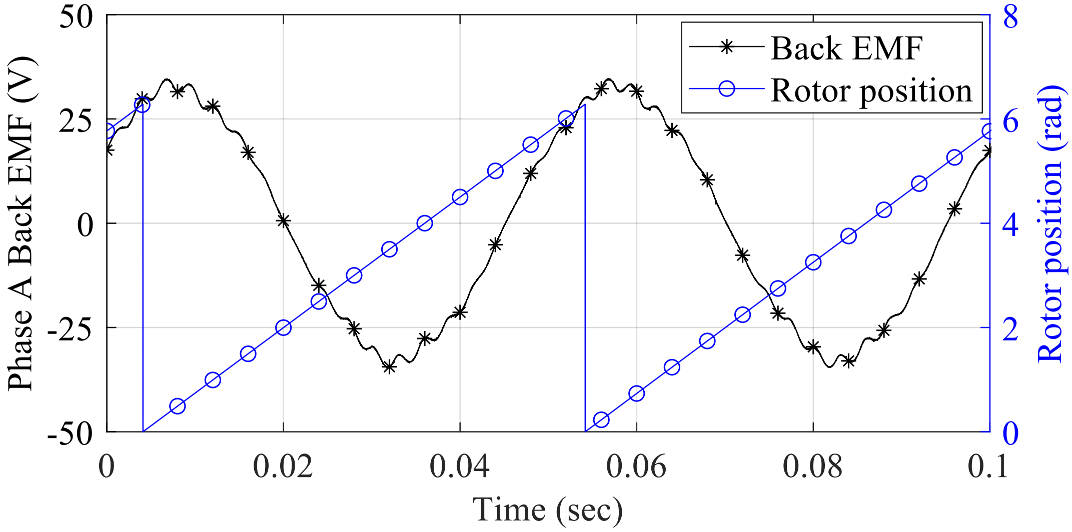

Fig. 4.6: Measured back EMF and the rotor position when the machine is run as a generator at 600 rpm.

4.5.2 Magnet Flux Linkage Measurement

In order to measure the magnet flux linkage, the mechanical clamp shown in Fig. 4.5 is removed, and the test motor is run as an open circuited generator by running the dynamometer in motoring mode. The three phase back EMFs are measured and recorded for different speeds. Based on (4.24), the magnet flux linkage is defined as the peak value of the coil flux linkages when no current flows in the coils. From (4.25), the open circuited terminal voltage is the rate of change of coil flux linkage. Since the fundamental component is of interest, the magnet flux linkage, ψ_m is obtained from (4.40).

$$\psi_m = \frac{V_{a1(peak)}}{\omega_r} \tag{4.40}$$

where, $V_{a1(peak)}$ is the peak value of the fundamental back EMF when the machine is rotated at an electrical speed of ω_r. In order to obtain a better estimate of the magnet flux linkage, the three phase back EMFs at different speeds are recorded, and peak values of the fundamental back EMFs are obtained from FFT analysis of the recorded waveforms. The magnet flux linkage, ψ_m is computed as the average of the magnet flux linkages computed at each speed for all the phases.

4.5.3 Inductance and Resistance Measurement

Based on the mathematical model represented by (4.28) to (4.30), the machine parameters are L_s, L_Δ, r_s and ψ_m. In the alternative model represented by (4.37) to (4.39), the parameters L_d,

L_q, r_s and ψ_m are enough to establish the model. The L_q is the sum of L_s and L_Δ, and L_d is the difference of L_s and L_Δ. Thus, two inductance terms viz; L_s and L_Δ along with r_s and ψ_m are enough to establish the mathematical models of the shifted IPMSM in the qd reference frame.

In the abc reference frame, the stator inductance varies with the rotor position. The stator self inductance has a constant term and a variable term that varies sinusoidally at double frequency. Since the measurement of L_Δ requires the position dependent inductances, it is proposed to keep the current vector fixed in space and measure the phase inductance at rotor positions extending one electrical cycle in stationary reference frame. When the reference frame is stationary, the $\alpha\beta 0$ transformation shown in (4.41) is used.

$$K_{ss} = \frac{2}{3}\begin{bmatrix} 1 & -\frac{1}{2} & -\frac{1}{2} \\ 0 & \frac{\sqrt{3}}{2} & -\frac{\sqrt{3}}{2} \\ \frac{1}{2} & \frac{1}{2} & \frac{1}{2} \end{bmatrix} \tag{4.41}$$

The machine currents are such that $i_a = i_{ref}$, $i_b = -i_{ref}/2$ and $i_c = -i_{ref}/2$. Applying the transformation defined by (4.41) to the machine equation in 4.24 for this particular case, the β-axis current and flux linkage are zero while the followings expressions for the α-axis current, i_α and flux linkage, ψ_α are obtained.

$$i_\alpha = i_{ref} \tag{4.42}$$

$$\psi_\alpha = (L_s + L_\Delta \sin 2\theta_r) i_{ref} \tag{4.43}$$

where, L_s, and L_Δ are the same inductances in (4.28). Thus, the α-axis inductance is obtained as the ratio of ψ_α and i_α as presented in (4.44).

$$L_\alpha = \frac{\psi_\alpha}{i_\alpha} = L_s + L_\Delta \sin 2\theta_r; \tag{4.44}$$

The FFT of the measured L_α waveform would give the parameters L_s and L_Δ.

In order to measure the machine inductances, the automated current control method presented in [16] is used with some modifications. This method uses the transient response of the motor to measure the machine inductance, and both the resistance and inductance are measured simultaneously. As shown in Fig. 4.5, the motor shaft is locked at a fixed position using a mechanical clamp. This is the same test setup used to measure the back EMF. The outputs of a three phase VSI are connected to the terminals of the wye connected motor. An absolute position encoder is used to measure the rotor position. Fig. 4.7 presents the schematics of the control structure. OPAL-RT OP4510 real time system for control and prototyping applications is used to control the phase

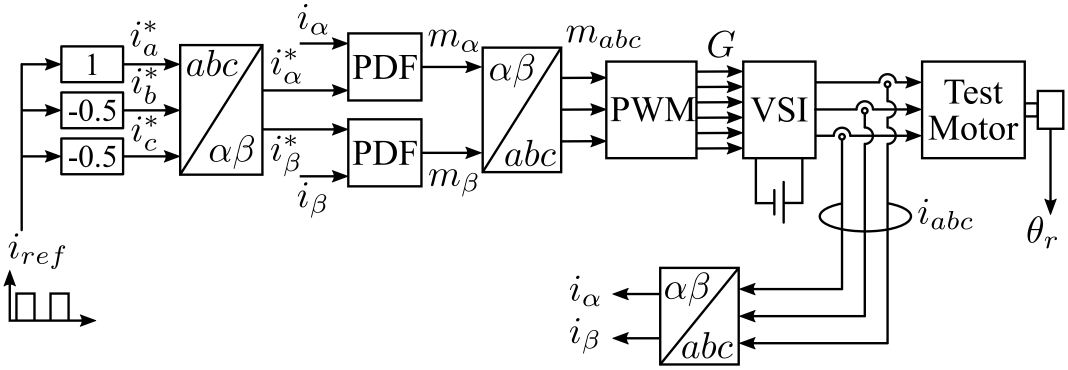

Fig. 4.7: Schematics of the control structure using PDF controllers to measure the phase inductance due to three phase excitation.

currents and compute the inductance, L_α and phase resistance, r_s. The reference to the controller is a pulsed stator reference current, i_{ref} aligned along phase a-axis. Both the reference and measured currents in abc frame are transformed to $\alpha\beta0$ reference frame. Pseudo-derivative feedback (PDF) controllers are used to control the currents to obtain the desired transient response. For a desired settling time, details on the design of PDF controllers are presented in [80]. For this particular test, a settling time of 0.5 S was chosen. Based on the discussion presented in chapter 2, the number of measurement samples are adequate for the chosen settling time. The modulation references generated by the controllers are used to generate the PWM signals to drive the VSI. In order to reduce the current ripple, a reduced dc link voltage is applied to the VSI. The voltages and currents in the machine are measured and processed in real-time in the controller. The followings are the expressions implemented in real time to compute L_α and r_s.

$$L_\alpha = \frac{1}{i_{ref}} \int_0^t [v_\alpha(\tau) - i_\alpha(\tau) r_s] d\tau \tag{4.45}$$

$$r_s = \left. \frac{v_\alpha}{i_\alpha} \right|_{steady} \tag{4.46}$$

where, $v_\alpha(\tau)$ and $i_\alpha(\tau)$ are the instantaneous values of v_α and i_α. In this method, r_s is measured as the ratio of steady state v_α to steady state i_α. In the method presented, the measurement of L_α and r_s for different magnitudes of currents are automated in the real-time controller.

The α-axis inductance at different current magnitudes and rotor positions extending to one pole pair is measured. For each current magnitude and rotor position, several measurements are taken and averaged to obtain the mean. Fig. 4.8 presents the measured α-axis inductance at two current magnitudes, for rotor positions extending from $0°$ to $360°$ electrical. The plot shows that the measured inductance has a constant component and a sinusoidal component at double the frequency. A FFT analysis of the inductance waveforms is done in MATLAB to obtain the harmonic content

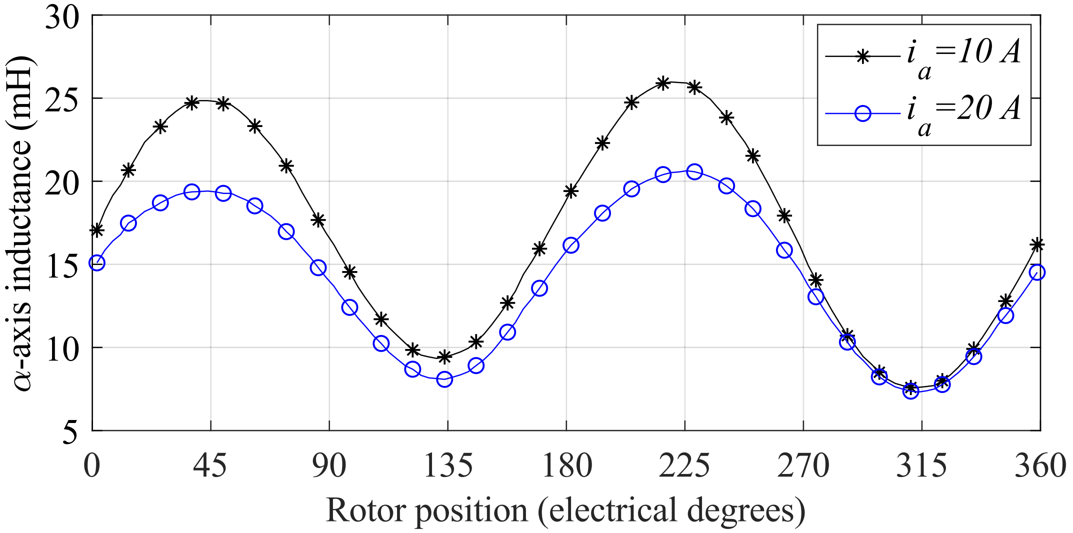

Fig. 4.8: Measured α-axis inductance variation with the rotor position at two current magnitudes.

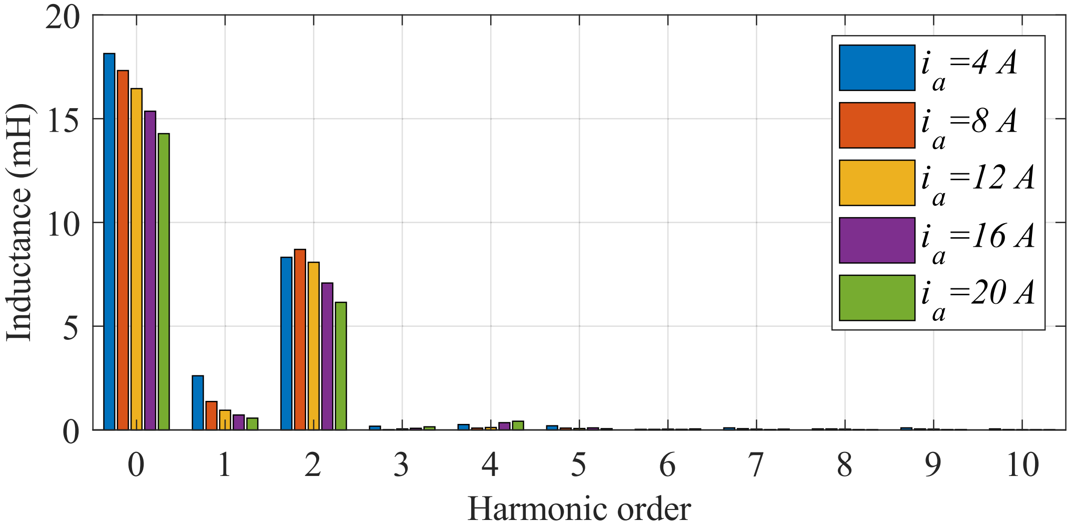

Fig. 4.9: Harmonics in the measured inductances at five different current magnitudes obtained using FFT.

in the machine inductance. Fig. 4.9 presents the harmonics in the measured inductances at five different current magnitudes obtained using FFT. It shows that the average inductance over the rotor positions (constant component) reduces with an increase in the current magnitude. This is due to core saturation at higher currents. The plot also shows that harmonic inductances of first order exist. It is due to the asymmetric rotor structure and reversal of the magnet flux direction when the rotor is rotated by $180°$. However, its magnitude is lower compared to the constant and dominant harmonic component. As expected, the dominant harmonics are of second order and all other higher order harmonics are negligible. In the FFT plot obtained, the average component is L_s and the second order harmonic is L_Δ.

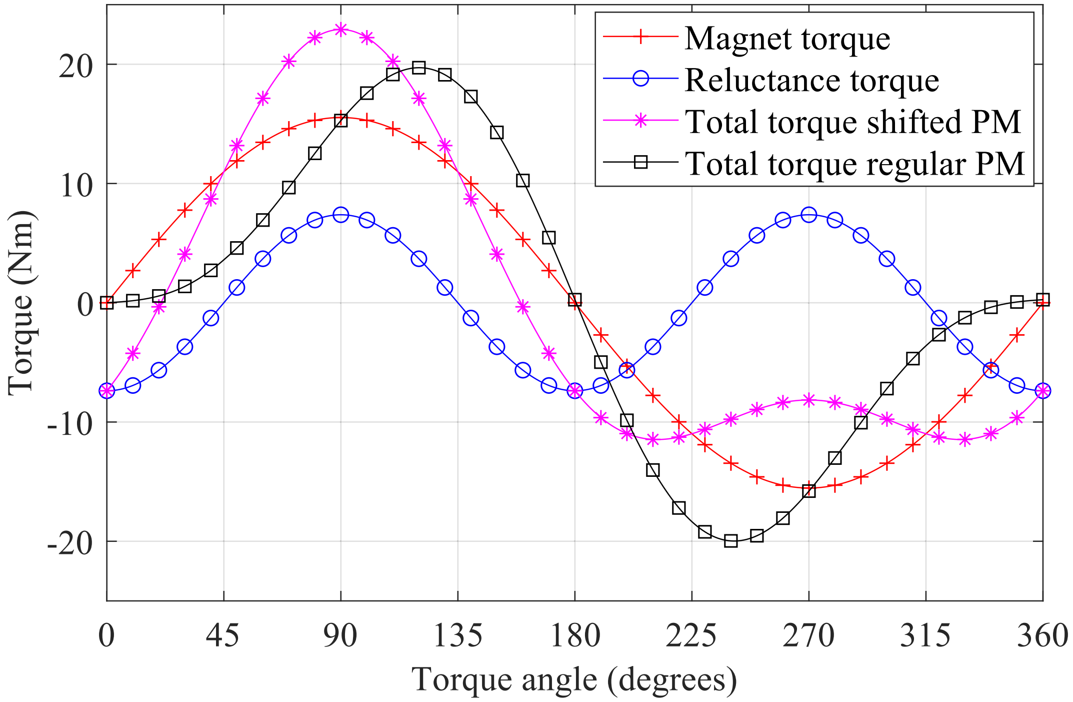

Fig. 4.10: Breakdown of the total torque at $I_s = 20\ A$ computed using (4.30) and total torque in a regular IPMSM for the same magnet and reluctance torques.

4.5.4 Torque Measurement

One of the differences between a conventional IPMSM model and the shifted IPMSM model developed in section 4.3 is the torque equation. In order to validate the developed mathematical model, this paper also presents a comparison of the torque angle curves computed from the model and the experimentally measured torque angle curves.

The mathematical model of the shifted IPMSM represented by (4.28)–(4.30) is used to compute the torque produced by the test motor at various current magnitudes and angles. The magnet flux linkage, ψ_m, the stator resistance, r_s, and the inductances, L_s and L_Δ required by the model are obtained from the measurements performed on the prototyped motor. Based on the measured parameters, the magnet torque and reluctance torque components in the prototyped machine are calculated using the developed model. Fig. 4.10 shows the individual torque components and the total torque produced by the machine for the rated current of 20 A. Here, the torque angle is defined as the angle by which the current vector leads the d-axis. The plot also shows the total torque in a fictitious IPMSM having the same magnet and reluctance torque components as the shifted IPMSM. It is clearly seen that the shifted IPMSM have a higher total torque.

Fig. 4.11 presents the torque-angle curves at five different current magnitudes computed from the model. As expected, the electromagnetic torque peaks at the torque angle of $90°$ when i_d is

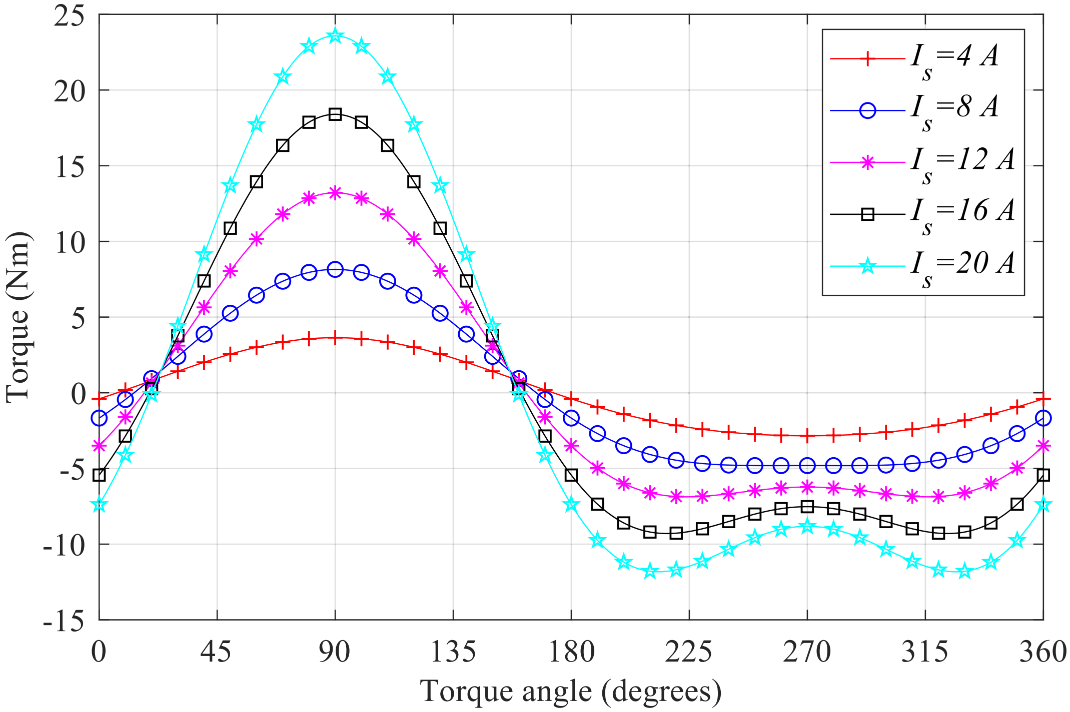

Fig. 4.11: Torque angle curves at various current magnitudes computed using the measured inductances in the developed torque equation presented in (4.30).

zero. Thus, it shows that the magnet and reluctance torques are aligned for positive torque region. However, due to the phase shift in the reluctance torque, it is seen that the magnet and reluctance torques are out of phase in the negative torque region. Thus, the machine produces higher torque in forward motoring mode and lower torque in forward generating (or braking) mode. In contrast, the machine produces lower torque in reverse motoring mode and higher torque in reverse generating mode. In transportation applications, forward motoring and braking modes of operations are of interest. Although the forward braking torque is lower in the shifted IPMSMs, a higher torque can be generated by supplying higher currents than the rated for short periods during braking. Based on the torque curves at different current magnitudes, it is seen that the magnitude of the reluctance torque is negligible compared to the magnet torque at lower current magnitudes. For higher current magnitudes, the reluctance torque varies with the square in the current and becomes comparable to the magnet torque.

In order to measure the torque-angle curve of the prototyped motor, a test setup capable of supplying electrical power to the test motor and extracting the shaft power from the test motor is required. The test setup in Fig. 4.5 depicts some components of the overall test setup. Schematics of the complete test setup is shown in Fig. 4.12. It shows a full four quadrant motor and dynamometer coupled together with a torque transducer. A programmable power supply (MX30-3pi) is used as a DC power supply to the VSI (Semikron Semiteach) DC link. The three phase outputs of the VSI

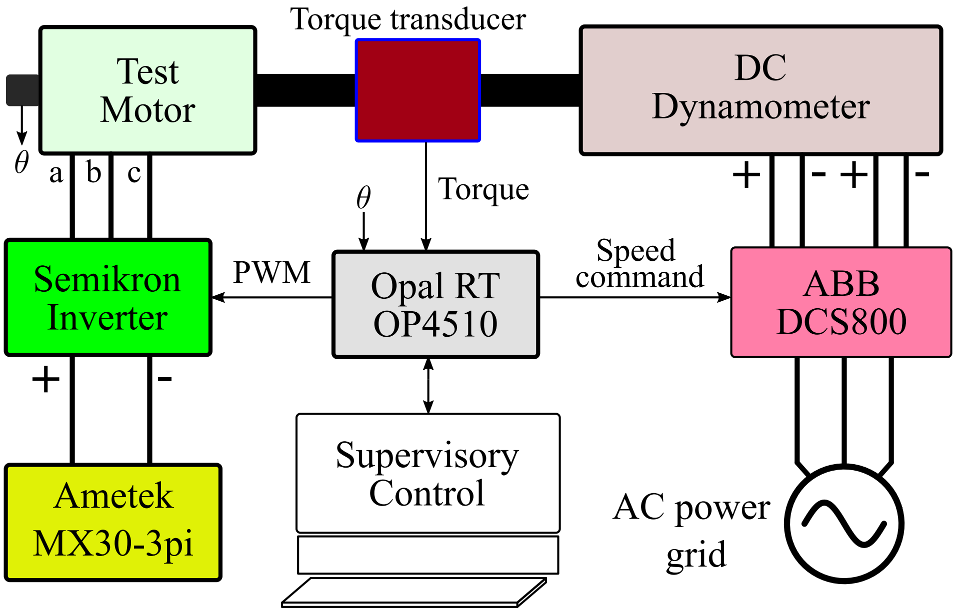

Fig. 4.12: Schematics of the test setup to measure the torque-angle and torque-speed curves of the test machine.

are connected to the terminals of the wye connected test motor. Since the power supply can both supply and sink power, the VSI can be operated to have a bidirectional power flow. Since the VSI can generate any voltage vector (limited by the DC link voltage), the test motor can be operated in all four quadrants. On the dynamometer, an ABB DCS800 is used to control the dc motor in four quadrant modes of operation. An OPAL-RT Op4510 control and prototyping real time system is used to control both the dc and AC drives. A host PC is used to monitor all the system variables and command the real time system. The shaft torque is measured using a torque-meter (MCRT®2903T).

The overall control strategy of the system is to control the shaft speed from the dc dynamometer and torque from the test motor. The inverter dc link is charged to the rated voltage before the motor is started. This will keep the anti parallel diodes reverse biased when the dc motor is started. The controller commands the dc drive to run at a fixed speed and PWM signals are applied to the AC drive inverter. Throughout the test for the torque angle curves, the dc drive maintains a constant shaft speed. Fig. 4.13 shows the schematics of the control strategy to control the test motor. The reference to the controller are the current magnitude, i_s and torque angle, δ. The measured currents are transformed to the dq domain using the rotor position measured by a position encoder. Error signals are then passed through PI controllers to generate PWM signals. The control strategy makes sure that the stator current and torque angle are controlled to the desired references.

Although the test motor is a new type of motor with a different torque characteristic compared to the conventional IPMSMs, and the qd flux linkages are coupled to both i_q and i_d in the developed

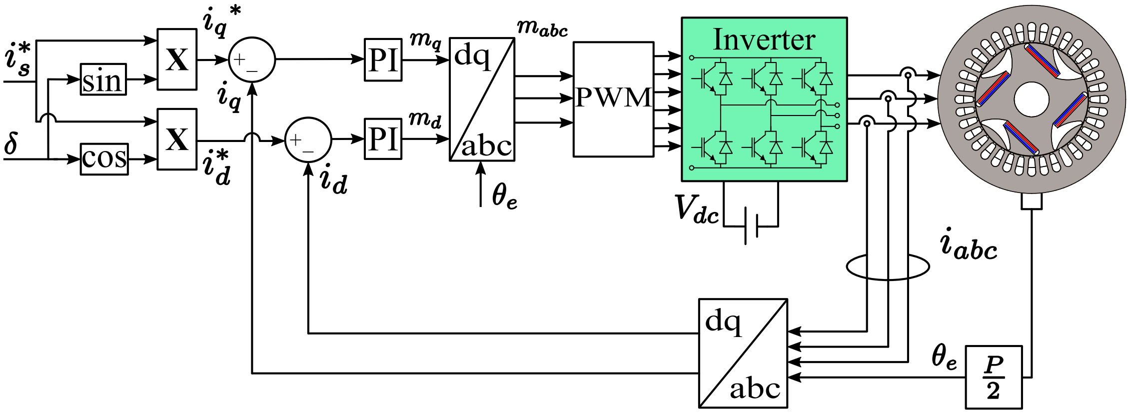

Fig. 4.13: Schematics of the control strategy to measure the torque-angle and torque-speed curves of the test machine.

mathematical model, this particular test does not require any specific attention in the control design. The only requirement in the control design for this test is to maintain the stator current to a desired magnitude and angle at steady state, without much attention to the dynamic performance. Since the dynamometer controls the shaft speed, any torque transient during change in the reference to the test motor will be absorbed by the dynamometer. In order to design the current controllers, the procedure presented in [58] is followed. For the model with reference frame d-axis aligned with the rotor d-axis, the dq inductances are equal to L_s. Thus, the open loop transfer function for both d- and q-axes controllers are same, and it is as follows.

$$G_p(s) = \frac{V_{dc}/2}{T_d s + 1} \frac{1/r_s}{\frac{L_s}{r_s} s + 1} \frac{1}{T_f s + 1} \tag{4.47}$$

where V_{dc} is the inverter dc link voltage, T_d is the time constant of the inverter when modeled as a first order delay and T_f is the filter time constant in the current feedback system. The machine parameters, L_s and r_s are measured in section 4.5.3. For the experimental test, V_{dc} is 350 V, T_d is 62.5 μs, corresponding to the switching frequency of 8 kHz, L_s is 16.5 mH, r_s is 0.22 Ω and T_f is 80 μs, corresponding to the first order filter at 2 kHz. The Sisotool in MATLAB is used to tune the controller gains. The location of the controller zero is selected to cancel the plant pole due to machine resistance and inductance. An integrator is added to the controller, and the gain is selected to have a controller bandwidth of 100 Hz. Since there is no outer control loop, the selected bandwidth is sufficient. With this procedure, the obtained proportional and integral gain values are 0.0594 and 0.792 respectively.

The test motor is operated at different current magnitudes and torque angles. At each operating point, the shaft torque is measured and recorded. Fig. 4.14 presents the torque angle curves measured at five different current magnitudes when the motor is run at a speed of 600 rpm. It

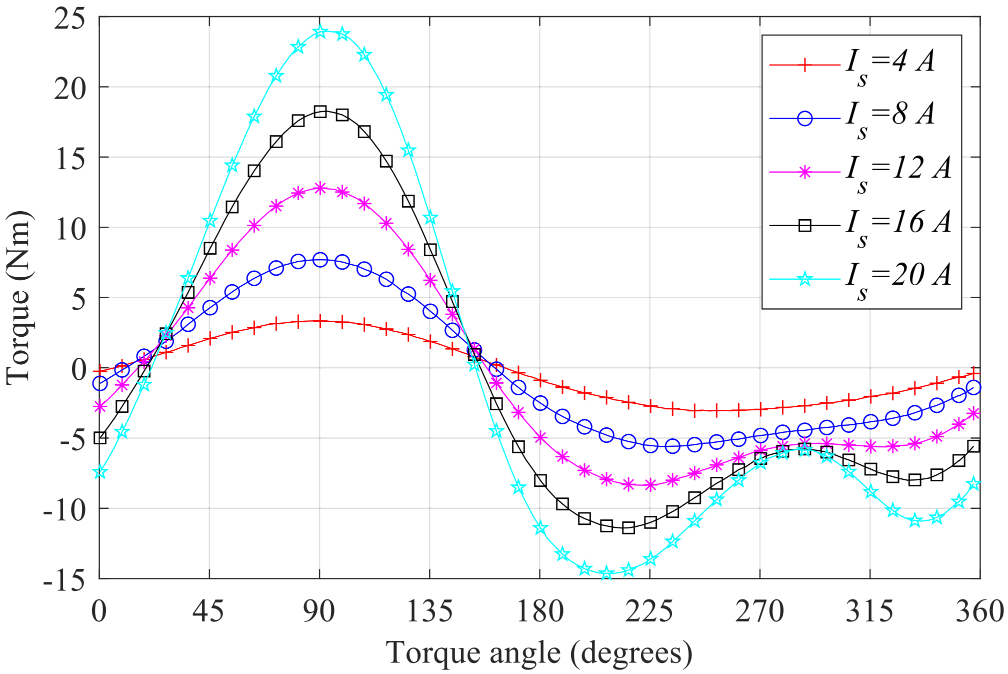

Fig. 4.14: Torque angle curves at various current magnitudes obtained by direct measurement when the motor is run at 600 rpm.

shows a similar characteristic to the one obtained from the mathematical model. A comparison of the measured torque-angle curves with the torque-angle curves obtained from the model for three different magnitudes of current are shown in Fig. 4.15. Although the torque curves for positive torque region is much closer to the computed ones, the deviation is higher for negative torque region. For the measured torque angle curves, the positive torque peaks at $\delta = 90°$ for lower currents, while it deviates slightly ($T = 23.92$ Nm at $\delta = 90°$ and $T_{peak} = 23.95$ Nm at $\delta = 93°$) at the rated current. In the negative torque region, while the calculated torque angle curves are symmetric about $\delta = 270°$, the measured torque angle curves are non-symmetric. In fact the measured torque for δ between $180°$ and $225°$ is higher compared to the calculated torque. Such a non-symmetric nature is caused by the first harmonic inductances that were neglected in the developed mathematical model. In the shifted IPMSM design, the first harmonic inductances are present due to core saturation and assymetric rotor design. A well designed IPMSM will have negligible first harmonic inductances. In such a case, the experimental and computed torque angle curves would match to a greater extent.

4.5.5 Torque-Speed Curve Measurement

The mathematical model presented in (4.28)-(4.30) is used to compute and generate torque-speed and power-speed curves of the prototyped motor. In the algorithm to generate these curves, current and voltage constraints are applied based on the machine rating. An experiment is also

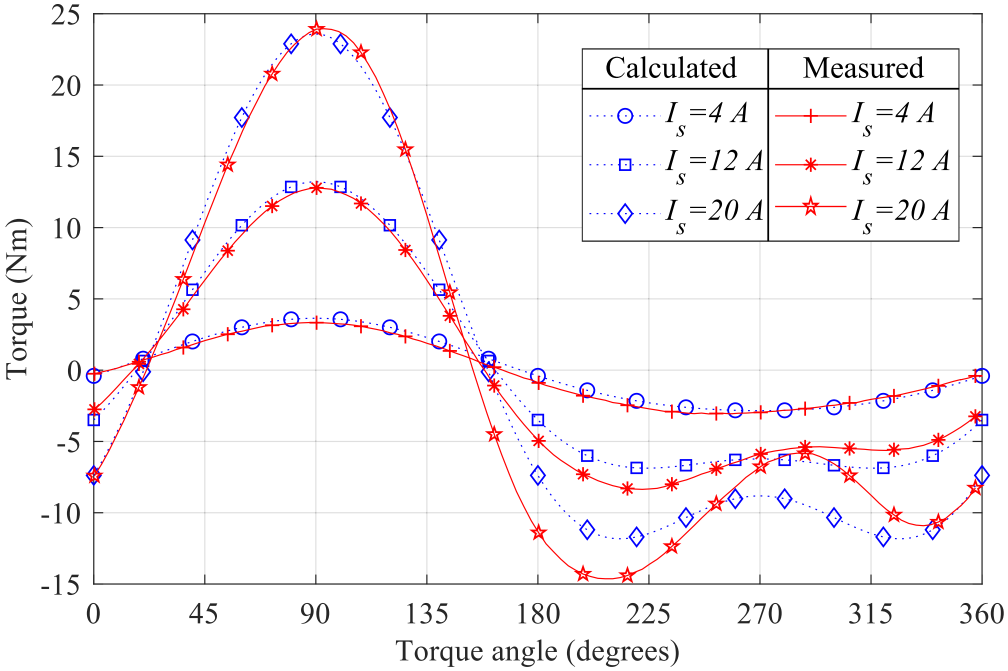

Fig. 4.15: Comparison of torque angle curves calculated from the developed model using the measured parameters with the directly measured torque angle curves.

performed to obtain the actual torque-speed and power-speed curves. The same experimental setup and control algorithm used in torque-angle measurement is used for torque-speed measurement. In the experiment, the dc motor controls the speed and the ac motor is operated in current control mode. The current magnitude and angle are kept constant at the maximum torque per ampere point until the base speed is reached. Thereafter, the torque angle δ is increased to apply field weakening current so that the terminal voltage is maintained constant at the rated value for higher speeds.

Fig. 4.16 presents a comparison of experimental and calculated torque-speed and power-speed curves for motoring mode of operation in positive direction of rotation. The figure shows that there is a close match between the experimental and calculated data below the base speed. For higher speeds, the model predicts higher torque and power. The computed torque and power are electromagnetic torque and power while the measured ones are shaft torque and power. The developed mathematical model does not consider core losses, frictional and windage losses. Core losses can be incorporated in the mathematical model as described in [114]. Frictional and windage losses can be modeled in the mechanical model and subtracted from the electromagnetic torque and power to obtain the shaft torque and power.

Finally, Fig. 4.17 presents a comparison of the experimentally obtained torque-speed and power-speed curves for motoring and braking modes of operation. The plot shows that the maximum braking torque is almost 60% of the motoring torque for lower speeds. However, the motoring

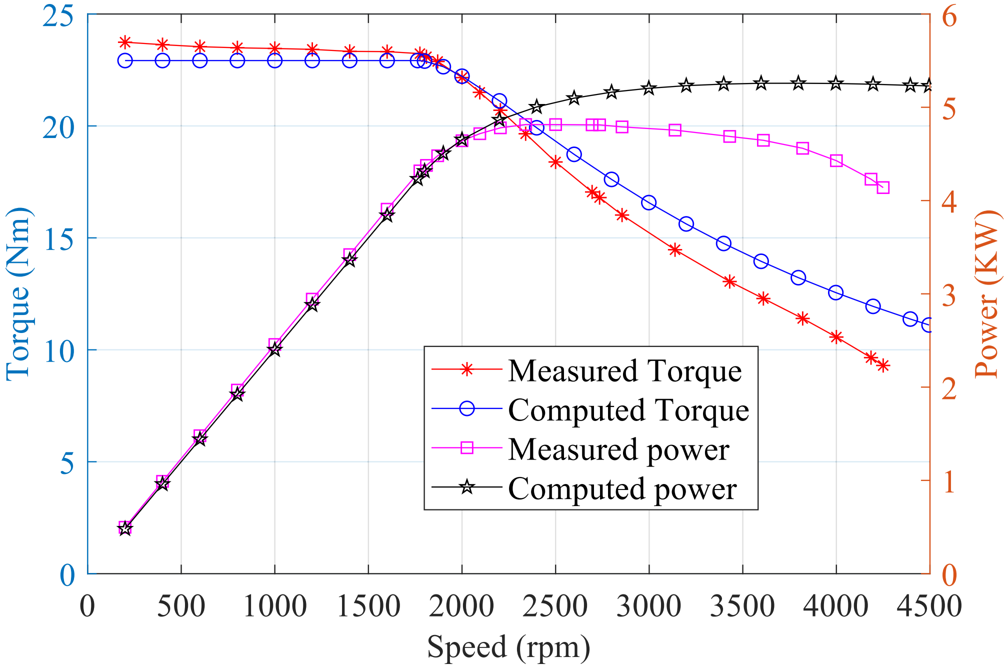

Fig. 4.16: Comparison of the measured torque-speed curve and power speed curve with the ones obtained from the model.

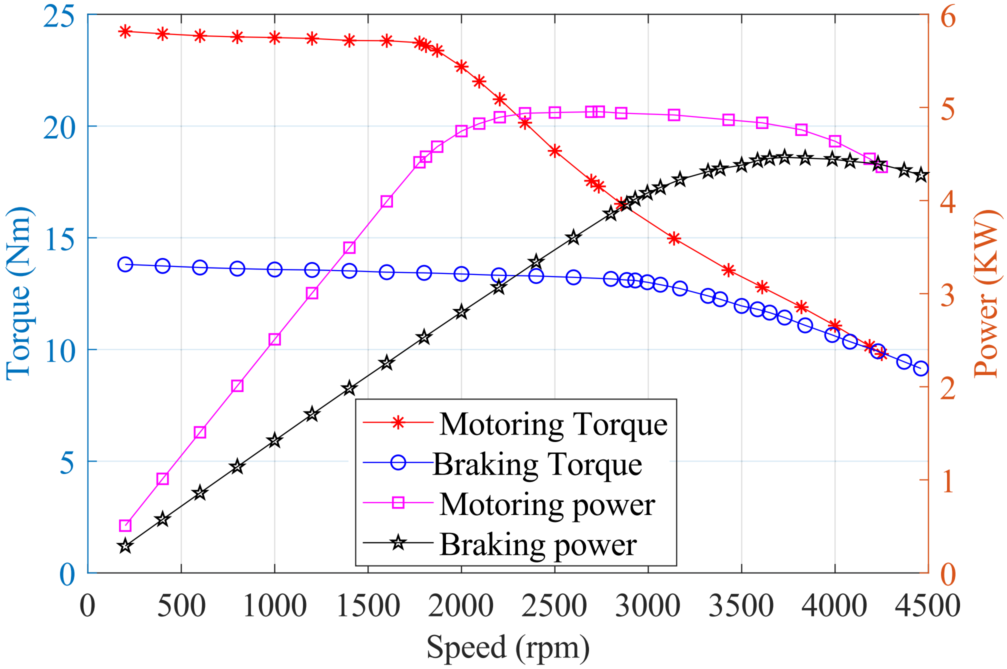

Fig. 4.17: Comparison of the measured torque-speed and power speed curves for motoring and braking modes of operations at the rated current. (Note: the braking mode torque and power are negative, but shown positive in the plot for clearer comparison)

and braking torques are similar for higher speeds of operations. While comparing the power speed

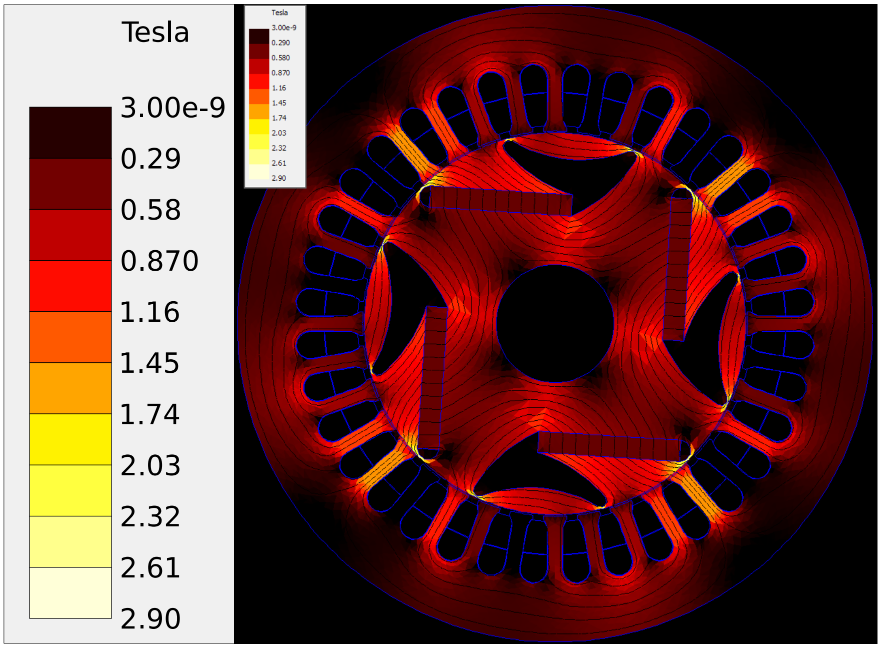

Fig. 4.18: FEA Simulated field distribution at the rated current.

curves, it is seen that the maximum power for braking mode of operation is close to 90% of the motoring mode maximum power. However, it is to be noted that the motoring mode has a wider constant power range than the braking mode.

4.6 FEA Simulation and Characterization

Recently, the FEA simulation has become an integrated part of machine and drive testing systems. Applications such as power hardware in the loop emulation requiring a detailed motor model considering the geometric variation and magnetic saturation uses the parameters obtained from a FEA software [72]. In such applications, the FEA generated flux linkages and inductances are used to represent the actual machine. In order to use such models representing special and novel machines, it is necessary to validate the model generated by FEA. Since the shifted IPMSM is a new class of machine having unsymmetrical rotor, parts of the motor is susceptible to saturation that leads to modeling error using FEA. This section presents the characterization of the test motor with the FEA model.

In order to obtain the FEA simulation results, the designed machine is modeled in MagneForce FEA software. Fig. 4.18 shows the simulated flux density distribution of the machine at the rated current (20A peak). It shows that the tooth flux density reach a flux density of $1.74\ T$, and the flux density near the air-gap in the barrier openings reaches more than $2\ T$. Thus, it is customary to

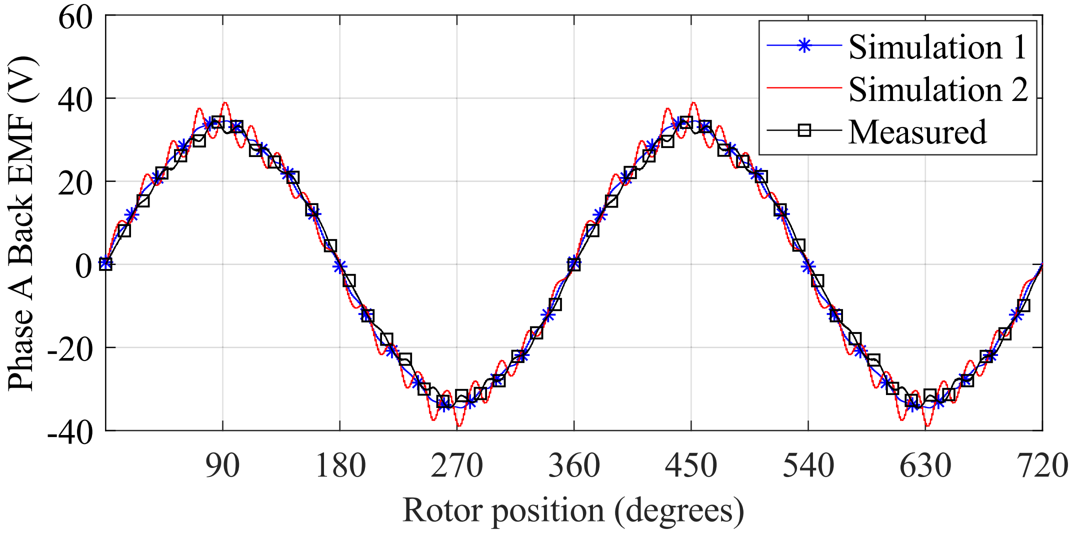

Fig. 4.19: Comparison of measured back EMF at 600 rpm with FEA simulation in MagneForce (Simulation 1 and 2 are stator skewing by 1 slot and 0.75 slot respectively.).

validate the FEA results with experimental results for its use in various applications. This thesis presents the back-emf, inductance, and torque characterization of the shifted IPMSM obtained in BLDC simulation environment in MagneForce software.

4.6.1 Back EMF Characterization

In an ideal sinusoidal machine, the back EMF is sinusoidal with no harmonics. Due to the non-sinusoidal winding distribution, non-sinusoidal air-gap flux and the presence of stator teeth, harmonics exists in the back-EMF. In order to reduce the harmonic voltages, the prototyped machine is designed to have a 8/9 short pitched winding and the stator is skewed by one slot. Since the back EMF plays a vital role in the waveform of the current drawn by the machine, and it directly affects the torque-ripple of the machine, the back EMF characterization is an important aspect of machine characterization.

In section 4.5.2, the experimental measurement of back EMF and magnetic flux linkage is presented. For back EMF characterization, the prototyped machine is operated in generator mode at 600 rpm, and the per phase machine back EMF is measured and recorded using OPAL-RT 0p4510 card with sampling frequency of 100 kHz. At 600 rpm, the back EMF frequency is 20 Hz. Since the voltage measurement unit used to measure the voltage has a bandwidth of 20 kHz, the harmonic content up to 100^th harmonic in the recorded voltage waveform is retained with no significant loss in magnitude and phase shift. The measured back EMF is plotted in Fig. 4.19.

In order to obtain the machine back EMF using FEA, the machine is modeled and simulated in

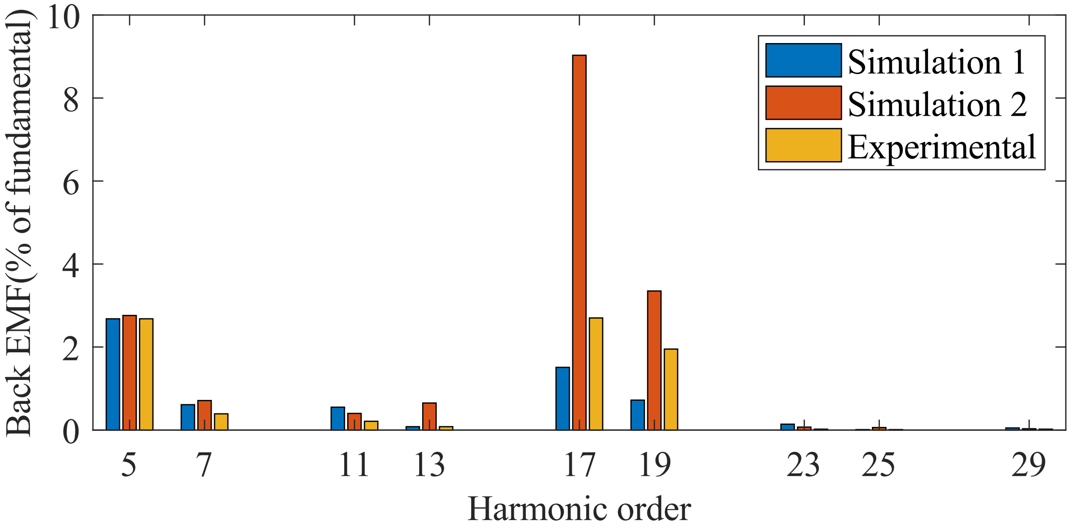

Fig. 4.20: Comparison of measurement and FEA simulated back emf harmonics (Simulation 1 and 2 are stator skewing by 1 slot and 0.75 slot respectively.).

BLDC simulation environment in MagneForce. The open circuited back EMF from MagneForce for one stator slot skew is shown in Fig. 4.19. Compared to the back EMF waveform from MagneForce for one stator slot skewing, the measured back EMF shows higher ripple content. Due to this, the designed machine is simulated again with a stator skewing of 0.75 slots. Fig. 4.19 compares the measured back EMF with simulated back EMFs for 1 and 0.75 stator slots skewing. It shows that the measured back EMF has higher ripple compared to simulation with 1 slot skew, but lower ripple compared to simulation for 0.75 slot skew. The harmonic content in the measured and simulated back EMFs are presented in Fig. 4.20. Based on this plot, it is seen that the measured back EMF harmonic content is in between the simulated back EMF with stator skewing of one slot and 0.75 slot. One reason for this might be the imperfections in stator skewing during the motor manufacturing.

4.6.2 Inductance Characterization

In order to characterize the machine inductance, the FEA model is simulated to obtain inductances for two cases of stator skew angle: 1 slot skew and 0.75 slot skew. From MagneForce, rotor position dependent self and mutual inductance terms are obtained. As presented in section 4.5.3, the L_α is obtained from MagneForce. Fig. 4.21 presents the rotor position dependent L_α obtained from MagneForce simulation at the rated current. It shows that there is a very slight difference in the inductance obtained from simulations with 1 stator slot skew and 0.75 stator slot skew. The plot also shows that the inductance has 1^{st} order harmonic opposed to the general assumption that the saliency will introduce 2^{nd} order harmonic and its multiples. This is due to unsymmetrical design with high magnetic saturation. The first order harmonic is more prevalent for lower stator currents.

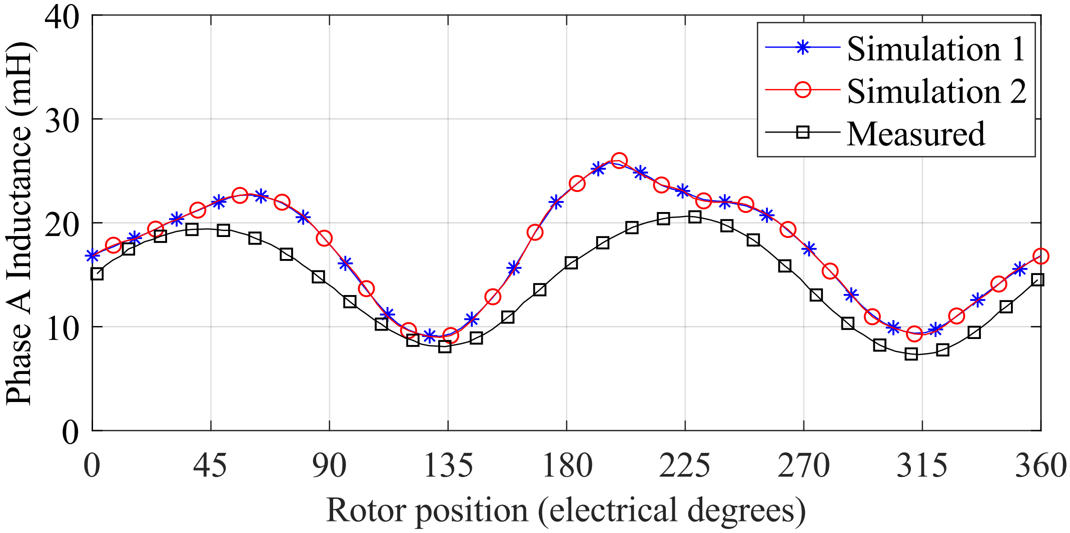

Fig. 4.21: Comparison of measured phase A inductance with FEA simulation (Simulation 1 and 2 are stator skewing by 1 slot and 0.75 slot respectively.).

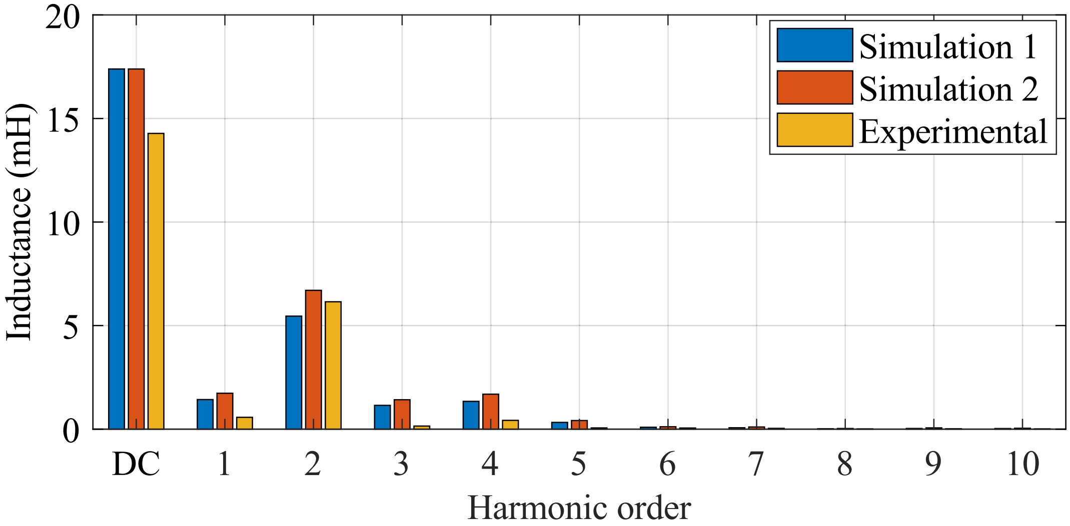

Fig. 4.22: Comparison of measurement and FEA simulated inductance harmonics (Simulation 1 and 2 are stator skewing by 1 slot and 0.75 slot respectively.).

Fig. 4.21 also presents a comparison of measured and simulated inductance variation with the rotor position. The plot shows that the experimentally measured inductance is slightly lower than the simulation.

In order to compare the harmonic inductances, FFT analysis is performed on the simulated inductances. Fig. 4.22 compares the harmonic contents of the simulated and experimental inductances at the rated current. The plot shows that the simulated inductance harmonic content for one stator slot skew and 0.75 stator slot skew has negligible difference. Comparing the measured and simulated inductance harmonic content, while the experimentally obtained inductance has

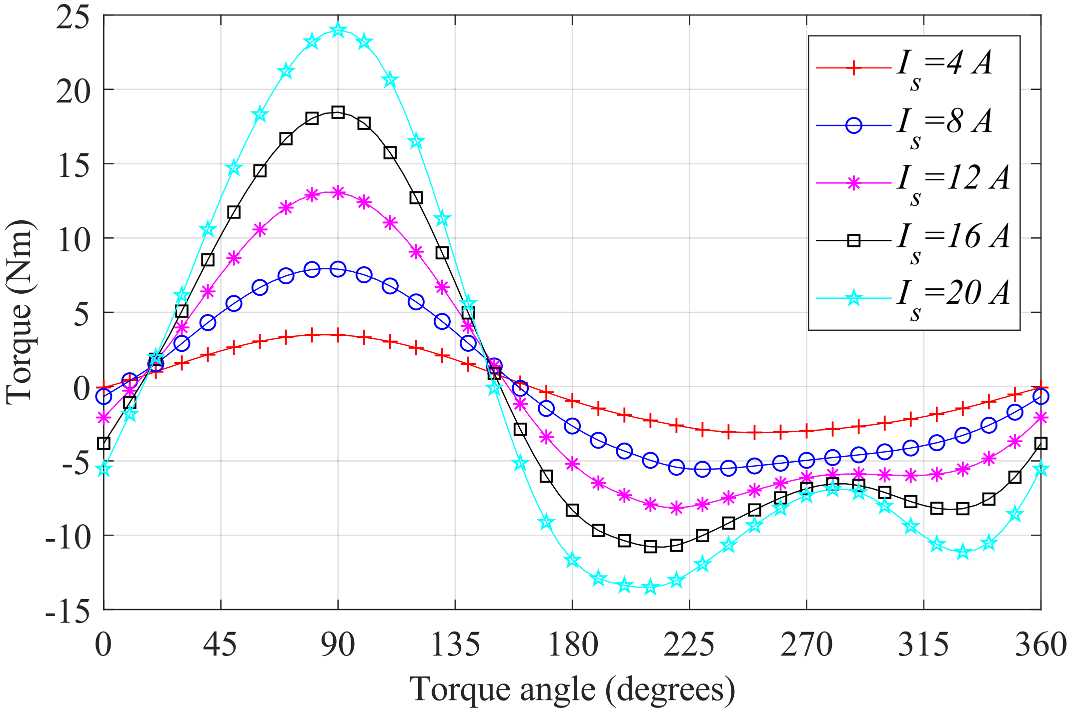

Fig. 4.23: FEA Simulated torque angle curves of the machine.

lower average inductance, the measured second harmonic inductances are almost the same. One reason for the deviation in the average inductance might be due to the imperfect model of the exact physical nature of the electrical steel. However, the harmonic inductance is mainly due to geometric variations, and thus it is less affected by the modeling error in physical nature of the steel. Due to the unsymmetrical design, the core above the flux barrier near the rotor surface is heavily saturated. The saturation characteristics of the steel used as the core material is not available for deep saturation region. This is the reason for the phase shift in the experimentally obtained torque characteristics at higher currents.

4.6.3 Torque Characterization

For torque characterization of the shifted IPMSM, the FEA model in MagneForce is simulated to obtain the torque characteristics of the machine. Simulations are run for various current magnitudes and angles. For each current magnitude and angle, the motor is simulated to run at 600 rpm, and the average torque over the rotor positions extending a complete rotation is recorded. Fig. 4.23 presents the simulated torque angle curve obtained from the MagneForce simulation. It shows that the simulated torque has a similar characteristic as the measured torque in Fig. 4.14. A comparison of the simulated and measured torque characteristic for three magnitudes of current is presented in Fig. 4.24. It is seen that the simulated peak torque magnitudes are almost equal to the measured

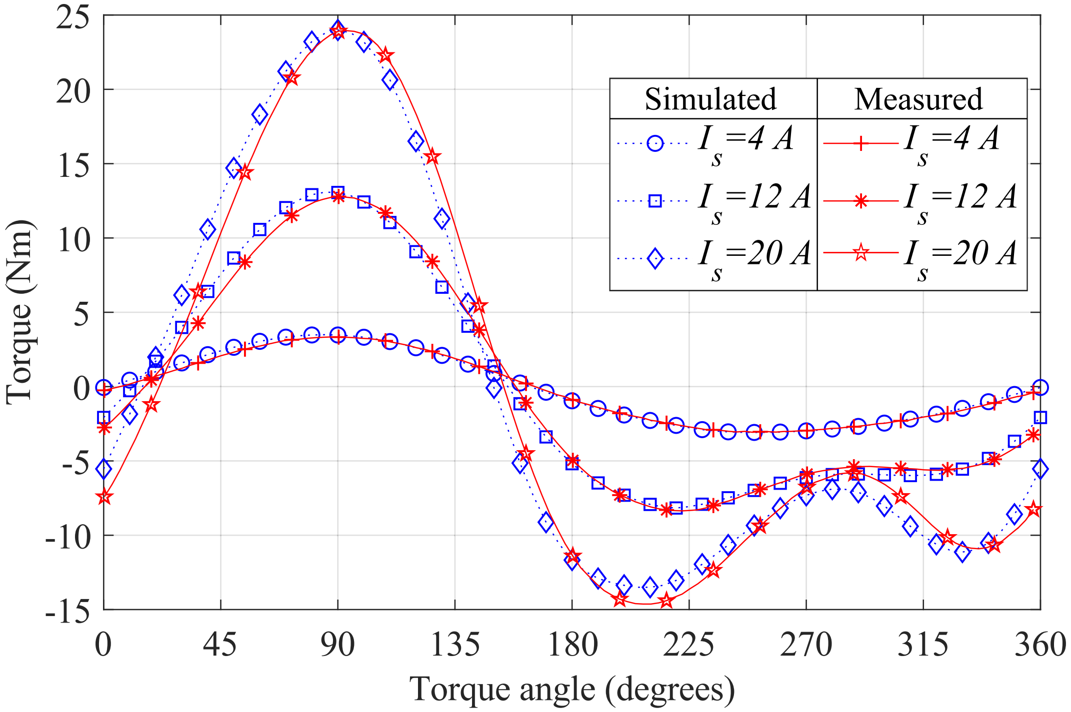

Fig. 4.24: Comparison of FEA simulated and experimentally measured torque angle curves.

peak torque in positive torque region. In the negative torque region, the measured peak torque is higher at the rated current. For lower currents, the simulated torque angle curves are almost in phase with the measured torque angle curve. However, there is a phase shift in the measured torque angle curve for higher currents.

4.7 Summary

This chapter presented a mathematical model of a novel (IPMSM) with aligned magnet and reluctance torques. It is a new class of IPMSM, a viable alternative design for transportation applications, where the flux barrier is modified in such a way that the relative positions of the magnet and reluctance axes shift from their regular position. The shift angle between the magnet and reluctance axes is such that both the magnet and reluctance torques have their peaks at the same torque angle, increasing the motor torque density. Due to the shift in the torque axes, the existing mathematical model for a regular IPMSM is not applicable in its present form. This chapter developed a mathematical model for the shifted IPMSM so that quantitative behavior of each variable in the system can be studied.

In order to validate the developed mathematical model, a motor is prototyped to perform experimental tests. Since the existing method to find the d-axis of the regular IPMSM does not apply to the shifted design, this chapter presented in detail a technique to find the rotor d-axis position. In order to obtain the parameters in the developed mathematical model, the prototyped motor is tested for its inductance, resistance and magnet flux linkage. The measured parameters are used in the mathematical model to obtain the torque-angle, torque-speed and power-speed curves of the prototyped motor. Experimental tests are performed to obtain the actual steady state torque and power characteristics. The comparison of the computed and the measured torque and power characteristics validates the usefulness of the developed mathematical model.

This chapter also presented the characterization of the novel shifted IPMSM with a FEA software. The back EMF, inductance and torque angle curves of the test motor is obtained from MagneForce software, and a comparative study is presented. It showed that the actual back EMF, inductance and torque angle curves deviates from the actual measured quantities. The deviations show the effect of manufacturing tolerances and modeling inaccuracy of the physical nature of the materials used.

Based on the work presented in this chapter, the following research paper is published [115].

- R. Thike and P. Pillay, ”Mathematical Model of an Interior PMSM With Aligned Magnet and Reluctance Torques,” in IEEE Transactions on Transportation Electrification, vol. 6, no. 2, pp. 647-658, June 2020, doi: 10.1109/TTE.2020.2991369.

Chapter 5

Parameter Measurements and Modeling of a Novel Hybrid Variable Flux Machine

As already discussed in chapter 1, high accuracy machine emulations require a highly accurate behavioral model of an electric machine. With the advent of modern design and manufacturing technologies, new and novel electric machine designs are evolving. Electric machines for EV and HEV applications must have wide speed range and high efficiency in the entire operating region. VFMs possess both of these properties, and are considered an alternative to the conventional IPMSMs. This chapter present the parameter measurements of a novel hybrid VFM with series rare-earth and AlNiCo magnets. A current control based method is used to measure the machine flux linkages and inductances including cross-saturation at different magnetization states. The same current controller is used to obtain the magnetization and demagnetization characteristics of the test VFM. Based on the experimentally measured magnetization curves and flux linkages, a look-up table based model of the prototyped VFM is built in MATLAB Simulink considering the conditions that affect the magnetization state, which is useful for machine emulation applications. The developed model is validated with experimental test results for steady state and transient operations.

5.1 Background

PMSMs require an additional field weakening armature current continuously for their operations above base speed. This additional current increases the copper losses as well as drive system losses. In addition, the field weakening current limits the torque producing current component, thereby narrowing the torque speed range of the motor [7]. In order to eliminate the field weakening current, various VFM designs are proposed [42, 47, 48, 50, 52, 108, 116]. In variable flux machines (VFMs), low coercive force magnets such as AlNiCo are used instead of rare-earth magnets, where the magnet flux is controlled by a short pulse of d-axis current [65]. For extended speed operation, demagnetizing d-axis current pulses are applied to lower the magnet flux, eliminating the continuous flux weakening current.

When low coercive field magnets are used, the magnets are susceptible to unintentional demagnetization by the armature current. The main issue with the AlNiCo based VFM is the partial loss of magnetization with the q-axis current. One solution to overcome this issue is to increase the thickness of the magnet. However, it increases the magnetization current of the machine, and thus the inverter rating increases. Other issues with the AlNiCo based VFMs are the reduced power capability at high speeds and higher torque ripple due to its design. In order to overcome these shortcomings, machine topologies utilizing both rare-earth and AlNiCo magnets in series and parallel combinations to form a motor pole are presented in [109, 117]. An alternative design utilizing a small thickness of rare earth magnet in series with the low coercive field AlNiCo magnets is presented in [57]. In this design, the magnetic field produced by the two types of magnets are in series, and hence called the series hybrid VFM.

This chapter presents the measurement of flux linkages and magnetization characteristics of a novel hybrid VFM with series rare-earth and AlNiCo magnets presented in [57]. It also develops a machine model based on the measured flux linkages and magnetization characteristics for power hardware-in-the-loop (PHIL) simulations commonly known as machine emulation. It is a testing methodology of an electric drive system. An accurate machine emulation system should have details on the machine's magnetic characteristics considering variation of machine geometric and magnetic data [58, 118]. In VFMs, there exists one more variable that affects the magnetic behavior of the machine. Since the magnet flux can be varied in real time in VFMs, inclusion of magnet flux variation with respect to the stator current and the variation of the stator flux linkage with the magnet flux in the machine model is necessary.

In order to develop a detailed look-up table based model of a VFM for PHIL applications using the experimentally measured data, a fast and accurate parameter measurement method is required. Rotational tests as presented in [66] produce accurate machine inductances, but averaged over the rotor positions. Traditional DC standstill and AC standstill tests are limited to the measurement of inductances without considering cross-saturation effects. A voltage pulse based standstill method as presented in [64] is efficient to measure position dependent machine inductances including cross-saturation effects. However, it requires an offline processing of the measured signals. A novel current control standstill method to automate the flux linkage measurement is presented in [80]. In [73, 119, 120], a self-commissioning and self identification method to obtain the machine parameters without locking the rotor is presented. However, the magnetization state in the VFM is affected by the d-axis current. Therefore, these methods need modifications in order to be applied to VFMs.

This chapter uses the current control method presented in 2 to measure the machine flux linkage and magnetization characteristics. In this method, the VFM rotor is locked to a fixed position, and stator currents in the qd reference frame are applied in a controlled manner. The current in the axis of measurement is applied in a pulsed form while the current in the quadrature axis is maintained constant. The change in magnetization state of the magnets is avoided during the measurement procedure by avoiding the d-axis current that can cause change in the magnetization. Finally, the experimentally measured flux linkage and magnetization characteristics are used to model the hybrid VFM with series rare-earth and AlNiCo magnets for machine emulation applications, and the developed model is validated using the transient response of the prototyped motor.

5.2 Test VFM and its Model

The test VFM is a hybrid VFM using series rare-earth and AlNiCo magnets in the rotor to produce the air-gap flux. Table 5.1 presents the design details of the test VFM. It is a six pole inverter driven motor designed for 600 volt dc link. It has a single layer distributed winding with stator skewed by 1 slot pitch (10^o mechanical). Normally, AlNiCo based VFMs are designed with unskewed stator to eschew the uneven magnet demagnetization. However, with a small thickness of rare-earth magnets on the top of the AlNiCo magnets, the uneven stator flux due to the stator currents has no effect on the magnetization state of AlNiCo magnets. The test motor is designed for 59% demagnetization at twice the rated motor current.

Fig. 5.1 presents a section of the test VFM geometry. The rotor is a V-shaped design having two pieces of magnets forming a magnetic pole. Each piece of the magnet consists of a thinner rare-earth magnet placed on the top of the AlNiCo magnet. Dynamics of the VFM in the standard dq reference frame with flux linkages as state variables are given by (5.1) and (5.2).

$$v_d = R_s i_d + \frac{d\lambda_d}{dt} - \omega_r \lambda_q \tag{5.1}$$

$$v_q = R_s i_q + \frac{d\lambda_q}{dt} + \omega_r \lambda_d \tag{5.2}$$

where v_d, v_q and i_d, i_q are the dq voltages and currents, R_s is the stator phase resistance, ω_r is the rotor electrical speed, λ_d and λ_q are the dq flux linkages. The d-axis flux linkage, λ_d is the sum of

Table 5.1: Specification of the VFM under test.

Machine Type	3 phase Y connected
Rated Power	10 hp
Rated Peak Current	17 A
Rated Voltage	415 V
Number of Poles	6
Peak Torque	45 Nm
Stator Outer Diameter	180 mm
Rotor Outer Diameter	108 mm
Air-gap length	0.5 mm
Stack length	125 mm
Number of Stator Slots	36
Number of turns per coil	23
Winding configuration	5/6 distributed
Rated magnet flux linkage	0.31 V.s
Demagnetization current	34 A
Demagnetization level	59% with 2x I$_{rated}$

magnet flux linkage (λ_m) and the flux linkage due to stator d-axis current (λ_{ds}) as shown in (5.3).

$$\lambda_d = \lambda_{ds} + \lambda_m \tag{5.3}$$

Since the magnet flux can be varied by the d-axis current, it depends on the magnitude and polarity of i_d. It is represented mathematically as follows.

$$\lambda_m = \begin{cases} \mathcal{F}(i_d), & for\ i_d \geq 0\ \&\ \mathcal{F}(i_d) > \lambda_{m0} \\ \lambda_{m0} & for\ i_d > 0\ \&\ \mathcal{F}(i_d) < \lambda_{m0} \\ \lambda_{m0} & for\ i_d < 0\ \&\ \mathcal{G}(i_d) > \lambda_{m0} \\ \mathcal{G}(i_d), & for\ i_d < 0\ \&\ \mathcal{G}(i_d) < \lambda_{m0} \end{cases} \tag{5.4}$$

Where, λ_{m0} is the previous value of the magnet flux linkage, $\mathcal{F}$ is the function representing magnetization characteristics, and $\mathcal{G}$ is the function representing demagnetization characteristics. One of the objectives of this chapter is to obtain these functions along with the flux linkage

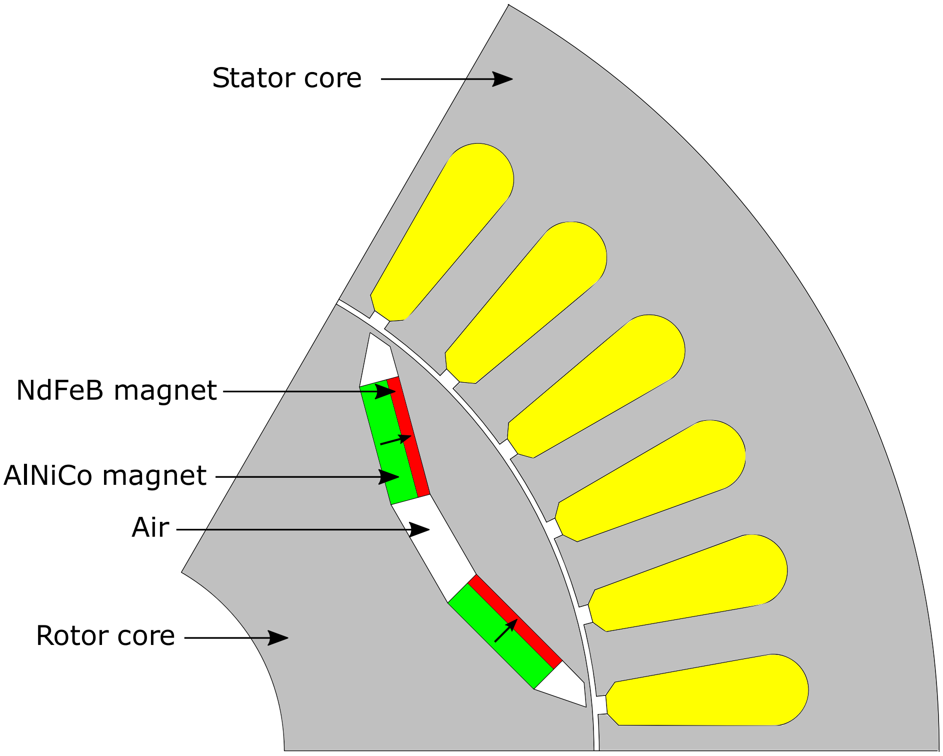

Fig. 5.1: Machine geometry of the VFM under test showing its components.

characteristics of the VFM.

Due to saturation and cross-coupling effects, both the dq flux linkages are functions of dq currents and magnet flux. The dq flux linkages can be expressed as functions of several inductances shown in (5.5) and (5.6).

$$\lambda_d = L_{dd}(i_d, \lambda_m)i_d + L_{dq}(i_d, i_q, \lambda_m)i_q + \lambda_m(i_d) \tag{5.5}$$

$$\lambda_q = L_{qd}(i_d, i_q, \lambda_m)i_d + L_{qq}(i_q, \lambda_m)i_q \tag{5.6}$$

where L_{dd} and L_{qq} are the direct and the quadrature axis self inductances, L_{dq} and L_{qd} are the direct and quadrature axis cross-coupling inductances.

In a motor drive system with voltage input and current as the output, the direct solution of (5.1) and (5.2) for current requires the inductance estimates. Since the inductance is not a continuous function, this chapter solves the dynamic equations for flux linkages. In order to obtain the dq currents from the flux linkages, functions relating the dq currents and flux linkages due to stator currents at different magnetization states are obtained experimentally.

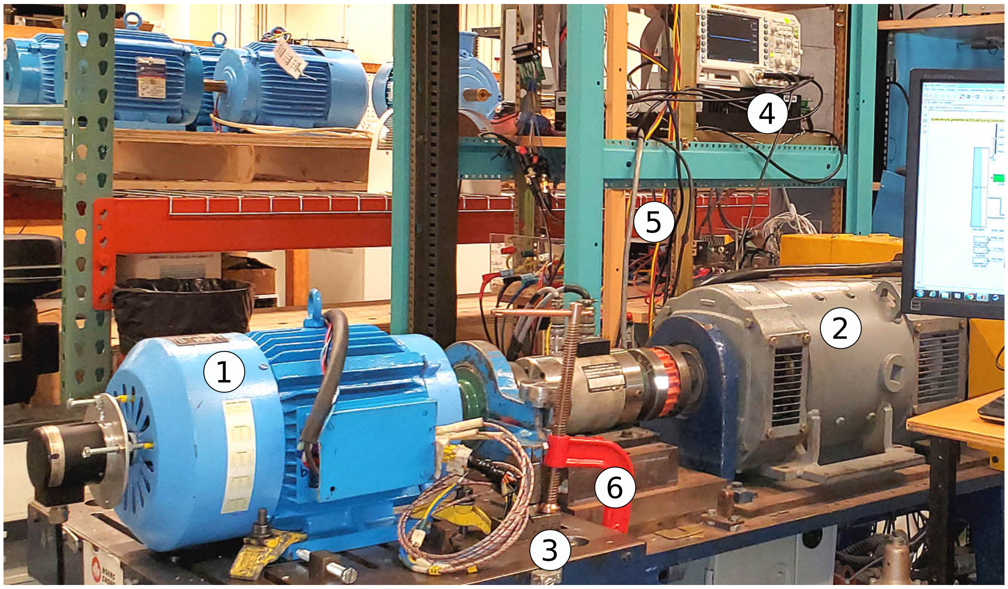

Fig. 5.2: Experimental setup showing 1. Test VFM. 2. DC dynamometer. 3. Adjustable test bench. 4. OPAL-RT OP4510. 5. Voltage and current sensors. 6. Mechanical clamp.

5.3 Experimental Tests and Measurements

5.3.1 Rotor d-axis Location

Unlike regular PMSMs, the test rotor d-axis in special electric machines may not lock to the stator phase A axis when a dc current is supplied to stator phase A with return current flowing equally in B and C phases [115]. For the test VFM , it is experimentally found that the rotor axis along either of the magnets in the rotor pole aligns along the phase A axis when a dc stator current along phase A is applied. Based on Fig. 5.1, the rotor d-axis is in between the magnet pieces in a pole. In order to find the rotor d-axis, the VFM is run as a generator at 600 rpm. The dynamometer setup shown in Fig. 5.2 is used to run the test VFM. The three phase back-emfs are measured and transformed to the dq reference frame online in Opal-RT Op4510 using the following transformation.

$$\left[K_{qd}\right] = \frac{2}{3}\begin{bmatrix}\cos(\theta) & \cos(\theta-\gamma) & \cos(\theta+\gamma)\\ \sin(\theta) & \sin(\theta-\gamma) & \sin(\theta+\gamma)\end{bmatrix} \tag{5.7}$$

$$\begin{bmatrix}v_q\\ v_d\end{bmatrix} = \left[K_{qd}\right]\begin{bmatrix}\sum V_n\cos(n\omega t)\\ \sum V_n\cos(n\omega t-\gamma)\\ \sum V_n\cos(n\omega t+\gamma)\end{bmatrix} \tag{5.8}$$

$$\theta = \theta_{en} + \theta_{sh} \tag{5.9}$$

where, v_q and v_d are qd axes back-emfs, γ is $120°$, θ is the q-axis position from the phase A axis, n is the harmonic order, V_n is the n^{th} order back-emf amplitude, θ_{en} is the rotor position measured by the position encoder, and θ_{sh} is the shift applied to θ_{en}. When θ_{sh} is such that v_d is zero and v_q is V_1, the peak of the fundamental back-emf, θ becomes the position of rotor q-axis from phase A axis. Both v_q and v_d will have harmonics due to measurement offset and back-emf harmonics. Since the fundamental will transform to dc in the qd reference frame, a low-pass filter will remove all the harmonics in v_q and v_d.

5.3.2 Measurement of Magnetization Characteristics

Magnetization characteristics of a VFM shows how the magnet flux varies with the stator d-axis current. The experimental setup shown in Fig. 5.2 is used to measure the magnetization and demagnetization characteristics of the test VFM. First of all, the rotor shaft is locked using a mechanical clamp arrangement. A positive i_d pulse of magnitude 36 A is applied to the machine. The magnet flux is measured by running the VFM as a generator. In order to avoid the offline FFT, the back-emf voltages are converted to the qd reference frame and filtered out to obtain the dc values of v_d and v_q, which are used to obtain the peak magnitude of the fundamental component of the phase back-emf. The magnet flux is computed as the ratio of V_1 and the rotor electrical speed. The measured magnet flux corresponding to $i_d = 36\ A$ is the full magnetization of the motor. The demagnetization characteristics is obtained from the measured V_1 by applying negative i_d pulses to the fully magnetized VFM, increasing its magnitude in each measurement. The maximum magnitude of i_d applied to the machine for demagnetization characteristics is $36\ A$. Fig. 5.3b presents the experimentally obtained demagnetization characteristics of the prototyped VFM. At full magnetization, the measured magnet flux is 0.3096 V.s which reduces to 0.173 V.s at $i_d = -36\ A$. In order to obtain the magnetization characteristics, positive i_d pulses are applied in increasing magnitude to the least magnetized VFM, measuring the magnet flux for each i_d pulse. Fig. 5.3a shows the experimentally obtained magnetization characteristics of the test VFM. The lowest magnetization state has a magnet flux linkage of 0.173 V.s. For $i_d = 36\ A$, the magnet flux increases to 0.3096 V.s. The functions $\mathcal{F}$ and $\mathcal{G}$ defined in (5.4) are obtained from the magnetization and demagnetization characteristics in Fig. 5.3a and 5.3b respectively.

5.3.3 Flux Linkage and Inductance Measurement

VFMs are special compared to regular PMSMs due to change in the magnet flux with i_d. The flux linkage measurement procedure discussed in [73, 119, 120] and other recent publications focusing on auto-tuning and self-commissioning apply bidirectional currents to the test motor. Since the

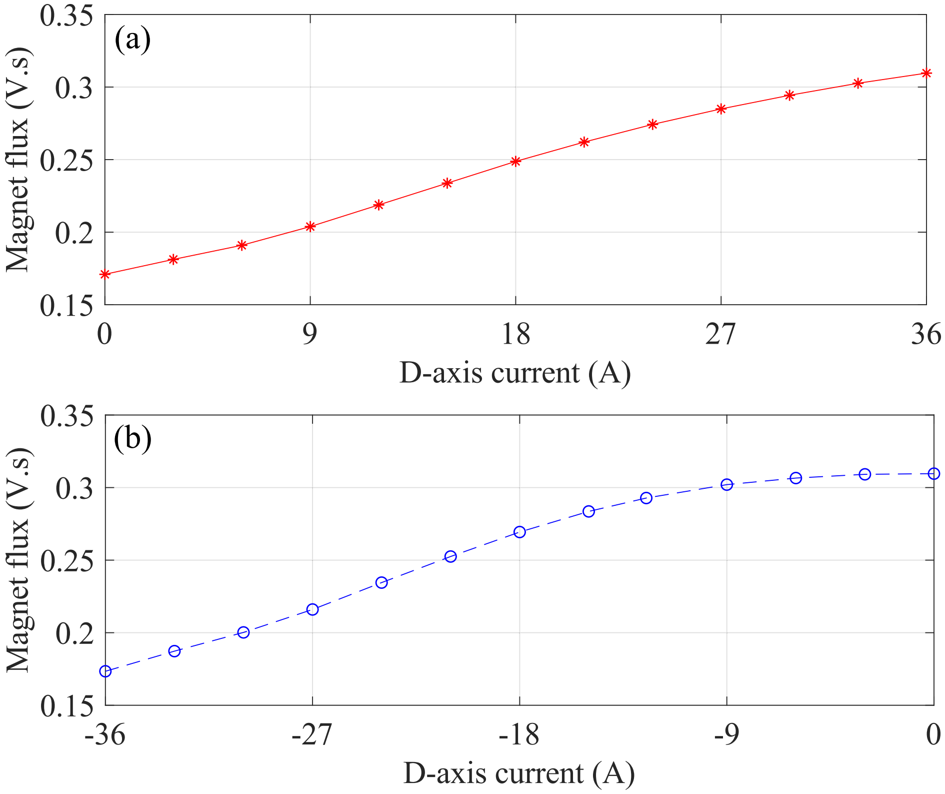

Fig. 5.3: Experimentally obtained magnet flux linkage variation with d-axis current pulse magnitude. (a) Magnetization characteristics. (b). Demagnetization characteristics.

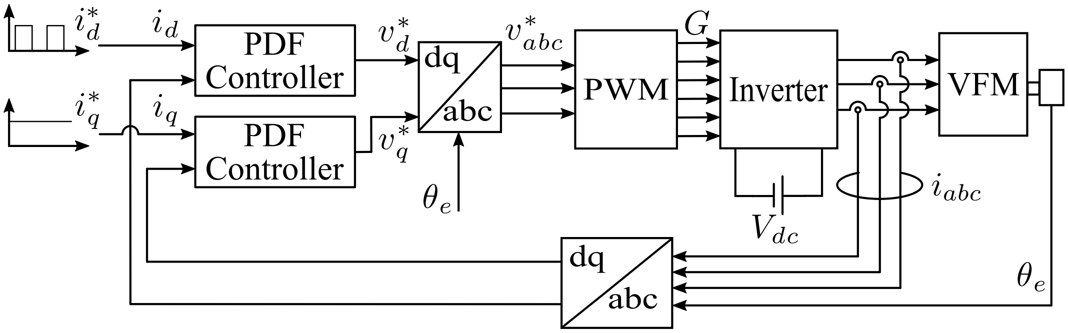

Fig. 5.4: Proposed control structure to measure the VFM flux linkages and inductances at locked rotor condition.

magnet flux in VFMs varies with i_d magnitude and direction, measurement of cross-magnetizing inductances without locking the rotor shaft is challenging. Thus, this thesis uses the locked rotor test to measure the VFM flux linkage and inductance with respect to current.

In order to avoid offline processing, and ensure the magnetization state is unaffected during the measurement, it is proposed to use the automated current control method presented in chapter 2 to measure the VFM flux linkages. Fig. 5.4 presents the schematics of the proposed method to

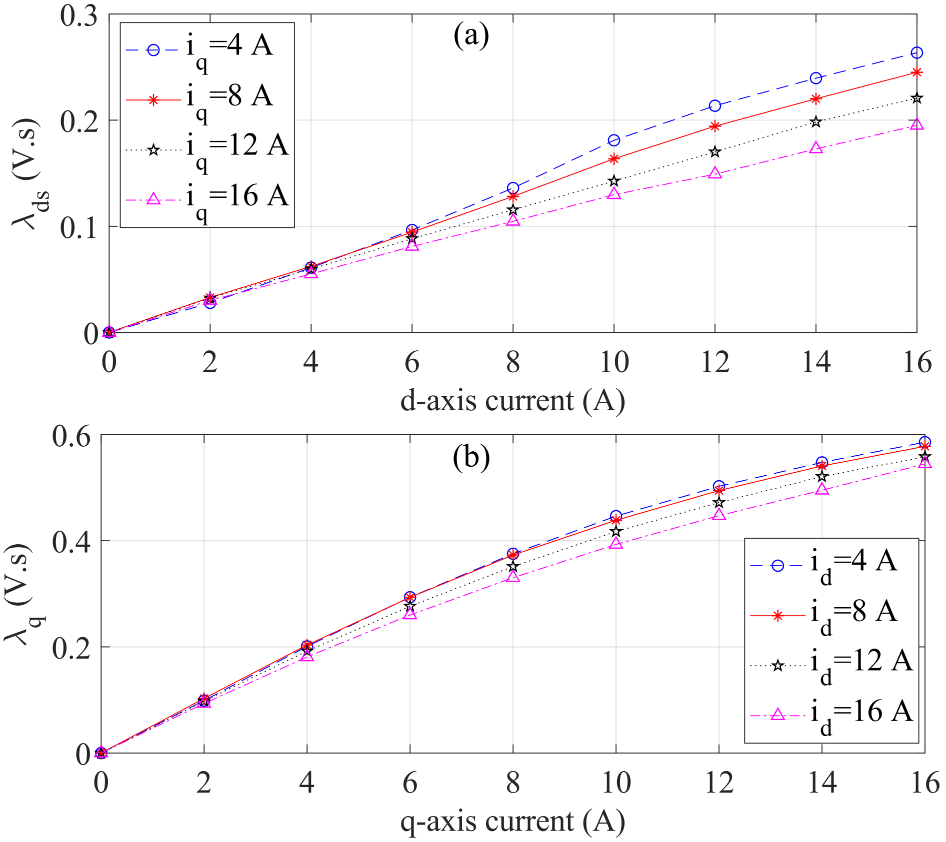

Fig. 5.5: Experimentally measured qd flux linkages. (a) D-axis flux linkage variation with i_d at different i_q magnitudes. (b). Q-axis flux linkage variation with i_q at different i_d magnitudes.

measure the VFM flux linkages. The proposed method requires locking the VFM rotor shaft to a fix position. For the d-axis flux linkage measurement as shown, a d-axis current pulse is applied in closed loop while controlling the q-axis current to a constant. As discussed in chapter 2, an advantage of the proposed technique is that a rough estimate of the machine inductance is enough to design the current controllers. More details on the current controller design to ensure almost similar current response for a wide variation in machine inductance using a rough estimate of inductances to design the controllers are presented in [80]. The controllers are designed to have no overshoot in the response while ensuring a similar response for wide variation in machine inductances. These are essential requirements in VFM flux linkage measurement to avoid the change in magnetization during the measurement process. Although the test VFM is designed for a 600 V dc link, a reduced inverter dc input of 100 V is used in the measurement. It is done to limit the current ripple produced due to switching. For the q-axis flux linkage and inductance measurement, a pulsed q-axis current is applied in closed loop while the d-axis current is maintained constant using the closed loop current controller.

Fig. 5.5 presents the experimentally measured qd flux linkages due to stator excitation at 100%

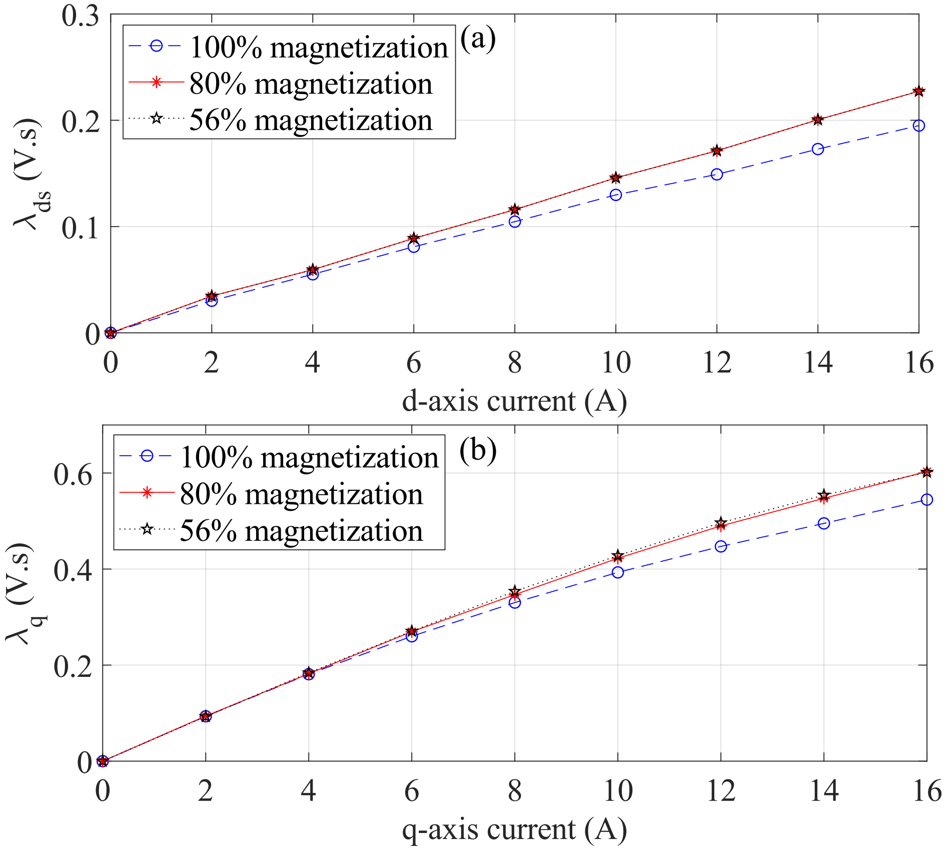

Fig. 5.6: Comparison of experimentally obtained flux linkages at three different magnetization states. (a) D-axis flux linkages due to stator current only at $i_q = 16\ A$. (b). Q-axis flux linkages at $i_d = 16\ A$.

magnetization state of the VFM. Since the proposed technique does not measure the magnet flux component, it is not included in Fig. 5.5a. Based on the plots, it is seen that cross-magnetization effects exist in both qd axes. Based on the rotor geometry, the flux produced by the stator current in the d-axis is smaller due to the presence of the magnet flux compared to the same current in q-axis. Due to higher flux level in the d-axis, the cross-magnetizing effect on it is higher compared to the q-axis.

Since the complete modeling of the VFM requires the flux linkage characteristics at different magnetization states, the stator flux linkages due to stator currents are measured at different magnetization states. Fig. 5.6a presents a comparison of d-axis flux linkage at three different magnetization states for $i_q = 16\ A$. Similarly, Fig. 5.6b shows a comparison of q-axis flux linkage at three different magnetization states for $i_d = 16\ A$. The plots suggest that the qd flux linkages also vary with the magnetization state of the VFM. For higher magnetization state, the flux linkage due to the stator currents are lower. The plots also show that the change in the flux linkages produced by stator current has less variation between 80% and 56% magnetization states.

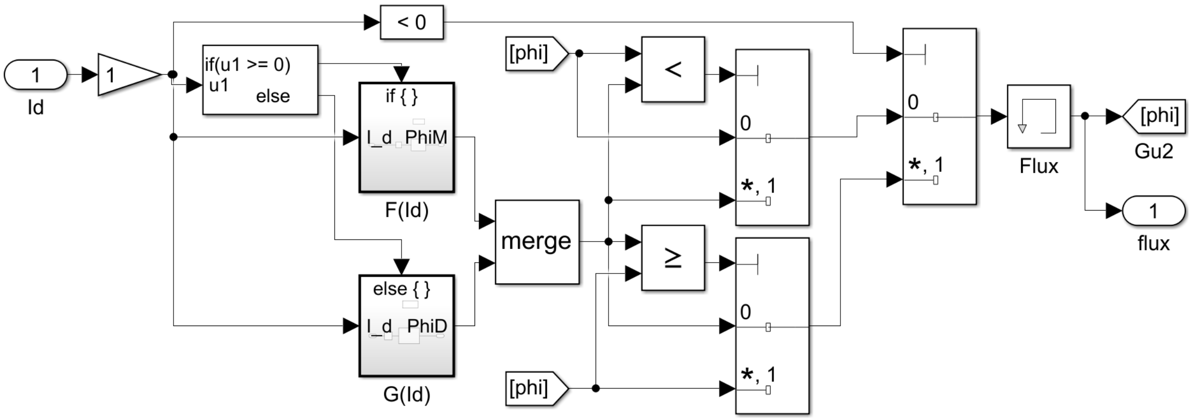

Fig. 5.7: MATLAB Simulink implementation of magnetization ($\mathcal{F}$) and demagnetization ($\mathcal{G}$) characteristics of the VFM.

5.4 Simulation and Validation of the Model

Based on the mathematical model of the VFM represented by (5.1)-(5.4), a MATLAB Simulink model of the hybrid VFM is developed using the experimentally measured magnetization, and flux linkage characteristics. These characteristics are utilized as look-up tables in the Simulink model. Fig. 5.7 shows the implementation of the magnet flux computation subsystem in MATLAB Simulink. It implements (5.4) utilizing experimentally obtained $\mathcal{F}$ and $\mathcal{G}$ with cubic spline interpolation. A memory block is used to initialize and hold the magnet flux linkage. The magnet flux depends on both the magnitude and direction of i_d and previous value of the magnet flux. If a positive i_d of certain amplitude is applied to the VFM and the magnet flux corresponding to i_d in the look-up table is smaller than the current magnet flux, i_d does not have any effect on the magnetization state of the VFM. Similarly, if a negative i_d of certain amplitude is applied to the VFM, and the magnet flux corresponding to the applied i_d in the look-up table is higher than the current magnet flux, there is no change in the magnetization state of the VFM.

In order to validate the developed model and measured flux linkages, an experimental setup was built to measure the transient and steady state response of the VFM for a step change in the q-axis current (hence torque). The test bench consists of the dynamometer system shown in Fig. 5.2. The dc dynamometer is operated in speed control mode using an ABB DCS800 drive. It is used to run and control the test motor speed at 600 rpm. The test motor is operated in current control mode using an OPAL-RT OP4510 system. Proportional-integral controllers without the feed forward terms that represent the speed voltage terms are used as current controllers, and they are designed to have a bandwidth of 400 Hz and a phase margin of 64°. The q-axis current reference is changed from 2 A to 7 A while the d-axis reference is kept zero. Both i_d and i_q are measured and recorded at steady state and transient conditions. After steady state at $i_q = 7\ A$, the i_q reference is changed

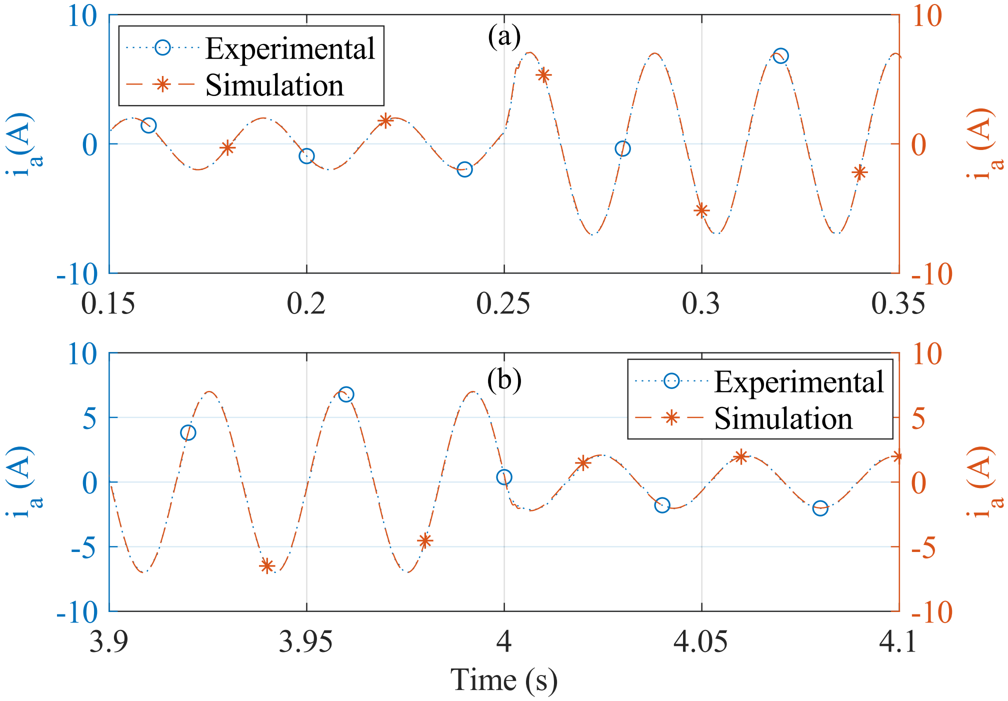

Fig. 5.8: Comparison of simulated and experimental current transients. (a). Phase A currents for a step change in i_q from 2 A to 7 A. (b). Phase A currents for a step change in i_q from 7 A to 2 A.

back to 2 A. Both the steady state and transient currents are measured and recorded.

A similar transient in i_q is applied to the VFM model in MATLAB Simulink. The same PI controllers with same values of gains are used in the simulation model. Figs. 5.8, 5.9 and 5.10 present the comparison of experimentally obtained steady state and transient responses with the simulated responses for similar conditions. Fig. 5.8a compares the experimental and simulated phase A currents when the i_q is increased from 2 A to 7 A. Since the rotor position during the experiment at which the reference current is changed is recorded, the current reference is changed at the same rotor position during simulation. It shows that the experimental and simulated currents are almost the same during steady state and transient periods. Fig. 5.8b presents the comparison of experimental and simulated phase A currents when the reference i_q is reduced back to 2 A. It also shows that the experimental and simulated current waveforms are almost the same.

In Fig. 5.9a, the axis levels are shifted for visually differentiating the two curves. It shows that the experimental i_q has a small ripple while the simulated current is ripple free. The two transients are almost the same validating the measured flux linkages. Fig. 5.9b shows that the d-axis current is disturbed when the q-axis current reference is changed. It is the result of the speed transient due to the sudden increase in the motor torque that caused a drift in the motor speed. Such a transient can be eliminated by adding feedforward terms in the controller that represent the speed voltage terms. However, the speed voltage terms are not applied in the controllers in this test on purpose so that

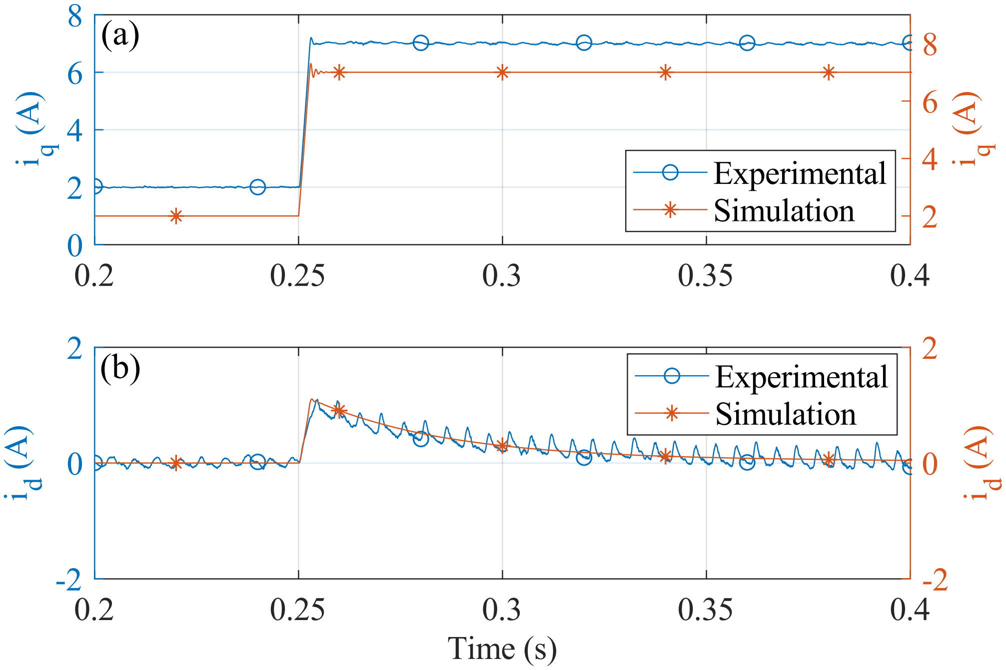

Fig. 5.9: Comparison of simulated and experimental current transients with a step change in i_q from 2 A to 7 A. (a) i_q transients. (b). i_d transients.

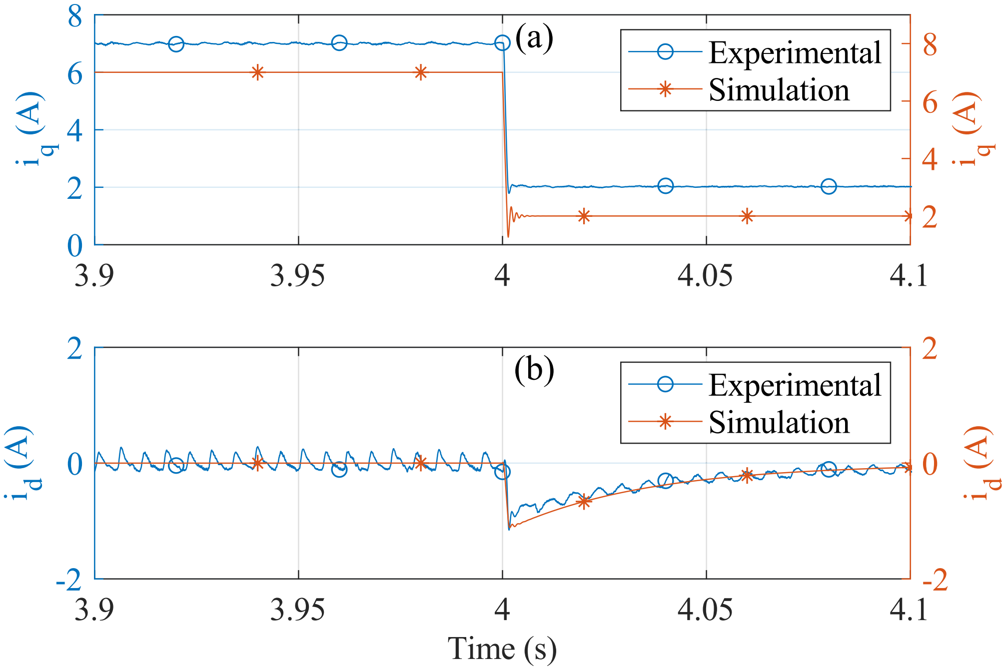

Fig. 5.10: Comparison of simulated and experimental current transients for a step change in i_q from 7 A to 2 A. (a) i_q transients. (b). i_d transients.

the experimental and simulated current transients can be compared. In Fig. 5.10, it is seen that the simulated currents have no ripple in steady state while the experimental currents possess ripples.

The plots also show that the simulated and transient responses are similar, validating the measured flux linkages.

5.5 Summary

This chapter presented the parameter measurements of a novel hybrid VFM with series rare-earth and AlNiCo magnets. It is proposed to use a current control based method to measure the VFM parameters. For VFMs with rotor d-axis not locking with the stator phase A with the conventional method, this chapter presented a solution that is more promising in VFMs where the magnet flux linkage has to be measured at different current magnitudes. Based on the measured magnetization and flux linkages characteristics, a simulation model of the VFM is developed for motor emulation applications requiring an accurate machine model. The experimentally obtained magnetization and flux linkage characteristics are used as look-up tables in the developed model. In order to validate the developed model and the measured flux linkages, current transients are applied to both the simulation model and the test motor under similar conditions. The comparison of the experimental and simulated current waveforms are almost the same. This validates the measured flux linkages and the developed model.

Based on the work presented in this chapter, the following research paper is published [58, 72, 121].

- R. Thike and P. Pillay, ”Parameter Measurements and Modeling of a Novel Hybrid Variable Flux Machine with Series Rare-Earth and AlNiCo Magnets,” 2020 IEEE Energy Conversion Congress and Exposition (ECCE), Detroit, MI, USA, 2020, pp. 1433-1438, doi: 10.1109/ECCE44975.2020.9235628
- K. S. Amitkumar, R. Thike and P. Pillay, ”Linear Amplifier-Based Power-Hardware-in-the-Loop Emulation of a Variable Flux Machine,” in IEEE Transactions on Industry Applications, vol. 55, no. 5, pp. 4624-4632, Sept.-Oct. 2019, doi: 10.1109/TIA.2019.2921286.
- K. S. Amitkumar, R. Thike and P. Pillay, ”Power-Hardware-in-the-Loop Based Emulation of a Variable Flux Machine,” 2018 IEEE Energy Conversion Congress and Exposition (ECCE), Portland, OR, 2018, pp. 6454-6460, doi: 10.1109/ECCE.2018.8558315.

Chapter 6

Conclusion and Future Works

This thesis presented an automated current control method to measure the parameters of special electric machines. The proposed parameter measurement method is validated with the test performed on a SynRM, and it is also applied to measure the parameters of a shifted IPMSM with aligned magnet and reluctance torques and a hybrid VFM using rare-earth and AlNiCo magnets in series, for modeling these machines. The main conclusions of this thesis and the future works corresponding to each chapters are presented below.

6.1 Automated Current Control Method for Flux-Linkage Measurement

Chapter 2 developed an automated current control method for flux linkage measurement of special electric machines with a SynRM as a test motor. The conclusions of this chapter are as follows.

- When a VSI is used, the voltage pulse method is limited to measure the parameter at certain operating points in the $i_d i_q$ plane.
- The number of samples available during the transient varies with the voltage pulse method, which results in reduced measurement accuracy for the machines with lower time constants.
- The proposed current control method can be used to measure the flux linkages at any operating point in the $i_d i_q$ plane, and the transient response can be modified such that an adequate number of samples are available during the transient, irrespective of the machine time constant.

- The proposed current controller design technique ensures similar machine responses for a wide range of machine inductance variations due to saturation and cross-magnetizing effects, making it suitable for parameter measurements using a real time system.
- The chapter also presented an online implementation of the proposed parameter measurement method. A comparison with the parameters measured using the standard AC locked rotor test and constant speed method test show that the proposed method produces highly accurate machine flux linkages and inductances.

The followings are few limitations and future works associated with the work presented in chapter 2.

- In the implementation of the proposed method to measure the flux linkages, analog voltage sensors are used to measure the voltage across the machine terminals. Since the voltages being measured are switching voltages, an analog filter is a must before sampling the measured signals. An investigation on avoiding the use of analog voltage sensors could be one of the possible future works.
- If 'N' is the number of evenly spaced divisions in current magnitudes, the number of experimental tests required to obtain the flux linkage characteristics is $2N^2$ in the proposed algorithm. It is possible to reduce the number of experimental tests to 2 N. Implementation and validation of such algorithm could be an extension to the work presented.
- The proposed technique is implemented to measure the flux linkages of a SynRM at locked rotor condition. Implementation of the proposed technique without requiring the rotor being locked would be one of the future works.

6.2 Torque Performance of a Segmented Pole SynRM with Grain-Oriented Laminations

Chapter 3 presented the study on the torque performance of a segmented pole SynRM with grain-oriented laminations. The conclusions of this chapter are as follows.

- LRT with averaging over the rotor periphery can be used to obtain an accurate estimate of MTPA trajectory of a SynRM. The same test can be used to obtain the torque-ripple of a SynRM over the entire operating range.

- The SynRM using segmented CRGO laminations has higher torque per ampere and thus higher saliency ratio. Due to higher saliency ratio, the CRGO SynRM has higher power factor than the CRNGO SynRM.
- The CRGO SynRM has lower torque ripple compared to the CRNGO SynRM.

The future works related to the research work presented in chapter 3 are as follows.

- The experimentally obtained torque-speed curves for the test SynRMs showed that the CRNGO SynRM having higher torque ripple had a lower torque-speed range compared to the CRGO SynRM when operated in speed controlled mode with the controller having the same bandwidth. A detailed investigation on this with a proper mathematical analysis can be one of the future works.
- One of the experimental methods to obtain the torque angle curve is to compute the torque using measured inductances. In order to obtain the MTPA trajectory from inductances, position dependent inductances are required to obtain a better estimate of torque angle curves. A study on the effective rotor position at which measured inductances would produce the actual MTPA trajectory could be one of the extensions to the work presented.

6.3 Modeling of a Shifted Interior Permanent Magnet Machine

Chapter 4 presented the mathematical model of a novel shifted IPMSM with aligned magnet and reluctance torques. In order to obtain the parameters in the developed model, the automated current control method to obtain the flux linkage developed in chapter 2 was used. The developed model is validated by comparing the experimental torque angle and torque-speed curves with the ones generated from the model. The conclusions on the research work presented in this chapter are as follows.

- Due to the difference in the magnet and reluctance axes positions, the existing mathematical model of a regular IPMSM is not applicable to the shifted IPMSM in its present form.
- Two different forms of the mathematical model of the shifted IPMSM are developed which depend on the choice of rotor d-axis location. One of the forms has the same expression for the magnet torque as the regular IPMSM while the other has the same expression for the reluctance torque as the regular IPMSM.

- Due to the shift in the relative position of the magnet and reluctance axes, the regular experimental method to locate the rotor d-axis in the regular IPMSM is not applicable to the shifted IPMSM. This chapter presented an experimental method to find the rotor d-axis position of a shifted IPMSM.
- The FFT analysis of the measured inductance waveform of the prototyped shifted IPMSM suggested that it has a first harmonic inductance component, which is responsible for asymmetrical torque angle curve in the negative torque region.
- In the shifted IPMSM, the motoring mode torque and power is higher than the braking torque and power at lower speeds. However, the torque and power at higher speeds are the same for both modes of operation.
- Chapter 4 also presented the characterization of machine back EMF, inductance and torque with a FEA software tool used to design and simulate the shifted IPMSM. Due to manufacturing tolerance and modeling inaccuracy, deviations exist between the measured and simulated performance quantities.

The research work presented in chapter 4 is one of the initial works in the area of shifted IPMSM modeling. The future works related to this research work are as follows.

- The developed model considers no spatial first harmonic inductance variation. While it is true for an ideal motor and it would be negligible in the improved designs, its inclusion in the mathematical model would be beneficial for higher performance drives. One of the future works would be the modification in the developed model to include the spatial first harmonic inductance.
- Two forms of mathematical model are developed in this research. As an extension to this work, a study on application of each form in the operation of drives would be required for the development of a drive using the shifted IPMSM.
- The magnet axis in the shifted IPMSM is not aligned along either the maximum or the minimum reluctance axes. While the position sensorless control of regular PMSMs and SynRMs utilizes the saliency property to detect the rotor position, this investigation in the shifted IPMSM is one of the interesting future works.

6.4 Parameter Measurements and Modeling of a Novel Hybrid Variable Flux Machine

Chapter 5 presented the mathematical model of a novel hybrid variable flux machine having series rare-earth and AlNiCo magnets. It utilizes the same current control method to measure the machine parameters. It also presented the validation of the developed model with experimental and simulation transients. The conclusions of this chapter are as follows.

- A mathematical model of a VFM is presented considering magnet flux as a function of d-axis current.
- It is proposed to use the same automated current control method in chapter 2 to measure the VFM flux linkages.
- It also presented an experimental method to locate the rotor d-axis for VFMs in which the conventional method is not applicable.
- A simulation model of the test VFM is built in MATLAB Simulink using the experimentally obtained magnetization and flux linkage curves, satisfying the developed equations.
- Comparison of simulation and experimental steady state and transient currents for a step change in q-axis current shows that the simulation model represents the actual motor characteristics.

Although this thesis presented some works related to the VFM modeling, more work is required in this area to represent the VFM for high performance applications. The following are few of them.

- Since the VFMs are frequently magnetized and demagnetized in variable speed applications, validation of the model during magnetization and demagnetization transients is necessary.
- This thesis validates the developed model by comparing simulation and experimental transients. A higher level validation using the model in an actual power hardware in the loop emulation is necessary for the actual implementation of the model in such applications.

Appendix A

MATLAB Programs

A.1 Development of Inductance Matrix in abc Frame

The following MATLAB code is used to generate the inductance matrix of the shifted IPMSM in abc reference frame when the rotor d-axis is along the magnet flux axis. It uses the symbolic operations to the symbolic variables.

```
clear
clc
% Define symbolic variables representing physical and geometric data
syms Mu_o Ns Beta_s Alfa_1 Alfa_2 Theta_r r l Zeta

% Define symbolic variables for stator current and inductances
syms Ias Ibs Ics Laa Lab Lac Lba Lbb Lbc Lca Lcb Lcc

% Define symbolic variabled for winding distribution functions
syms NasBeta_s NbsBeta_s NcsBeta_s
NasBeta_s=-Ns/2*sin(Beta_s);
NbsBeta_s=-Ns/2*sin(Beta_s-2*pi/3);
NcsBeta_s=-Ns/2*sin(Beta_s-4*pi/3);

```

```
    % Define flux distributions due to individual phase excitations
    syms Br_a_exc Brb_exc Brc_exc
    Br_a_exc=Mu_o*Ns/2*Ias*cos(Zeta)*(Alfa_1-Alfa_2*sin(2*Zeta-2*Theta_r));
    Br_b_exc=Mu_o*Ns/2*Ibs*cos(Zeta-2*pi/3)*(Alfa_1-Alfa_2*sin(2*Zeta-2*Theta_r));
    Br_c_exc=Mu_o*Ns/2*Ics*cos(Zeta-4*pi/3)*(Alfa_1-Alfa_2*sin(2*Zeta-2*Theta_r));

    %Laa- phase A flux linkage due to excitation in phase A
    Temp=int(Br_a_exc*r*l,Zeta,Beta_s,Beta_s+pi); % temporary variable
    Laa=int(NasBeta_s*Temp,Beta_s,pi,2*pi)/Ias

    %Lab- Phase A flux linkage due to excitation in phase B
    Temp=int(Br_b_exc*r*l,Zeta,Beta_s,Beta_s+pi); % temporary variable
    Lab=int(NasBeta_s*Temp,Beta_s,pi,2*pi)/Ibs

    %Lac- Phase A flux linkage due to excitation in phase c
    Temp=int(Br_c_exc*r*l,Zeta,Beta_s,Beta_s+pi); % temporary variable
    Lac=int(NasBeta_s*Temp,Beta_s,pi,2*pi)/Ics

    %Lba- phase B flux linkage due to excitation in phase A
    Temp=int(Br_a_exc*r*l,Zeta,Beta_s,Beta_s+pi); % temporary variable
    Lba=int(NbsBeta_s*Temp,Beta_s,pi+2*pi/3,2*pi+2*pi/3)/Ias

    %Lbb- phase B flux linkage due to excitation in phase B
    Temp=int(Br_b_exc*r*l,Zeta,Beta_s,Beta_s+pi); % temporary variable
    Lbb=int(NbsBeta_s*Temp,Beta_s,pi+2*pi/3,2*pi+2*pi/3)/Ibs

    %Lbc- phase B flux linkage due to excitation in phase C
```

```
        Temp=int(Br_c_exc*r*l,Zeta,Beta_s,Beta_s+pi); % temporary variable
        Lbc=int(NbsBeta_s*Temp,Beta_s,pi+2*pi/3,2*pi+2*pi/3)/Ics

        %Lca- phase C flux linkage due to excitation in phase A
        Temp=int(Br_a_exc*r*l,Zeta,Beta_s,Beta_s+pi); % temporary variable
        Lca=int(NcsBeta_s*Temp,Beta_s,pi+4*pi/3,2*pi+4*pi/3)/Ias

        %Lcb- phase C flux linkage due to excitation in phase B
        Temp=int(Br_b_exc*r*l,Zeta,Beta_s,Beta_s+pi); % temporary variable
        Lcb=int(NcsBeta_s*Temp,Beta_s,pi+4*pi/3,2*pi+4*pi/3)/Ibs

        %Lcc- phase C flux linkage due to excitation in phase C
        Temp=int(Br_c_exc*r*l,Zeta,Beta_s,Beta_s+pi); % temporary variable
        Lcc=int(NcsBeta_s*Temp,Beta_s,pi+4*pi/3,2*pi+4*pi/3)/Ics
```

The followings are the outputs of the script when run in MATLAB 2018a.

```
Laa =

(Mu_o*Ns^2*l*r*pi*(2*Alfa_1 + Alfa_2*sin(2*Theta_r)))/8


Lab =

-(Mu_o*Ns^2*l*r*pi*(Alfa_1 + Alfa_2*cos(2*Theta_r - pi/6)))/8


Lac =

-(Mu_o*Ns^2*l*r*pi*(Alfa_1 - Alfa_2*cos(2*Theta_r + pi/6)))/8


Lba =
```

```

-(Mu_o*Ns^2*l*r*pi*(Alfa_1 + Alfa_2*sin(2*Theta_r + pi/3)))/8


Lbb =

(Mu_o*Ns^2*l*r*pi*(2*Alfa_1 + Alfa_2*cos(2*Theta_r + pi/6)))/8


Lbc =

-(Mu_o*Ns^2*l*r*pi*(Alfa_1 - Alfa_2*sin(2*Theta_r)))/8


Lca =

-(Mu_o*Ns^2*l*r*pi*(Alfa_1 - Alfa_2*cos(2*Theta_r + pi/6)))/8


Lcb =

-(Mu_o*Ns^2*l*r*pi*(Alfa_1 - Alfa_2*sin(2*Theta_r)))/8


Lcc =

(Mu_o*Ns^2*l*r*pi*(2*Alfa_1 - Alfa_2*cos(2*Theta_r - pi/6)))/8

>>
```

A.2 Development of Inductance Matrix in qd Frame

After the development of the inductance matrix in *abc* reference frame, it is broken down into two parts: constant part, and the sinusoidally varying part. The following code in MATLAB is used to obtain the inductance matrix in dq reference frame.

```
clear
clc
% Define the symbolic variables
syms Ia Ib Ic Lls Lms Labc theta_r Lambda_m Iabc Lrlc Lambda_abc Lambda_qd Tabc L_delta
% constant part of abc inductance
Labc=[Lls+Lms -Lms/2 -Lms/2;
-Lms/2 Lls+Lms -Lms/2;
-Lms/2 -Lms/2 Lls+Lms]
% position dependent part of the inductance
Lrlc=L_delta*...
[sin(2*theta_r) sin(2*theta_r-2*pi/3) sin(2*theta_r+2*pi/3);
sin(2*theta_r-2*pi/3) sin(2*theta_r+2*pi/3) sin(2*theta_r);
sin(2*theta_r+2*pi/3) sin(2*theta_r) sin(2*theta_r-2*pi/3)]
Iabc=[Ia; Ib; Ic]
% magnet flux linkage
Lambda_abcM=Lambda_m*[sin(theta_r);
sin(theta_r-2*pi/3);
sin(theta_r-4*pi/3)]
% abc to qd transformation
Tabc=2/3*[cos(theta_r) cos(theta_r-2*pi/3) cos(theta_r-4*pi/3);
sin(theta_r) sin(theta_r-2*pi/3) sin(theta_r-4*pi/3)]
% inverse of Tabc, qd to abc transformation
TabcInv=[cos(theta_r) sin(theta_r) 1;
cos(theta_r-2*pi/3) sin(theta_r-2*pi/3) 1;
cos(theta_r-4*pi/3) sin(theta_r-4*pi/3) 1;]
% inductance in qd frame for constant abc inductance
L_qd1=simplify(Tabc*(Labc*TabcInv))
% inductance in qd frame for position dependent abc inductance
L_qd2=simplify(Tabc*(Lrlc*TabcInv))
L_qd=simplify(L_qd1+L_qd2) % inductance in qd frame
Lambda_qd3=simplify(Tabc*Lambda_abcM) % qd flux linkage due to magnet
```

The followings are the output of the script when run in MATLAB 2018a.

```
Labc =
```

```

[ Lls + Lms,      -Lms/2,      -Lms/2]
[      -Lms/2, Lls + Lms,      -Lms/2]
[      -Lms/2,      -Lms/2, Lls + Lms]


Lrlc =

[                 L_delta*sin(2*theta_r), L_delta*sin(2*theta_r - (2*pi)/3), L_delta*sin(2*theta_r + (2*pi)/3)]
[ L_delta*sin(2*theta_r - (2*pi)/3), L_delta*sin(2*theta_r + (2*pi)/3),                 L_delta*sin(2*theta_r)]
[ L_delta*sin(2*theta_r + (2*pi)/3),                 L_delta*sin(2*theta_r), L_delta*sin(2*theta_r - (2*pi)/3)]


Iabc =

Ia
Ib
Ic


Lambda_abcM =

Lambda_m*sin(theta_r)
Lambda_m*sin(theta_r - (2*pi)/3)
Lambda_m*sin(theta_r - (4*pi)/3)


Tabc =

[ (2*cos(theta_r))/3, (2*cos(theta_r - (2*pi)/3))/3, (2*cos(theta_r - (4*pi)/3))/3]
[ (2*sin(theta_r))/3, (2*sin(theta_r - (2*pi)/3))/3, (2*sin(theta_r - (4*pi)/3))/3]
```

```


TabcInv =

[            cos(theta_r),            sin(theta_r), 1]
[ cos(theta_r - (2*pi)/3), sin(theta_r - (2*pi)/3), 1]
[ cos(theta_r - (4*pi)/3), sin(theta_r - (4*pi)/3), 1]


L_qd1 =

[ Lls + (3*Lms)/2,               0, 0]
[               0, Lls + (3*Lms)/2, 0]


L_qd2 =

[              0, (3*L_delta)/2, 0]
[ (3*L_delta)/2,               0, 0]


L_qd =

[ Lls + (3*Lms)/2,   (3*L_delta)/2, 0]
[   (3*L_delta)/2, Lls + (3*Lms)/2, 0]


Lambda_qd3 =

0
Lambda_m
```

Bibliography

[1] W. Xu, J. Zhu, Y. Zhang, Y. Wang, and G. Sun, "Characterization of advanced drive system for hybrid electric vehicles," in *Electrical Machines and Systems (ICEMS), 2010 International Conference on*, Oct 2010, pp. 487–492.

[2] N. R. Canada, "Electric vehicle technology roadmap for canada," Government of Canada, Tech. Rep., 2009.

[3] I. Husain, *Electric and Hybrid Vehicles: Design Fundamentals*, 2nd ed. Boca Raton, FL 33487-2742: CRC Press, 2011.

[4] M. Zaccagnino, "Electric vehicle sales:facts & figures." 701 Pennsylvania Avenue, NW Washington, DC 20004-2696202-508-5000: Edison Electric Institute, Oct. 2019. [Online]. Available: www.eei.org/issuesandpolicy/electrictransportation/Documents/FINAL_EV_Sales_Update_Oct2019.pdf

[5] B. Bilgin, J. Liang, M. V. Terzic, J. Dong, R. Rodriguez, E. Trickett, and A. Emadi, "Modeling and analysis of electric motors: State-of-the-art review," *IEEE Transactions on Transportation Electrification*, vol. 5, no. 3, pp. 602–617, Sep. 2019.

[6] E. Agamloh, A. von Jouanne, and A. Yokochi, "An overview of electric machine trends in modern electric vehicles," *Machines*, vol. 8, no. 2, p. 20, Apr. 2020.

[7] Z. Q. Zhu and D. Howe, "Electrical machines and drives for electric, hybrid, and fuel cell vehicles," *Proceedings of the IEEE*, vol. 95, no. 4, pp. 746–765, April 2007.

[8] I. Boldea, L. N. Tutelea, L. Parsa, and D. Dorrell, "Automotive electric propulsion systems with reduced or no permanent magnets: An overview," *IEEE Transactions on Industrial Electronics*, vol. 61, no. 10, pp. 5696–5711, Oct 2014.

[9] J. D. Widmer, R. Martin, and M. Kimiabeigi, "Electric vehicle traction motors without rare earth magne," *Sustainable Materials and Technologies*, vol. 3, pp. 7–13, Apr. 2015.

[10] W. Zhao, F. Xing, X. Wang, T. A. Lipo, and B. i. Kwon, "Design and analysis of a novel pm-assisted synchronous reluctance machine with axially integrated magnets by the finite-element method," *IEEE Transactions on Magnetics*, vol. 53, no. 6, pp. 1–4, June 2017.

[11] K. S. Amitkumar, "Emulation of permanent magnet machines," phdthesis, Concordia University, Mar. 2020.

[12] A. Vagati, "The synchronous reluctance solution: a new alternative in ac drives," in *Proceedings of IECON'94 - 20th Annual Conference of IEEE Industrial Electronics*, vol. 1, Sep. 1994, pp. 1–13 vol.1.

[13] X. Ma, G. J. Li, Z. Q. Zhu, G. W. Jewell, and J. Green, "Investigation on synchronous reluctance machines with different rotor topologies and winding configurations," *IET Electric Power Applications*, vol. 12, no. 1, pp. 45–53, 2018.

[14] A. Vagati, M. Pastorelli, G. Francheschini, and S. C. Petrache, "Design of low-torque-ripple synchronous reluctance motors," *IEEE Transactions on Industry Applications*, vol. 34, no. 4, pp. 758–765, Jul 1998.

[15] T. Matsuo and T. A. Lipo, "Rotor design optimization of synchronous reluctance machine," *IEEE Transactions on Energy Conversion*, vol. 9, no. 2, pp. 359–365, Jun 1994.

[16] R. Thike and P. Pillay, "Automatic inductance measurements of synchronous reluctance machines including cross-saturation using real-time systems," in *2018 IEEE Energy Conversion Congress and Exposition (ECCE)*, Sep. 2018, pp. 6121–6127.

[17] M. J. Kamper and A. F. Volsdhenk, "Effect of rotor dimensions and cross magnetisation on ld and lq inductances of reluctance synchronous machine with cageless flux barrier rotor," *IEE Proceedings - Electric Power Applications*, vol. 141, no. 4, pp. 213–220, Jul 1994.

[18] A. Vagati, "Synchronous reluctance electric motor having a low torque-ripple design," U.S. Patent US005 818 140A, Oct 6, 1998.

[19] S. Yamamoto, H. Hirahara, J. B. Adawey, T. Ara, and K. Matsuse, "Maximum efficiency drives of synchronous reluctance motors by a novel loss minimization controller with inductance estimator," *IEEE Transactions on Industry Applications*, vol. 49, no. 6, pp. 2543–2551, Nov 2013.

[20] M. Ferrari, N. Bianchi, and E. Fornasiero, "Analysis of rotor saturation in synchronous reluctance and pm-assisted reluctance motors," *IEEE Transactions on Industry Applications*, vol. 51, no. 1, pp. 169–177, Jan 2015.

[21] T. Lubin, H. Razik, and A. Rezzoug, “Magnetic saturation effects on the control of a synchronous reluctance machine,” *IEEE Transactions on Energy Conversion*, vol. 17, no. 3, pp. 356–362, Sep. 2002.

[22] A. Vagati, M. Pastorelli, F. Scapino, and G. Franceschini, “Impact of cross saturation in synchronous reluctance motors of the transverse-laminated type,” *IEEE Transactions on Industry Applications*, vol. 36, no. 4, pp. 1039–1046, Jul 2000.

[23] S. Taghavi and P. Pillay, “A novel grain-oriented lamination rotor core assembly for a synchronous reluctance traction motor with a reduced torque ripple algorithm,” *IEEE Transactions on Industry Applications*, vol. 52, no. 5, pp. 3729–3738, Sep. 2016.

[24] C. Desai, H. R. Mehta, and P. Pillay, “Fabrication and assembly method for synchronous reluctance machines,” *IEEE Transactions on Industry Applications*, vol. 54, no. 5, pp. 4227–4235, Sep. 2018.

[25] S. Sara Maroufian and P. Pillay, “Analytical modeling of a segmented-pole synchronous reluctance machine with crgo laminations,” in *2018 IEEE Energy Conversion Congress and Exposition (ECCE)*, Sep. 2018, pp. 7315–7321.

[26] N. Yang, W. Cao, Z. Liu, and J. Morrow, “Design of an asymmetrical rotor for easy assembly and repair of field windings in synchronous machines,” *The Journal of Engineering*, vol. 2017, no. 8, pp. 427–434, 2017.

[27] Y. Liu, L. Li, Q. Gao, J. Cao, R. Wang, and Z. Sun, “Analytical model of torque-prediction for a novel hybrid rotor permanent magnet machines,” *IEEE Access*, vol. 7, pp. 109 528–109 538, 2019.

[28] W. Zhao, H. Shen, T. A. Lipo, and X. Wang, “A new hybrid permanent magnet synchronous reluctance machine with axially sandwiched magnets for performance improvement,” *IEEE Transactions on Energy Conversion*, vol. 33, no. 4, pp. 2018–2029, Dec 2018.

[29] X. Zeng, L. Quan, X. Zhu, L. Xu, and F. Liu, “Investigation of an asymmetrical rotor hybrid permanent magnet motor for approaching maximum output torque,” *IEEE Transactions on Applied Superconductivity*, vol. 29, no. 2, pp. 1–4, March 2019.

[30] G. Xu, G. Liu, W. Zhao, Q. Chen, and X. Du, “Principle of torque-angle approaching in a hybrid rotor permanent-magnet motor,” *IEEE Transactions on Industrial Electronics*, vol. 66, no. 4, pp. 2580–2591, April 2019.

[31] G. Liu, G. Xu, W. Zhao, X. Du, and Q. Chen, "Improvement of torque capability of permanent-magnet motor by using hybrid rotor configuration," *IEEE Transactions on Energy Conversion*, vol. 32, no. 3, pp. 953–962, Sep. 2017.

[32] W. Zhao, F. Zhao, T. A. Lipo, and B. Kwon, "Optimal design of a novel v-type interior permanent magnet motor with assisted barriers for the improvement of torque characteristics," *IEEE Transactions on Magnetics*, vol. 50, no. 11, pp. 1–4, Nov 2014.

[33] W. Ren, Q. Xu, and Q. Li, "Asymmetrical v-shape rotor configuration of an interior permanent magnet machine for improving torque characteristics," *IEEE Transactions on Magnetics*, vol. 51, no. 11, pp. 1–4, Nov 2015.

[34] W. Zhao, T. A. Lipo, and B. Kwon, "Optimal design of a novel asymmetrical rotor structure to obtain torque and efficiency improvement in surface inset pm motors," *IEEE Transactions on Magnetics*, vol. 51, no. 3, pp. 1–4, March 2015.

[35] X. Du, G. Liu, Q. Chen, G. Xu, M. Xu, and X. Fan, "Optimal design of an inset pm motor with assisted barriers and magnet shifting for improvement of torque characteristics," *IEEE Transactions on Magnetics*, vol. 53, no. 11, pp. 1–4, Nov 2017.

[36] M. Ibrahim and P. Pillay, "Aligning the reluctance and magnet torque in permanent magnet synchronous motors for improved performance," in *2018 IEEE Energy Conversion Congress and Exposition (ECCE)*, Sep. 2018, pp. 2286–2291.

[37] S. Hayslett and E. Strangas, "Design and analysis of aligned axis interior permanent magnet machines considering saturation," in *2019 IEEE International Electric Machines Drives Conference (IEMDC)*, May 2019, pp. 686–692.

[38] H. Mirahki, M. Moallem, M. Ebrahimi, and B. Fahimi, "Asymmetrical magnet shape optimization based on s-c mapping for torque profile mitigation in unidirectional application of spms machine," *IEEE Transactions on Transportation Electrification*, vol. 5, no. 3, pp. 630–637, Sep. 2019.

[39] W. Zhao, D. Chen, T. A. Lipo, and B. Kwon, "Performance improvement of ferrite-assisted synchronous reluctance machines using asymmetrical rotor configurations," *IEEE Transactions on Magnetics*, vol. 51, no. 11, pp. 1–4, Nov 2015.

[40] P. Winzer and M. Doppelbauer, "Theoretical analysis of synchronous machines with displaced reluctance axis," in *2014 International Conference on Electrical Machines (ICEM)*, Sep. 2014, pp. 641–647.

[41] J. Y. Alsawalhi and S. D. Sudhoff, “Effects of positioning of permanent magnet axis relative to reluctance axis in permanent magnet synchronous machines,” in *2015 IEEE Power and Energy Conference at Illinois (PECI)*, Feb 2015, pp. 1–8.

[42] V. Ostovic, “Memory motors,” *IEEE Industry Applications Magazine*, vol. 9, no. 1, pp. 52–61, Jan 2003.

[43] V. Ostovic, “Memory motors-a new class of controllable flux pm machines for a true wide speed operation,” in *Conference Record of the 2001 IEEE Industry Applications Conference. 36th IAS Annual Meeting (Cat. No.01CH37248)*, vol. 4, Sep. 2001, pp. 2577–2584 vol.4.

[44] M. Ibrahim, “Application of magnetic hysteresis modeling to the design and analysis of electric machines,” Ph.D. dissertation, Concordia University, Montreal, Quebec, Canada, November 2014.

[45] M. Ibrahim, L. Masisi, and P. Pillay, “Design of variable-flux permanent-magnet machines using alnico magnets,” *IEEE Transactions on Industry Applications*, vol. 51, no. 6, pp. 4482–4491, Nov 2015.

[46] ——, “Design of variable flux permanent-magnet machine for reduced inverter rating,” *IEEE Transactions on Industry Applications*, vol. 51, no. 5, pp. 3666–3674, Sept 2015.

[47] M. Ibrahim and P. Pillay, “Design of high torque density variable flux permanent magnet machine using alnico magnets,” in *Energy Conversion Congress and Exposition (ECCE), 2014 IEEE*, Sept 2014, pp. 3535–3540.

[48] A. Takbash and P. Pillay, “Magnet design consideration of a variable-flux pm machine,” in *2017 IEEE Energy Conversion Congress and Exposition (ECCE)*, Oct 2017, pp. 3935–3941.

[49] C. Yiguang, P. Wei, W. Ying, T. Renyuan, and W. Jing, “Interior composite-rotor controllable-flux pmsm - memory motor,” in *2005 International Conference on Electrical Machines and Systems*, vol. 1, Sept 2005, pp. 446–449 Vol. 1.

[50] K. Sakai, K. Yuki, Y. Hashiba, N. Takahashi, and K. Yasui, “Principle of the variable-magnetic-force memory motor,” in *Electrical Machines and Systems, 2009. ICEMS 2009. International Conference on*, Nov 2009, pp. 1–6.

[51] Z. Changqing, W. Xiuhe, and W. Bei, “Study of a novel permanent magnet synchronous motor with composite-rotor,” in *2010 International Conference on Electrical Machines and Systems*, Oct 2010, pp. 1044–1047.

[52] G. Zhou, T. Miyazaki, S. Kawamata, D. Kaneko, and N. Hino, “Development of variable magnetic flux motor suitable for electric vehicle,” in *The 2010 International Power Electronics Conference - ECCE ASIA -*, June 2010, pp. 2171–2174.

[53] M. Aydin, Surong Huang, and T. A. Lipo, “A new axial flux surface mounted permanent magnet machine capable of field control,” in *Conference Record of the 2002 IEEE Industry Applications Conference. 37th IAS Annual Meeting (Cat. No.02CH37344)*, vol. 2, Oct 2002, pp. 1250–1257 vol.2.

[54] J. A. Tapia, F. Leonardi, and T. A. Lipo, “Consequent pole permanent magnet machine with field weakening capability,” in *Electric Machines and Drives Conference, 2001. IEMDC 2001. IEEE International*, 2001, pp. 126–131.

[55] N. Naoe and T. Fukami, “Trial production of a hybrid excitation type synchronous machine,” in *Electric Machines and Drives Conference, 2001. IEMDC 2001. IEEE International*, 2001, pp. 545–547.

[56] D. Fodorean, A. Djerdir, I. A. Viorel, and A. Miraoui, “A double excited synchronous machine for direct drive application 2014;design and prototype tests,” *IEEE Transactions on Energy Conversion*, vol. 22, no. 3, pp. 656–665, Sept 2007.

[57] M. Ibrahim and P. Pillay, “Design of hybrid variable flux motors for enhanced wide-speed performance,” in *2019 IEEE Energy Conversion Congress and Exposition (ECCE)*, Sep. 2019, pp. 6046–6053.

[58] K. S. Amitkumar, R. Thike, and P. Pillay, “Linear amplifier-based power-hardware-in-the-loop emulation of a variable flux machine,” *IEEE Transactions on Industry Applications*, vol. 55, no. 5, pp. 4624–4632, Sep. 2019.

[59] M. N. Ibrahim, P. Sergeant, and E. M. Rashad, “Relevance of including saturation and position dependence in the inductances for accurate dynamic modeling and control of synrms,” *IEEE Transactions on Industry Applications*, vol. 53, no. 1, pp. 151–160, Jan 2017.

[60] R. Thike and P. Pillay, “Vector controlled drive to measure inductances of variable flux machine,” in *2016 IEEE International Conference on Power Electronics, Drives and Energy Systems (PEDES)*, Dec 2016, pp. 1–6.

[61] S. Yamamoto, T. Kano, Y. Yamaguchi, and T. Ara, “A method to determine direct- and quadrature-axis inductances of permanent magnet synchronous motors,” *Electrical Engineering in Japan*, vol. 171, no. 3, pp. 41–50, 2010. [Online]. Available: https://onlinelibrary.wiley.com/doi/abs/10.1002/eej.20969

[62] A. Kilthau and J. M. Pacas, “Parameter-measurement and control of the synchronous reluctance machine including cross saturation,” in *Conference Record of the 2001 IEEE Industry Applications Conference. 36th IAS Annual Meeting (Cat. No.01CH37248)*, vol. 4, Sept 2001, pp. 2302–2309 vol.4.

[63] S. Yamamoto, T. Ara, and K. Matsuse, “A method to calculate transient characteristics of synchronous reluctance motors considering iron loss and cross-magnetic saturation,” *IEEE Transactions on Industry Applications*, vol. 43, no. 1, pp. 47–56, Jan 2007.

[64] B. Stumberger, G. Stumberger, D. Dolinar, A. Hamler, and M. Trlep, “Evaluation of saturation and cross-magnetization effects in interior permanent-magnet synchronous motor,” *IEEE Transactions on Industry Applications*, vol. 39, no. 5, pp. 1264–1271, Sept 2003.

[65] R. Thike and P. Pillay, “Characterization of a variable flux machine for transportation using a vector-controlled drive,” *IEEE Transactions on Transportation Electrification*, vol. 4, no. 2, pp. 494–505, June 2018.

[66] S. Wiedemann, S. Hall, R. M. Kennel, and M. Alaküla, “Dynamic testing characterization of a synchronous reluctance machine,” *IEEE Transactions on Industry Applications*, vol. 54, no. 2, pp. 1370–1378, March 2018.

[67] R. Nuscheler, “Determination of the inductances and the rotor flux-linkage of a permanent-field synchronous machine with reluctance effects,” in *The 4th International Power Electronics and Motion Control Conference, 2004. IPEMC 2004.*, vol. 2, Aug 2004, pp. 620–625 Vol.2.

[68] R. Thike and P. Pillay, “Experimental investigation of mtpa trajectory of synchronous reluctance machine,” in *2018 IEEE International Conference on Power Electronics, Drives and Energy Systems (PEDES)*, Dec 2018, pp. 1–6.

[69] C. M. Hackl, M. J. Kamper, J. Kullick, and J. Mitchell, “Current control of reluctance synchronous machines with online adjustment of the controller parameters,” in *2016 IEEE 25th International Symposium on Industrial Electronics (ISIE)*, June 2016, pp. 153–160.

[70] Ž. Plantić and G. Štumberger, “Determining parameters of a three phase permanent magnet synchronous machine using controlled single phase voltage source,” *PRZEGLAD ELEKTROTECHNICZNY (Electrical Review)*, vol. 87, pp. 0033–2097, 2011.

[71] J. B. Im, W. Kim, K. Kim, C. S. Jin, J. H. Choi, and J. Lee, “Inductance calculation method of synchronous reluctance motor including iron loss and cross magnetic saturation,” *IEEE Transactions on Magnetics*, vol. 45, no. 6, pp. 2803–2806, June 2009.

[72] K. S. Amitkumar, R. Thike, and P. Pillay, "Power-hardware-in-the-loop based emulation of a variable flux machine," in *2018 IEEE Energy Conversion Congress and Exposition (ECCE)*, Sep. 2018, pp. 6454–6460.

[73] N. Bedetti, S. Calligaro, and R. Petrella, "Stand-still self-identification of flux characteristics for synchronous reluctance machines using novel saturation approximating function and multiple linear regression," *IEEE Transactions on Industry Applications*, vol. 52, no. 4, pp. 3083–3092, July 2016.

[74] M. Hinkkanen, P. Pescetto, E. Mölsä, S. E. Saarakkala, G. Pellegrino, and R. Bojoi, "Sensorless self-commissioning of synchronous reluctance motors at standstill without rotor locking," *IEEE Transactions on Industry Applications*, vol. 53, no. 3, pp. 2120–2129, May 2017.

[75] S.-H. Hwang, J.-M. Kim, H. V. Khang, and J.-W. Ahn, "Parameter identification of a synchronous reluctance motor by using a synchronous pi current regulator at a standstill," *Journal of Power Electronics*, vol. 10, 09 2010.

[76] N. R. Tavana and V. Dinavahi, "A general framework for fpga-based real-time emulation of electrical machines for hil applications," *IEEE Transactions on Industrial Electronics*, vol. 62, no. 4, pp. 2041–2053, April 2015.

[77] C. Dufour, S. Cense, T. Yamada, R. Imamura, and J. Bélanger, "Fpga permanent magnet synchronous motor floating-point models with variable-dq and spatial harmonic finite-element analysis solvers," in *2012 15th International Power Electronics and Motion Control Conference (EPE/PEMC)*, Sept 2012, pp. LS6b.2–1–LS6b.2–10.

[78] K. S. Amitkumar, R. S. Kaarthik, and P. Pillay, "A versatile power-hardware-in-the-loop-based emulator for rapid testing of transportation electric drives," *IEEE Transactions on Transportation Electrification*, vol. 4, no. 4, pp. 901–911, Dec 2018.

[79] "Ieee draft trial-use guide for testing permanent magnet machines," *IEEE P1812/D2, January 2013*, pp. 1–81, Feb 2013.

[80] R. Thike and P. Pillay, "Automated current control method for flux-linkage measurement of synchronous reluctance machines," *IEEE Transactions on Industry Applications*, vol. 56, no. 2, pp. 1464–1474, March 2020.

[81] M. A. J. Kondelaji and M. Mirsalim, "Segmented-rotor modular switched reluctance motor with high torque and low torque ripple," *IEEE Transactions on Transportation Electrification*, vol. 6, no. 1, pp. 62–72, March 2020.

[82] S. S. Maroufian and P. Pillay, “Torque characterization of a synchronous reluctance machine using an analytical model,” *IEEE Transactions on Transportation Electrification*, pp. 1–1, 2018.

[83] K. C. Kim and D. S. Ryu, “Torque characteristic with respect to the load angle of a permanent magnet motor,” *IEEE Transactions on Magnetics*, vol. 48, no. 11, pp. 4200–4203, Nov 2012.

[84] C.-T. Pan and S. M. Sue, “A linear maximum torque per ampere control for ipmsm drives over full-speed range,” *IEEE Transactions on Energy Conversion*, vol. 20, no. 2, pp. 359–366, June 2005.

[85] P. Niazi, H. A. Toliyat, and A. Goodarzi, “Robust maximum torque per amp (mtpa) control of pm-assisted synrm for tractions applications,” in *2005 IEEE Vehicle Power and Propulsion Conference*, Sept 2005, pp. 624–630.

[86] J. Chen, J. Li, and R. Qu, “Maximum-torque-per-ampere and magnetization-state control of a variable-flux permanent magnet machine,” *IEEE Transactions on Industrial Electronics*, vol. 65, no. 2, pp. 1158–1169, Feb 2018.

[87] H. W. de Kock, A. J. Rix, and M. J. Kamper, “Optimal torque control of synchronous machines based on finite-element analysis,” *IEEE Transactions on Industrial Electronics*, vol. 57, no. 1, pp. 413–419, Jan 2010.

[88] A. P. Goncalves, S. M. A. Cruz, F. J. T. E. Ferreira, A. M. S. Mendes, and A. T. D. Almeida, “Synchronous reluctance motor drive for electric vehicles including cross-magnetic saturation,” in *2014 IEEE Vehicle Power and Propulsion Conference (VPPC)*, Oct 2014, pp. 1–6.

[89] C. Desai and P. Pillay, “Torque-angle characterization of a synchronous reluctance machine,” in *2016 IEEE International Conference on Power Electronics, Drives and Energy Systems (PEDES)*, Dec 2016, pp. 1–5.

[90] J. A. Güemes, A. M. Iraolagoitia, J. I. D. Hoyo, and P. Fernández, “Torque analysis in permanent-magnet synchronous motors: A comparative study,” *IEEE Transactions on Energy Conversion*, vol. 26, no. 1, pp. 55–63, March 2011.

[91] S.-M. Hwang, J.-B. Eom, Y.-H. Jung, D.-W. Lee, and B.-S. Kang, “Various design techniques to reduce cogging torque by controlling energy variation in permanent magnet motors,” *IEEE Transactions on Magnetics*, vol. 37, no. 4, pp. 2806–2809, Jul 2001.

[92] T. M. Jahns and W. L. Soong, “Pulsating torque minimization techniques for permanent magnet ac motor drives-a review,” *IEEE Transactions on Industrial Electronics*, vol. 43, no. 2, pp. 321–330, April 1996.

[93] N. Bianchi, M. Degano, and E. Fornasiero, "Sensitivity analysis of torque ripple reduction of synchronous reluctance and interior pm motors," *IEEE Transactions on Industry Applications*, vol. 51, no. 1, pp. 187–195, Jan 2015.

[94] M. Muteba, B. Twala, and D. V. Nicolae, "Torque ripple minimization in synchronous reluctance motor using a sinusoidal rotor lamination shape," in *2016 XXII International Conference on Electrical Machines (ICEM)*, Sept 2016, pp. 606–611.

[95] M. Sanada, K. Hiramoto, S. Morimoto, and Y. Takeda, "Torque ripple improvement for synchronous reluctance motor using an asymmetric flux barrier arrangement," *IEEE Transactions on Industry Applications*, vol. 40, no. 4, pp. 1076–1082, July 2004.

[96] N. Bianchi, E. Fornasiero, M. Ferrari, and M. Castiello, "Experimental comparison of pm-assisted synchronous reluctance motors," *IEEE Transactions on Industry Applications*, vol. 52, no. 1, pp. 163–171, Jan 2016.

[97] M. A. Kabir and I. Husain, "Application of a multilayer ac winding to design synchronous reluctance motors," *IEEE Transactions on Industry Applications*, vol. 54, no. 6, pp. 5941–5953, Nov 2018.

[98] C. Babetto, G. Bacco, and N. Bianchi, "Synchronous reluctance machine optimization for high-speed applications," *IEEE Transactions on Energy Conversion*, vol. 33, no. 3, pp. 1266–1273, Sept 2018.

[99] S. S. R. Bonthu, M. T. B. Tarek, and S. Choi, "Optimal torque ripple reduction technique for outer rotor permanent magnet synchronous reluctance motors," *IEEE Transactions on Energy Conversion*, vol. 33, no. 3, pp. 1184–1192, Sept 2018.

[100] Z. Q. Zhu, "A simple method for measuring cogging torque in permanent magnet machines," in *2009 IEEE Power Energy Society General Meeting*, July 2009, pp. 1–4.

[101] G. Heins, M. Thiele, and T. Brown, "Accurate torque ripple measurement for pmsm," *IEEE Transactions on Instrumentation and Measurement*, vol. 60, no. 12, pp. 3868–3874, Dec 2011.

[102] L. Ferraris, F. Franchini, and E. Poskovic, "The cogging torque measurement through a new validated methodology," in *2017 11th IEEE International Conference on Compatibility, Power Electronics and Power Engineering (CPE-POWERENG)*, April 2017, pp. 398–403.

[103] S. Taghavi, "Design of synchronous reluctance machines for automotive applications," Ph.D. dissertation, Concordia University, Canada, 2015.

[104] R. Thike and P. Pillay, "Experimental study of torque-ripple and its effect on the flux weakening range of synchronous reluctance machines," in *2019 IEEE International Electric Machines Drives Conference (IEMDC)*, May 2019, pp. 1479–1484.

[105] A. Vagati, B. Boazzo, P. Guglielmi, and G. Pellegrino, "Design of ferrite-assisted synchronous reluctance machines robust toward demagnetization," *IEEE Transactions on Industry Applications*, vol. 50, no. 3, pp. 1768–1779, May 2014.

[106] M. Barcaro and N. Bianchi, "Interior pm machines using ferrite to substitute rare-earth surface pm machines," in *2012 XXth International Conference on Electrical Machines*, Sep. 2012, pp. 1339–1345.

[107] H. Kim, K. Kim, Y. Jo, and J. Hur, "Optimization methods of torque density for developing the neodymium free spoke-type bldc motor," *IEEE Transactions on Magnetics*, vol. 49, no. 5, pp. 2173–2176, May 2013.

[108] N. Limsuwan, T. Kato, K. Akatsu, and R. D. Lorenz, "Design and evaluation of a variable-flux flux-intensifying interior permanent-magnet machine," *IEEE Transactions on Industry Applications*, vol. 50, no. 2, pp. 1015–1024, March 2014.

[109] G. Qiao, M. Wang, F. Liu, Y. Liu, P. Zheng, and Y. Sui, "Analysis of magnetic properties of alnico and magnetization state estimation in variable-flux pmsms," *IEEE Transactions on Magnetics*, vol. 55, no. 7, pp. 1–6, July 2019.

[110] A. Fatemi, N. A. O. Demerdash, T. W. Nehl, and D. M. Ionel, "Large-scale design optimization of pm machines over a target operating cycle," *IEEE Transactions on Industry Applications*, vol. 52, no. 5, pp. 3772–3782, Sep. 2016.

[111] G. Xu, G. Liu, S. Jiang, and Q. Chen, "Analysis of a hybrid rotor permanent magnet motor based on equivalent magnetic network," *IEEE Transactions on Magnetics*, vol. 54, no. 4, pp. 1–9, April 2018.

[112] P. C. Krause, O. Wasynczuk, and S. D. Sudhoff, *Basic Principles for Electric Machine Analysis*. IEEE, 2002. [Online]. Available: https://ieeexplore.ieee.org/document/5265720

[113] K. H. Nam, *AC Motor Cotrol and Electric Vehicle Applications*. CRC Press, 2010.

[114] B. Lee, S. Kwon, T. Sun, J. Hong, G. Lee, and J. Hur, "Modeling of core loss resistance for $d - q$ equivalent circuit analysis of ipmsm considering harmonic linkage flux," *IEEE Transactions on Magnetics*, vol. 47, no. 5, pp. 1066–1069, May 2011.

[115] R. Thike and P. Pillay, “Mathematical model of an interior pmsm with aligned magnet and reluctance torques,” *IEEE Transactions on Transportation Electrification*, vol. 6, no. 2, pp. 647–658, 2020.

[116] T. Kato, N. Limsuwan, C. Y. Yu, K. Akatsu, and R. D. Lorenz, “Rare earth reduction using a novel variable magnetomotive force flux-intensified ipm machine,” *IEEE Transactions on Industry Applications*, vol. 50, no. 3, pp. 1748–1756, May 2014.

[117] H. Hua, Z. Q. Zhu, A. Pride, R. Deodhar, and T. Sasaki, “Comparative study on variable flux memory machines with parallel or series hybrid magnets,” *IEEE Transactions on Industry Applications*, vol. 55, no. 2, pp. 1408–1419, March 2019.

[118] Y. Lee, Y. Kwon, and S. Sul, “Dc-link voltage design of high-bandwidth motor emulator for interior permanent-magnet synchronous motors,” in *2018 IEEE Energy Conversion Congress and Exposition (ECCE)*, 2018, pp. 4453–4459.

[119] N. BEDETTI, S. CALLIGARO, and R. PETRELLA, “Feasible auto-tuning procedure for mid-performance sensorless ipmsm and synrm drives,” in *2019 IEEE 10th International Symposium on Sensorless Control for Electrical Drives (SLED)*, 2019, pp. 1–6.

[120] J. Jacob, P. Kumar, S. Calligaro, and R. Petrella, “Self-commissioning identification of permanent magnet flux-linkage magnitude in sensorless drives for pmsm at quasi stand-still,” in *2018 IEEE 9th International Symposium on Sensorless Control for Electrical Drives (SLED)*, 2018, pp. 144–149.

[121] R. Thike and P. Pillay, “Parameter measurements and modeling of a novel hybrid variable flux machine with series rare-earth and alnico magnets,” in *2020 IEEE Energy Conversion Congress and Exposition (ECCE)*, 2020, pp. 1433–1438.